MOUNTAIN-PLAINS CONSORTIUM

MPC 22-474 | C. Pantelides and I. Dangol

HYBRID BRIDGE BENTS USING POST-TENSIONED PRECAST COLUMNS FOR ACCELERATED BRIDGE CONSTRUCTION IN HIGH SEISMIC REGIONS

MOUNTAIN-PLAINS CONSORTIUM REGION 8

A University Transportation Center sponsored by the U.S. Department of Transportation serving the Mountain-Plains Region. Consortium members:

Colorado State University
North Dakota State University
South Dakota State University
University of Colorado Denver
University of Denver
University of Utah
Utah State University
University of Wyoming

Technical Report Documentation Page

1. Report No.	2. Government Accession No.	3. Recipient's Catalog No.
MPC-588		

4. Title and Subtitle	5. Report Date
Hybrid Bridge Bents Using Post-tensioned Precast Columns for Accelerated Bridge Construction in High Seismic Regions	September 2022
	6. Performing Organization Code

7. Author(s)	8. Performing Organization Report No.
C. Pantelides I. Dongol	MPC 22-474

9. Performing Organization Name and Address	10. Work Unit No. (TRAIS)
University of Utah 2115 Meldrum Building Salt Lake City, UT 84112	11. Contract or Grant No.

12. Sponsoring Agency Name and Address	13. Type of Report and Period Covered
Mountain-Plains Consortium North Dakota State University PO Box 6050, Fargo, ND 58108	Final Report
	14. Sponsoring Agency Code

15. Supplementary Notes

Supported by a grant from the US DOT, University Transportation Centers Program

16. Abstract

A new method for building seismically resilient bridges is proposed using Accelerated Bridge Construction (ABC) methods. The hybrid two-column bridge bent consists of post-tensioned precast concrete columns with a buckling restrained brace (BRB) as an external energy dissipation device. The design of initial post-tensioning forces and the selection of the appropriate strength of the BRB is provided. The BRB used had two steel cores; the first BRB steel core fractured during the 5.0% drift ratio and the second steel core fractured during the 6.0% drift ratio. The two unbonded post-tensioned (PT) bars of the west column yielded after fracture of the BRB steel cores, while the two PT bars of the east column did not yield. The precast concrete elements of the hybrid bridge bent remained undamaged up to 6.0% drift ratio. The longitudinal mild steel bars of the columns did not yield until the 6.0% drift ratio. The gusset assemblies at the cap beam and the footing remained elastic. The damaged BRB could be easily replaced after an earthquake and the steel gussets could be used to re-center the bridge bent; thus, the proposed system is promising for constructing resilient bridges using ABC methods in high seismic regions that should remain functional after an earthquake. An analytical model of a double rocking bridge bent consisting of two octagonal columns with two post-tensioned bars each and detached joints was developed using OpenSees.

17. Key Word	18. Distribution Statement
bents, bridge construction, buckling, columns, earthquake resistant design, precast concrete, repeated loads	Public distribution

19. Security Classif. (of this report)	20. Security Classif. (of this page)	21. No. of Pages	22. Price
Unclassified	Unclassified	102	n/a

Form DOT F 1700.7 (8-72) Reproduction of completed page authorized

HYBRID BRIDGE BENTS USING POST-TENSIONED PRECAST COLUMNS FOR ACCELERATED BRIDGE CONSTRUCTION IN HIGH SEISMIC REGIONS

Chris P. Pantelides
Professor

Ijan Dangol
Graduate Student

Department of Civil and Environmental Engineering
The University of Utah

September 2022

Acknowledgments

The authors acknowledge the financial support provided by the Mountain-Plains Consortium (MPC) under project MPC-588.

Disclaimer

The contents of this report reflect the views of the authors, who are responsible for the facts and the accuracy of the information presented. This document is disseminated under the sponsorship of the Department of Transportation, University Transportation Centers Program, in the interest of information exchange. The U.S. Government assumes no liability for the contents or use thereof.

ABSTRACT

A new method for building seismically resilient bridges is proposed using accelerated bridge construction (ABC) methods. The hybrid two-column bridge bent consists of post-tensioned precast concrete columns with a buckling restrained brace (BRB) as an external energy dissipation device. The design of initial post-tensioning forces and the selection of the appropriate strength of the BRB is provided. The connection design for such configuration considering the free rocking of the columns and the experimental performance of the hybrid bridge bent subjected to cyclic loads is presented. The BRB used had two steel cores; the first BRB steel core fractured during the 5.0% drift ratio, and the second steel core fractured during the 6.0% drift ratio. The two unbonded post-tensioned (PT) bars of the west column yielded after fracture of the BRB steel cores, while the two PT bars of the east column did not yield. The precast concrete elements of the hybrid bridge bent remained undamaged up to 6.0% drift ratio. The longitudinal mild steel bars of the columns did not yield until the 6.0% drift ratio. The gusset assemblies at the cap beam and the footing remained elastic. The damaged BRB could be easily replaced after an earthquake, and the steel gussets could be used to re-center the bridge bent; thus, the proposed system is promising for constructing resilient bridges using ABC methods in high seismic regions that should remain functional after an earthquake.

This report also contributes to development of an analytical model and modeling approach of a double rocking bridge bent consisting of two octagonal columns with two post-tensioned bars each and detached joints using OpenSees. The modeling of rocking mechanisms at the joint of the precast members that are joined by PT bars and BRB as external energy dissipation devices is discussed. The results of the analytical modeling of such hybrid bridge bents under quasi-static cyclic loads are discussed and compared with the experimental results. Numerical simulation demonstrates that the results from the analytical model agree with the experiments in terms of structural response, cumulative hysteretic energy, and joint movement of the test specimens. The response of the BRB is well captured by the analytical model, and the exact amount of energy dissipated by the energy dissipator was obtained and compared to the total amount of the energy dissipated by the bent. The influence of adding an energy-dissipating element on the performance of the bridge bent is analyzed.

The numerical model is subsequently extended to a previously tested three-column bridge bent for a configuration, which included two BRBs. A fiber-based bridge bent model, which includes soil-structure interaction (SSI) using simplified springs, is built. Seismic analyses of hybrid bridge bents using far-field and near-field ground motions show that the hybrid bridge bent displays superior performance.

TABLE OF CONTENTS

LIST OF FIGURES

LIST OF TABLES

EXECUTIVE SUMMARY

A new hybrid bridge system for accelerated bridge construction in seismic regions is developed where precast post-tensioned columns are combined with a buckling restrained brace (BRB). This is the first time columns reinforced with unbonded post-tensioning (PT) bars are combined with a BRB in a hybrid bridge system. A 42% reduced scale bridge bent specimen with columns reinforced with unbonded PT bars employed as re-centering elements and a BRB used as an external energy dissipator was tested under cyclic loads. A diagonal BRB was connected from the footing at one end to the cap-beam at the other end. A quasi-static cyclic load along with a vertical axial load, simulating gravity, were applied to the cap beam to determine the seismic capacity and rocking behavior of the hybrid bridge bent. The hysteresis curves of the bridge bent were stable and symmetric. The specimen showed superior lateral displacement capacity with rocking at the joints under large rotations. The BRB yielded at 1.5% drift ratio and fractured at 5.0% drift ratio. The combination of axial load and post-tensioning force through the PT bars was able to re-center the system; the residual drift ratio was 2.3% when the BRB fractured. The PT bars yielded only after complete fracture of the BRB at 6.0% drift ratio. Not even hairline cracks were observed in the precast column throughout the test, which demonstrates the seismic resilience of the bridge bent system. A numerical model was developed in OpenSees and compared with the experimental results. The numerical model was able to capture the initial stiffness, lateral strength, hysteretic energy dissipation, PT bar force levels, and BRB response with a very good match. The hybrid bridge bent with a BRB displays superior seismic performance under simulated earthquake excitations. Moreover, the replaceable feature of the BRBs makes the hybrid bridge bent seismically resilient; the bridge can recover immediately after an earthquake and remain operational. It is recommended that hybrid bridge bents with BRBs can be used in seismic zones due to their reduced residual displacement and higher hysteretic energy dissipation in strong earthquakes.

LIST OF ACRONYMS

2D-FEM	2-dimensional Finite Element Model
3D-FEM	3-dimensional Finite Element Model
AASHTO	American Association of State Highway and Transportation Officials
ABC	Accelerated Bridge Construction
ACI	American Concrete Institute
AISC	American Institute of Steel Construction
ASCE	American Society of Civil Engineers
ASTM	American Society of Testing and Materials
BRB	Buckling Restrained Brace
BRBF	BRB Frame
Caltrans	California Department of Transportation
CBF	Concentrically Braced Frames
CDF	Cumulative Distributive Function
CFT	Concrete Filled Tube
CIP	Cast-In-Place
CPFD	Cap Pocket Full Ductility
DAD	Damage Avoidance Design
DBE	Design Basis Earthquake
DCR	Dissipative Controlled Rocking
DS	Damage States
FEM	Finite Element Model
FHWA	Federal Highway Administration
GM	Ground Motion
GSS	Grouted Splice Sleeve Connectors
IM	Intensity Measure
LRFD	Load and Resistance Factor Design
LVDT	Linear Variable Differential Transducer
MCE	Maximum Considered Earthquake
MSA	Multiple Stripes Analysis
OpenSees	Open System for Earthquake Engineering Simulation
PEER	Pacific Earthquake Engineering Research Center
PGA	Peak Ground Acceleration
PPT-CFFT	Precast Post-Tensioned Concrete-Filled Fiber Tubes
PRESSS	Precast Seismic Structural System
PT	Post-tensioning
PVC	Polyvinyl chloride
PU	Polyurethane
RC	Reinforced Concrete
SCBF	Special Concentrically Braced Frames
SDC	Seismic Design Criteria
SEI	Structural Engineering Institute
SLA	Stretch Length Anchor
UDOT	Utah Department of Transportation
USGS	United States Geological Survey
WP	Work Point
YLR	Yield Length Ratio

1. INTRODUCTION

Most of the existing roadway system in the United States was built over 50 years ago and is showing signs of increasing deterioration. Approximately 210 million daily trips are taken across structurally deficient bridges in the United States. The mean age of the nation's bridge structure is over 40 years, and most of them are nearing the mean design life of 50 years (Tang 2014). Many of these bridges located in and around seismic regions are vulnerable to earthquakes. Most of these deficient bridges need to be repaired or retrofitted, if not replaced, as soon as possible. The repair cost is equivalent to building a new bridge at the existing site. Moreover, the traditional method of building or retrofitting bridges takes a long time. Construction activities related to bridge rehabilitation and replacement contribute to traffic congestion and increased safety hazards. Accelerated bridge construction (ABC) bridges could eliminate many of the problems specified by demolishing and constructing new bridges in record time. Construction takes an even shorter time when building new bridges with ABC methods. Bridges constructed with ABC methods should sustain minimal damage and have a high re-centering capability in high seismic regions. The seismic resilience of bridges improves the safety and livability of communities. ABC seismically resilient bridges are essential for a transportation system, ensuring the protection and functionality of important bridges even after significant seismic events. A resilient self-centering hybrid bridge bent in high seismic regions, constructed using ABC technology, which could be built within a few days and could dissipate significant hysteretic energy and self-center itself is an attractive choice.

Monolithic bridges are prone to seismic events since these bridges have suffered heavy damage during previous earthquakes. Many bridges have been built using the ABC technique in non-seismic U.S. regions during the past two decades because it offers many advantages. Generally, prefabricated reinforced concrete components are assembled to form the desired structure in ABC construction technology. If structures are poorly designed using ABC, they might suffer significant damage during a large earthquake. The damage is mainly concentrated in the connection regions, which permanently damages the load-carrying vertical members such as the columns; moreover, there is a chance of complete bridge collapse.

The Northridge earthquake (1994) is one of the costliest natural disasters in U.S. history. It affected northern Los Angeles, the San Fernando Valley, and surrounding areas in southern California. More than 5,000 injuries were reported, and around 65 deaths were recorded. Property damage was estimated at $15 billion to $30 billion. The newly built bridges and post-1987 retrofitted reinforced concrete (RC) bridges performed reasonably well. Among seven bridges that collapsed in the Northridge earthquake, five had been scheduled as requiring retrofit, whereas two bridges were identified as not needing retrofit. The collapsed structures can be distinguished into three categories: three bridges designed and constructed before the 1971 San Fernando earthquake; two bridges designed before 1971 but construction finished after 1971, and two bridges designed and constructed a few years after the 1971 San Fernando earthquake but not to current standards. All the damaged bridges were built with monolithic or cast-in-place (CIP) construction. Most bridges have been designed and constructed as traditional monolithic construction for the past several decades in the U.S. During the 1994 Northridge earthquake, some important bridges were not operational; these were primary routes and were closed for emergency and public traffic.

CIP construction methods include a traditional method of building the structure on site. Bridges are erected on site with the bottom-to-top approach, which includes constructing the substructure first and then building the superstructure. The initial cost for building these bridges is low, but requires a longer construction time, more construction workers, and more resources. Moreover, monolithic construction of bridges results in severe traffic disruption, which is worse in urban areas where traffic congestion is very high. Current seismic design specifications depend on the bridge substructure system acting in a ductile manner and inelastically for monolithic construction during a seismic event. This design approach intends to absorb the seismic energy in the predefined locations in a bridge substructure called plastic hinge

zones. In the plastic hinge regions, a series of events occur, such as spalling and crushing of the concrete, and yielding, buckling, and ultimately fracture of the longitudinal steel rebar.

CIP construction has been in practice since the late 1970s and was introduced in many countries around the world; it has helped avoid a complete collapse of several bridge structures in strong earthquakes. This methodology targets life safety and collapse prevention performance levels during a design basis earthquake (DBE) and maximum considered earthquake (MCE), respectively. In an actual earthquake, the bridge may undergo large residual displacements and damage beyond repairability. The worst part is that the bridge might not function immediately after the earthquake, making urgent emergency relief impossible. The 2011 Christchurch earthquake has highlighted complexities in evaluating the future performance of bridges and repairing plastic hinge regions in traditional monolithic structures (Routledge et al. 2016). Past earthquakes have exhibited that even though monolithic structures are built at a DBE or MCE, a damaged bridge needs extensive repair or possible replacement. Hence, downtime, high repair cost, large residual displacements, and potential replacement are the disadvantages of CIP bridges.

In strong earthquakes, collapse or loss of functionality of a bridge show that traditional monolithic construction focuses only on the initial lower construction cost and might impact immediate functioning or prevention of collapse during an earthquake. These unfortunate results lead to a structured design methodology that the bridges should be constructed using the correct design procedure following current seismic codes. Moreover, current construction techniques should aim to design novel bridges with efficient seismic performance features, such as faster construction, minimum interruption, repair, and residual displacement after any seismic event. Since seismic specifications have not advanced as the ever-growing techniques of building new bridges using innovative ideas, the construction of durable and earthquake-resilient infrastructure remains a challenge in bridge engineering.

This report presents novel solutions for constructing a seismic-resistant bridge bent using precast concrete structural assemblages for high seismic regions. This design methodology aims to localize all nonlinear deformation in a bridge structure at a fuse-type dissipater. After an earthquake, the dissipater is designed to be easily replaceable, provided the structural members are mostly undamaged. This type of connection reduces damage to the capacity-protected members and residual displacement in a bridge bent; it couples unbonded post-tensioning (PT) elements with an external dissipater to deliver efficient self-centering and energy dissipation in a bridge, respectively. During a design-level earthquake, the hybrid bridge bent will self-center, remain fully functional, and may only suffer minor repairable damage. The initial cost of construction can be considered an impediment but not to a considerable extent; it offers the advantage of minimizing the repair work for a precast bridge bent during its serviceability period. The low damage technologies could justify the higher initial construction cost to infrastructure owners. The proposed system also reduces the costs related to the downtime and replacement of a bridge following a seismic event.

1.1 Accelerated Bridge Construction (ABC)

ABC was developed as an alternative building method to CIP for bridges in non-seismic areas. The Federal Highway Administration (FHWA, 2013) defines ABC as “bridge construction that uses innovative planning, design, materials, and construction methods safely and cost-effectively to reduce the onsite construction time that occurs when building new bridges or replacing and rehabilitating existing bridges.” With ABC, the precast assemblages can be built off-site and transported and assembled on-site. With ABC, new bridges can be constructed faster. Considering the complex nature of skewed, curved bridges, such bridges built with ABC methods can be built with ease. Existing bridges can be replaced in a relatively short time, and retrofit of existing bridges can be done efficiently. ABC construction offers many benefits, such as:

- Quick construction time

- Minimal interruption to traffic during construction, especially in densely populated areas
- Superior quality of the prefabricated components
- Economic design (lower maintenance cost, savings in formwork, fewer human resources)
- Higher accuracy in constructing bridge elements due to their prefabrication
- Improved durability of the structure
- Minimum environmental hazards and impact
- Higher level of safety
- Reduced weight of the structure
- Improved workability under challenging conditions and difficult situations (over water)

In low seismic regions, bridges built using ABC technology can be designed with minimum seismic considerations. Past earthquakes have shown the vulnerability of precast connections in high seismic regions. The demand for superior seismic performance of precast concrete structures was highlighted in earthquakes during the 1970s and 1980s, such as the Loma Prieta earthquake in 1989 (Buckle et al. 1994). Limitations of the ABC technique in moderate-to-high seismic regions are due to uncertainties involving seismic performance and behavior of the connections and interaction between the precast concrete elements. The connections must be easy to construct and robust enough to preserve their structural integrity during a seismic event. ABC connections include bar couplers, grouted ducts, pockets, sockets, and hybrid connections depending on the force transfer mechanism. Three parallel metrics, such as technology readiness, performance, and time savings potential, were used to rank the efficiency of ABC connections. Most of the connections are built with or without PT elements with various energy dissipators attached to the primary structure (Marsh et al. 2011).

Many U.S. bridges are built or rehabilitated using ABC techniques. A recent report discussed rapid removal and replacement of the 4500 South Bridge on State Route 266 over Interstate 215 in Salt Lake City, Utah, during one weekend (Ardani et al. 2010). A few examples of these types of bridges in Utah, which were constructed by the Utah DOT using ABC methodologies, include:

- Bridge over Weber River at Echo Junction
- I-80 Eastbound Bridge at Atkinson Canyon
- Pioneer Crossing in Lehi
- Proctor Lane over I-15, the F-762 bridge on US-6 at approximately MP 220
- Riverdale Bridge
- Sam White Lane Bridge over I-15
- South Layton Interchange over I-15
- SR-66 Bridge over Weber River in Morgan City
- Summit Park Bridge over I-80

1.1.1 Bar Couplers

Bar couplers are used to splice reinforcing bars, allowing a continuous force flow (axial force) through the interface between adjacent precast members (Marsh et al. 2011). The most widely used coupler type in bridges is a steel sleeve filled with high-strength grout after the precast element has been erected. These couplers have a large clearance to allow for field placement tolerance. Jansson (2008) evaluated two grout-filled mechanical reinforcement splices for ABC connections using precast concrete structural elements and discovered that both splices met the American Association of State Highway and Transportation Officials (AASHTO) load and resistance factor design (LRFD) criteria for slip and fatigue. Haber et al. (2015) performed static, dynamic, and cyclic tests on two mechanical reinforcing splices, which could withstand high ultimate stress demands. The grouted splice sleeve connector (GSS) is one of the rebar-splice techniques in ABC connections. It is made of a ductile iron sleeve, which facilitates passing of grout to connect two spliced bars. Ameli et al. (2015) compared the cyclic performance of

precast specimens, which used fastened and grouted splice sleeve connectors, with a cast-in-place specimen. The precast specimens with GSS and the CIP specimen had similar strength capacity. The precast specimens exceeded the drift demand expected of such bridges in large earthquakes and achieved sufficient ductility and curvature distribution that closely emulates CIP construction. In another study, Ameli et al. (2016) and Ameli and Pantelides (2017) examined the seismic performance of GSS connections with the connectors located in the column or footing of a bridge subassembly experimentally and numerically. Improved seismic performance was seen when the GSS connectors were placed inside the footing rather than inside the column. New standard test methods were developed for mechanical bar splices, and more than 160 bar couplers were tested under uniaxial monotonic and cyclic loading to failure to produce a systematic database of coupler performance (Dahal and Tazarv 2020).

1.1.2 Grouted Ducts

Grouted ducts allow individual reinforcing bars from adjacent bridge members to be fully developed into a separate duct. The bar development length can be shorter than the CIP design since the duct provides confinement. Grouted ducts offer larger construction tolerances, but extra space within the adjacent reinforcement cage is required. The grouted duct connection is feasible for ABC connections when sufficient space is available for duct placement. The grouted duct connection contains corrugated steel ducts inside the footing or cap-beam, and the protruded column bar reinforcement is extended inside the ducts and grouted. Since ductility demand is concentrated at the base of the column during a seismic event, the grouted duct connection becomes the most critical part of the structure. Raynor et al. (2002) studied the bond behavior of reinforcing bars grouted in ducts under cyclic loading. The seismic response of precast concrete frames with grouted connections heavily depends on bond slip of the bars at the connection regions. Under monotonic tension loading, Brenes et al. (2006) investigated the response of reinforcing bars grouted in galvanized steel and plastic ducts. Test results indicated that the response was not highly dependent on the variation of the embedment depth but rather it was influenced by the duct material. Based on both test results and an analytical model, Steuck et al. (2009) found that an anchorage length between 6 and 10 times the bar diameter in the grouted duct was sufficient to reach bar yielding and fracture, respectively.

Pang et al. (2010) studied the performance and behavior of cap beam-to-column connections for four 40% scale precast specimens using grouted ducts under cyclic response. The energy dissipated by the precast specimen was slightly smaller than the CIP specimen. The intentional partial debonding of bars implemented over a length of eight times the bar diameter within the ducts was ineffective; bar fracture in all four precast specimens occurred due to low-cycle fatigue. Matsumoto (2009a) found that the grouted duct connection was emulative of the monolithic construction strength, but a compromised displacement capacity was observed from the load-displacement response. The response of two half-scale precast bridge column-to-footing subassemblies connected by means of grouted ducts under cyclic quasi-static lateral load suggests that the grouted duct connection with the implemented detailing was feasible in terms of hysteretic performance, strength, and displacement capacity (Tazarv and Saiidi 2015). Hofer et al. (2021) investigated the cyclic behavior of a column-to-foundation joint for precast concrete elements adopting corrugated steel ducts embedded into the foundation, in which column protruding rebars are anchored and grouted by high-performance mortar. All six full-scale specimens showed a ductile flexural failure with plastic hinge formation at the base of the column.

1.1.3 Pocket Connection

Pocket connections connect bridge columns to precast cap beams or footings by placing a circular corrugated steel duct inside the cap beam, which forms the pocket. The protruded bars from the column are extended into the pocket, which is filled with high-strength concrete grout. The pocket connection has displayed good seismic performance. This connection contrasts with the member socket connection,

where the whole end of a precast member is embedded in the other member. Using experimental pullout tests, Matsumoto et al. (2008) investigated the anchorage behavior of straight and headed reinforcing bars embedded within grout pockets and grouted ducts. Matsumoto (2009b) performed an experimental study of two precast column-to-cap beam joints with the pocket connection. Compared with the CIP specimen, the precast specimens had equivalent strength and ductility to the CIP specimen. The cap pocket full ductility (CPFD) specimen satisfied the performance objective of the design, attaining an extensive drift without showing extensive plastic hinging of the column, had limited joint distress, no significant strength deterioration, and essentially elastic behavior of the bent cap (Restrepo et al. 2011). The pocket connection for column-to footing joints with a two-column bridge bent was experimentally tested using a shake table test, where the column plastic hinge regions were improved with engineered cementitious composite and a concrete-filled fiber-reinforced polymer. Damage was not observed at the connection (Motaref et al. 2011). Mehrsoroush and Saiidi (2016) tested pocket connections of pier models of circular columns in the cap beam. The embedment length was adequate to develop moment connection capacity and form plastic hinges in the columns; the embedment length was 1.2 and 1.0 times the column diameter, respectively. Mohebbi et al. (2018) conducted shake table studies and analysis of a large-scale post-tensioned precast bridge column connected to a precast footing using a pocket connection. The pocket connection was successful in developing a plastic hinge in the column with no connection damage.

1.1.4 Socket Connection

The socket connection is a new type of ABC connection where a spread footing is cast around precast concrete bridge columns. High-strength grout or a concrete closure pour is cast between the two precast members. First, a precast column is erected on the excavated level land, and the reinforced concrete footing is cast around the column. A theoretical and experimental analysis was conducted to analyze the transverse wall performance of the socket connection of a precast concrete structure (Canha et al. 2009). Haraldsson et al. (2013) examined a 42% scale of a prototype bridge with socket connections where effects of footing reinforcement and socket depth were analyzed. The performance of all three precast specimens with socket connection under cyclic lateral load was better than an equivalent cast-in-place specimen. Four 1:3-scale bridge column specimens were investigated both experimentally and numerically (Wang et al. 2018); the specimens consisted of two CIP columns and two precast concrete columns using socket and pocket connections; the specimens with pocket and socket connections had the same, if not better, level of seismic performance as CIP construction (Wang et al. 2019). Based on shake table tests of two large-scale models, a pocket and socket connection for RC two-way hinges at column bases was assessed, one with a pocket in the column and the other with a socket in the footing; both configurations exhibited satisfactory seismic behavior for use in high seismic areas (Jones et al. 2020).

1.1.5 Hybrid Connections

Hybrid connections are ABC connections that use unbonded PT elements and mild steel reinforcement passing through joint interfaces of structural members. In addition to mild steel, hybrid connections may also include other energy dissipating elements such as stretch length anchors, small localized buckling restrained braces (BRBs), angle sections, and bolted T-stubs. The joints between precast members start to rock when the seismic moment increases since the joints are not monolithic; the concentrated rotation at the joint accommodates all the member displacement; the precast member does not undergo any plastic deformation, and damage to the member is minimized (Marsh et al. 2011). The unbonded tendon can elongate evenly along its entire length. The joint opening causes only a small strain increment in the tendon, thus the tendon remains elastic. The PT tendon generates the elastic restoring force to the system, which minimizes the residual drift and promotes self-centering.

1.2 Hybrid Construction of Bridge Bents

The seismic performance of a bridge bent built with the ABC construction method, which has only PT elements connecting the prefabricated members, must be studied to evaluate the level of damage during a seismic event. This gives rise to the idea associated with strengthening an existing bridge bent built with PT elements; appropriate sacrificial elements can be introduced to limit any damage to the load-carrying member and joints. The presence of a BRB in a post-tensioned bridge bent can be an ideal method for mitigating the damage to essential bridge bent elements, such as columns, along with minimal residual displacements and maximum energy dissipation. The proposed hybrid solution consists of post-tensioned precast concrete columns in a two-column bridge bent with a BRB as the external energy dissipation device. In the second part of the research, the bridge bent was tested without a BRB to determine the energy dissipating device's contribution and the bridge bent's capacity without the BRB. The developed analytical model for ABC construction can accurately predict the response during an earthquake and improve the structure's performance. Even though many analytical models have accurately matched experimental results, extending such models to new configurations still poses many challenges. In precast post-tensioned concrete construction, the structure's common and general behavior pattern is hard to establish due to the many complexities involved with such structures, leading to problems in developing models for bridges that have not yet been built. In seismic regions, the development of analytical models to predict the behavior of a hybrid bent is an important step toward designing the appropriate bridge bent parameters using ABC methods. The functionality of a bridge after a DBE or MCE seismic event can be determined with a good numerical model. A functional roadway system following a seismic event saves lives and protects the economy. Moreover, if bridges preserve their integrity during an earthquake the community will feel less vulnerable and safer.

Two construction methods for bridge design for high seismic regions are compared in Table 1.1. Even though CIP construction has a lower initial cost than the hybrid bridge bent built with ABC, the project's total cost would be relatively high. The lower residual displacement, higher energy dissipation, and stiffness of the hybrid bridge bent make it superior over the CIP bridge bent. Hybrid bridge bents built with ABC technologies can be the future of bridge design, and appropriate seismic design considerations should be incorporated for efficient application. ABC techniques, high performance and durable materials, and advanced earthquake technologies, are important aspects for the next generation of bridges. The serviceability life of new bridges can be prolonged to 100 years with negligible maintenance costs by utilizing improved materials and advanced construction technologies. The goal of seismic bridge engineering in the next 20 to 30 years would be to preserve the functionality and operation of bridge structures even after a maximum credible earthquake event (Palermo and Mashal 2012).

Table 1.1 Comparison of construction methods

	CONSTRUCTION METHOD	
Parameters	**Cast in place (CIP)**	**ABC with hybrid bridge bent**
Structure cost	Low	Medium
Construction duration	High	Low
Maintenance cost and duration	Medium	Low
Post-earthquake repair cost and duration	High	Low

1.3 Rocking Systems in Post-tensioned Concrete Bridge Construction

During the Chile earthquake of May 1960, Housner (1963) discovered that several elevated water tanks survived the ground shaking because of uplift despite instability, while much more stable appearing RC elevated water tanks were severely damaged. Clough and Huckelbridge (1977) studied the effects of allowing column uplift in a three-story steel frame responding to seismic loading. Allowing column uplift reduced the seismic loading and ductility demand compared with a fixed base response for a similar input motion. Using a response-spectra approach and equivalent elastic characteristics, a simple design method for evaluating maximum rocking displacements was proposed and compared with outcomes from simulated seismic excitation of the model using an electro-hydraulic shake-table (Priestley et al. 1978). Aslam et al. (1980) conducted an analytical and experimental study of earthquake-induced rocking and overturning response of rigid blocks, which was motivated to establish safe design criteria for radiation shielding systems under strong-motion earthquakes.

Experimental studies on rocking incorporated in bridge and building structures started in the 1990s. The methodologies of rocking soften the connection between the column-footing interface and beam-column joints. Roh (2007) used "rocking columns" to reduce the structural strength of a rocking system for controlling the story accelerations; rocking columns were employed for weakening, and supplemental viscous dampers were added to reduce story displacements. The controlled rocking system displayed excellent self-centering properties, and replaceable fuse elements were efficient for energy dissipation and structural damage in stiff steel braced frames was negligible and remained virtually elastic (Eatherton et al. 2008). The seismic response of 1/3-scale, three-story steel frames with columns permitted to uplift was assessed and compared with fixed-base frames using three-dimensional shake table tests; maximum base shears of rocking frames were reduced compared with fixed base frames in both longitudinal and transverse directions (Midorikawa et al. 2009). Wiebe and Christopoulos (2009) suggested that incremental forces due to higher mode effects may be substantially decreased by allowing rocking at several locations over the height of a base-rocking structure. Roh and Reinhorn (2010) performed physical experiments of rocking columns, and an analytical model was developed using IDARC2D to evaluate several alternatives of weakening using rocking RC columns.

Dissipative controlled rocking (DCR) systems with external and internal dissipation devices were used to improve the seismic performance of ABC bridge structures (Mashal et al. 2012). A shake table test was performed on a post-tensioned bridge bent, where columns did not experience any damage by allowing the columns to rock on specially detailed ends (Thonstad et al. 2016). An inerter, which is a kind of two-terminal inertia element, was employed to resist forces proportional to the relative acceleration, which are combined with a clutch to oppose the relative motion and control the seismic response of rocking structures (Thiers-Moggia and Málaga-Chuquitaype 2019).

The precast concrete frame partially bonded and unbonded PT tendons can sustain large lateral displacement but they must have minimal residual deformation and insignificant structural damage (Priestley et al. 1999). A precast, prestressed concrete framing system with both unbonded post-tensioned reinforcement and bonded bar reinforcement displayed superior performance to conventional cast-in-place moment frames (Stanton et al. 1997). Mander and Cheng (1997) tested a near full-scale precast post-tensioned bridge pier to validate the generalized displacement-based seismic design, incorporating damage avoidance design (DAD); the bridge pier performed in a bilinear fashion without significant damage to the structural components. El-Sheikh et al. (1999) studied the performance of two six-story unbonded post-tensioned frames using nonlinear pushover static and time-history dynamic analysis. Numerical analysis showed that unbonded post-tensioned precast frame strength, ductility, and self-centering capability were more than adequate for severe earthquake loading.

The performance of four unbonded post-tensioned precast concrete segmental bridge columns under lateral earthquake loading was evaluated, where steel jackets were used to confine the plastic end region of each column (Hewes and Priestley 2002). Quasi-static cyclic tests of precast segmental columns incorporating unbonded PT strands showed superior recentering properties until the PT element yielded after a 9.0% drift ratio (Billington and Yoon 2004). Two unbonded post-tensioned, precast concrete-filled tube (CFT) segmental bridge columns were examined to evaluate the seismic behavior under cyclic loading (Chou and Chen 2006). Both specimens displayed higher self-centering up to 6.0% drift ratio without any significant damage; however, equivalent viscous damping was higher for the specimen incorporating external energy dissipators. Three 1:3 scale unbonded, post-tensioned cantilever bridge piers suffered minimum damage compared with a CIP specimen; recentering properties were also high for the post-tensioned specimen (Marriott et al. 2009). The seismic performance of precast segmental unbonded post-tensioned bridge columns in regions of high seismicity was examined experimentally (Ou et al. 2010a). Ou et al. (2010b) also tested three large-scale precast segmental RC columns under cyclic load. Unbonded PT bars were used as a self-centering material, and internal energy dissipators used were bonded mild steel, unbonded mild steel, and bonded high performance (HP) bars, respectively.

The seismic performance of precast post-tensioned concrete-filled fiber tube (PPT-CFFT) bents was compared with a monolithic moment resisting concrete bent using cyclic tests. The PPT-CFFT bents did not suffer any significant damage or residual displacement (ElGawady and Sha'lan 2011). Proper selection of durable materials with enhanced mechanical properties and appropriate detailing promotes the longevity of post-tensioned precast systems (Palermo and Mashal 2012). Experimental observations and results for two half-scale bents of a typical highway bridge with a 16-meter span in New Zealand were provided by Mashal et al. (2012). The first bent incorporated an emulative CIP solution, and the second a low damage specimen with a central PT bar and external replaceable seismic energy dissipators that displayed excellent self-centering properties. Segmental cantilever columns incorporating internal post-tensioned and slip-dominant (SD) joints displayed excellent recentering properties due to the presence of PT elements (Sideris et al. 2014). A shake table test on a large-scale (1:2.4) novel segmental concrete single-span bridge specimen, also called hybrid sliding–rocking bridge, that incorporated a box-girder superstructure with rocking joints and internal PT tendons and two single-column piers with internal unbonded PT displayed minimum residual displacements (Sideris et al. 2015).

Precast construction using PT elements such as all-thread high strength steel bars effectively limits residual displacements during large earthquakes (Guerrini and Restrepo 2015). The Wigram-Magdala Link Bridge was presented as a case study to illustrate the design method and detailing leading to low-damage; the bridge was constructed with a central unbonded PT bar in each column (Routledge et al. 2016). Two non-emulative precast column-footing connections, including central post-tensioning, were compared with an emulative connection; the post-tensioned specimens suffered only minor damage (White and Palermo 2016). DCR connections, which combine unbonded PT bars and externally attached metallic dissipaters in the bridge bent, displayed higher self-centering and energy absorption capabilities for the bridge, respectively (Mashal and Palermo 2019). Although quasi-static and shake table tests have been performed on CIP two-column bridge bents, few tests have been carried out with two-column bridge bents using post-tensioned columns without energy dissipators (Han et al. 2019). Efficient self-centering with less than 1.0% residual drift was observed for specimens with and without external energy dissipators. A two-column bridge bent using PT bars inside the two columns along with stretch length anchors (SLA) displayed excellent self-centering properties (Thapa and Pantelides 2021).

1.4 Buckling Restrained Braces (BRB)

During a seismic event, the manner in which the inertia energy, kinetic energy, and dissipative energy are absorbed by a structure determines the damage level. It is not economically feasible to dissipate the seismic input energy within elastic capacity. Bridges should be designed so that the structural members or dissipators yield in a controlled and ductile manner. The concept of structural fuses specifies that dissipators should be designed as sacrificial elements that absorb damage during an earthquake through repeated cycles of loading and limit damage to protected structural components. A BRB is a very efficient structural fuse element.

The BRB brace concept and construction were first discovered in Japan in the early 1980s (Ko and Field 1988), and actual testing was carried out in the mid-1980s by Watanabe et al. (1988). BRBs were implemented in Japan in the 1990s. After successfully using BRBs on numerous Japanese projects, Arup started using BRBs in buildings in California in 1999 (Field and Ko 2004). The technology was transferred to the United States because of its good seismic performance; testing and simulation were also carried out simultaneously, and BRBs were safely and routinely implemented in important projects after 2000. The first BRB tests in the U.S. were performed at UC Berkeley from 1999 to 2000 (Field and Ko 2004). The results from the comprehensive test program demonstrated that BRBs deliver ductile, stable, and repeatable hysteretic behavior. The BRB was codified as a lateral-force-resisting system in ASCE 7-05 and AISC 341-05 and has been integrated into more than 450 U.S. buildings (Robinson et al. 2012). The components of a BRB are the casing, filler material, steel core, and debonding agent as shown in Figure 1.1 (Xu and Pantelides 2017).

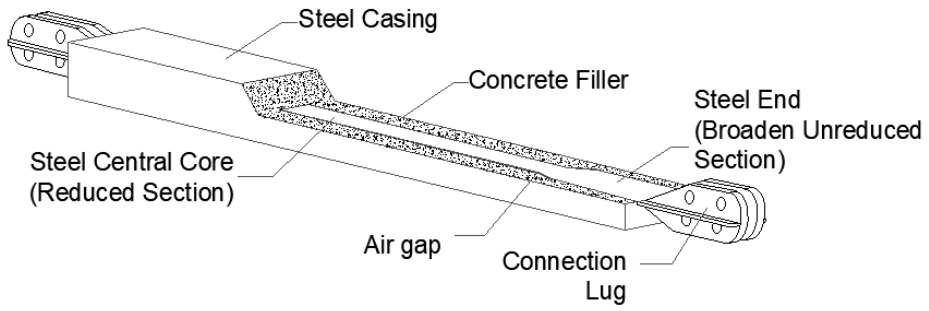

Figure 1.1 Schematic drawing of BRB

The steel core is the central yielding zone, and the transition zones, which have a thicker area than the central steel core, are located at either side of the yielding zone. The connection zones that extend past the sleeve are connected to the gusset plates. The steel casing is the outer part of a BRB that covers the concrete mortar and steel core. BRBs do not display any of the unfavorable behavior characteristics of conventional braces, such as buckling under compression forces. BRBs have balanced hysteretic behavior with compression yielding similar to tension yielding, as shown in Figure 1.2. A BRB absorbs energy by yielding in compression and tension; the magnitude of the tensile force is related to the steel core material properties. When the steel core is unbraced, buckling in compression leads to a loss in stiffness, progressive degrading behavior, and reduced energy dissipation ability. By enclosing the steel core over its length in a steel tube filled with concrete mortar, buckling of the central steel core is prevented. Thus, significant compressive strength is generated since the steel core is confined. A slip surface or unbonded layer between the surrounding concrete and the steel core allows the steel core to elongate or shorten without large wave buckling but rather with short wave buckling. As a result, adequate flexural strength and stiffness inhibit the brace's global buckling, and this allows the steel core to undergo fully reversed

axial yield cycles without loss of strength or stiffness; this leads to similar strength in tension and compression.

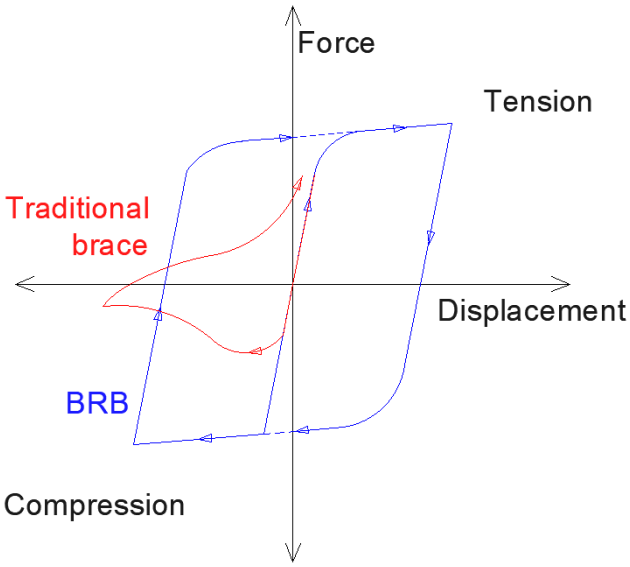

Figure 1.2 Comparison of the hysteresis behavior of a traditional brace and a BRB

A typical BRB can undergo several cycles of inelastic deformation during an earthquake without degradation or fracture since it has nearly identical behavior in tension and compression. The strains are distributed over a large range; thus, the BRB has a higher energy-dissipating ability than most dissipators. Moreover, the low-cycle fatigue life of a BRB is well over the demands obtained from nonlinear dynamic analysis under typical earthquakes. BRBs do not fracture under the demands imposed by maximum considered earthquakes when correctly designed according to seismic codes. Hence, BRBs improve the ductility and energy dissipation ability of the structural frames, known as BRB frames (BRBFs), they are attached to. BRBFs are proportioned using the fundamental philosophy of all ductile systems for seismic design. The BRBs are the yielding elements, which are sized for a reduced seismic force level and undergo significant inelastic deformation during a design-level earthquake, while all other elements in the system are capacity-designed so that they remain essentially elastic at the expected strength of the BRBs (Kersting et al. 2015). In the BRBF system, the BRB is the critical element that harnesses the inherent ductility of a steel core and offers stable and predictable energy dissipation without reliance on a global brace-buckling mechanism used in other concentrically braced frames (CBFs) and special concentrically braced frames (SCBFs). Since cyclic loading is not as reliable in CBFs and SCBFs, efficient and stable energy dissipation is impossible during seismic events. Superior performance and reduced drift levels are thus achieved using BRBFs rather than CBFs or SCBFs. Moreover, the increased stiffness of the BRBF due to the BRB helps reduce the maximum displacement of structures during a seismic event (Kim and Choi 2004).

Different types of BRBs have been invented to increase energy dissipation and reduce residual drift of structural systems. The use of low-strength steel for a BRB, which undergoes large plastic deformations and dissipates more energy, is beneficial for reducing structural damage (Kim and Choi 2004). A core plate sandwiched between two restraining members was made of a flat plate, channel and in-filled concrete, with fully tensioned A490 bolts to form a BRB (Chou and Chen 2010). Numerical analysis of an all-steel BRB was performed by varying the buckling restraint mechanism (BRM) and the gap between the core and the BRM (Hoveidae and Rafezy 2012). A simple expression was proposed for predicting the residual drift ratio of low-to-high rise BRBFs based on analytical results (Sahoo and Chao 2015). The

performance of new BRBs with similar total steel core areas was satisfactory, which dissipated similar amounts of hysteretic energy compared with conventional BRBs. Strong axis buckling of the steel core can be avoided by restricting the steel core width for a given dimension of steel casing (Xu and Pantelides 2017).

In bridges, only a few examples of using BRBs exist even though its application in buildings is widespread. BRBs have been used as an energy-dissipating element in a monolithic bridge bent as a retrofit technique to increase the lateral load-carrying capacity (El-Bahey and Bruneau 2011; Bazaez and Dusicka 2016; Wang et al. 2016; Upadhyay et al. 2019). BRBs help the structure dissipate seismic energy and improve seismic performance in the transverse direction (El-Bahey and Bruneau 2011).

In summary, a BRB consists of an outer steel thin cover, a central steel core, a concrete filler around the core (that supports the core and avoids buckling under axial compression), and a debonding agent, such as an air gap that inhibits undesired contact between the core and the filler. A BRB is a structural brace, constructed to ensure the structure where it is fixed upon to undergo large cyclic lateral loading, such as earthquake-induced loading. Ductile BRBs can absorb a large amount of energy during seismic events through repeated hysteretic loops. Preventing buckling of the steel core during compression allows a similar strength in tension and compression.

1.5 Hybrid Bridge Bents

Hybrid bridge bents are unbonded post-tensioned concrete elements connected by PT strands or bars at the joints and having additional energy-dissipating elements. During an earthquake, residual displacement in these bridge bents should remain low because of the post-tensioning effect of the PT bars or strands. PT bars or strands are either unbonded or bonded to provide self-centering. When the yielding of PT bars or strands is prevented, post-tensioning forces generate the restoring force required to self-center the system and eliminate residual deformations (Billington and Yoon 2004). However, the system does not perform well if the PT bars or strands yield at small drift ratios. Energy dissipating devices can be used along with PT bars or strands to avoid large displacements in strong earthquakes (Marriott et al. 2009).

The idea of hybrid self-centering structural behavior first began after rocking was combined with a hysteretic energy dissipation device in the stepping railway bridge over the South Rangitikei River in New Zealand (Cormack 1987). This innovative idea was applied to concrete moment frames; two unbonded post-tensioned, precast concrete beam-to-column joint sub-assemblages were tested under cyclic reversals of inelastic displacement. These frames had insignificant damage in the joints and could be easily repaired after an earthquake (Priestley and MacRae 1996). Stanton et al. (1997) concluded that precast prestressed concrete frame performance was superior and displayed essentially no residual drift compared with a conventional cast-in-place moment frame.

Hybrid rocking construction has been extensively used in single-column bridge piers (Billington and Yoon 2004; Ou et al. 2010; Palermo et al. 2007). The design methodologies, modeling aspects, and experimental results of quasi-static cyclic tests on five 1:3 scaled bridge pier specimens were presented by Palermo et al. (2007). In four hybrid configurations, when compared with a monolithic CIP benchmark specimen, minimum damage and negligible residual/permanent deformation were seen in the hybrid specimens (Palermo et al. 2007). Solutions have been developed for energy dissipation after performing analytical studies and quasi-cyclic tests on monolithic, purely rocking, and seismically resistant hybrid concrete columns (Marriott et al. 2009). Large-scale experiments performed on single-precast segmental post-tensioned bridge columns showed that the desired ductility and self-centering could be easily attained for use in high seismic regions (Ou et al. 2010; Sideris et al. 2014).

Cyclic tests performed on post-tensioned precast concrete dual shell columns with supplemental energy dissipation devices showed that the columns effectively attained self-centering up to an imposed 3.0% drift ratio (Guerrini et al. 2015). Two-column precast concrete bridge bents have also been tested using hybrid connections (ElGawady and Sha'lan 2011); insignificant damage and residual displacement was observed in the post-tensioned specimens. Shake table tests of hybrid concrete bridge columns and double-column bridge bents have displayed negligible residual displacements (Cheng 2008; Marriott et al. 2008; Motaref et al. 2014). Non-linear analysis of hybrid bridge bents confirms that they display excellent seismic resilience (Kwan and Billington 2003a, 2003b; Upadhyay and Pantelides 2018; Chou et al. 2013; Bu et al. 2016a, 2016b). However, current hybrid bridge bents have not used any diagonal elements such as a BRB as an energy dissipating device. A hybrid bridge bent was designed to create a resilient bridge that could perform well and eliminate or limit damage to the primary structural components in an earthquake; the bridge bent is comprised of precast concrete elements in a two-column bridge bent whose columns are post-tensioned with unbonded PT bars with a diagonal BRB as an external energy dissipation device.

2. DESIGN AND CONSTRUCTION OF BRIDGE BENT

2.1 Description of Riverdale Bridge Bent

The prototype bridge bent is inspired by the post-tensioned Riverdale bridge bent located in Utah. As seen in Figure 2.1, the total length of the bridge is 152 ft 6 in. (46.5 m), with two uniform spans along the sloping ground (UDOT 2008). Three bridge bents support the deck with a width of 170 ft 10 in. (52.1 m) at the top. In every line of support, there are four two-column bridge bents, which have mirror symmetry. These four bridge bents are not linked to each other directly through any connection beside the supporting deck at the top. All of the bridge bents have two octagonal columns, one cap beam and two footings, as shown in Figure 2.2. There are three supporting lines along with bridge bent #1, bent #2, and bent #3, as seen in Figure 2.1. Bridge abutments are present at support lines for bent #1 and bent #3. There are four two-column bridge bents at support line of bent #2. There is one independent footing for every column; the footings are fixed to the ground with numerous piles. There are two different sizes of footings; of the eight footings, six are rectangular 11 ft long, 13 ft 6 in. wide, and 4 ft deep (3.353 m x 4.115 m x 1.219 m), and the middle two footings are 11 ft long, 12 ft wide, and 4 ft deep (3.353 m x 3.658 m x 1.219 m). At the center of the footing, there is a recess of extending 3 in. (76 mm) clear in the radial direction and 4 in. (102 mm) deep to accommodate the column where the bedding grout is filled between the column and footing interface, as shown in Figure 2.3. The arrangement of the grout inlet tube is present inside the footings to fill the grout once post-tensioning is achieved. Nominal reinforcement is provided in the footings, which are designed according to the criteria of ACI 318-14, and at the place where the PT bars start, extra reinforcement is provided. A dead anchor is used as a means to hold down every PT bar in the footings. Six PT bars or rods are present, and these rods extend to columns.

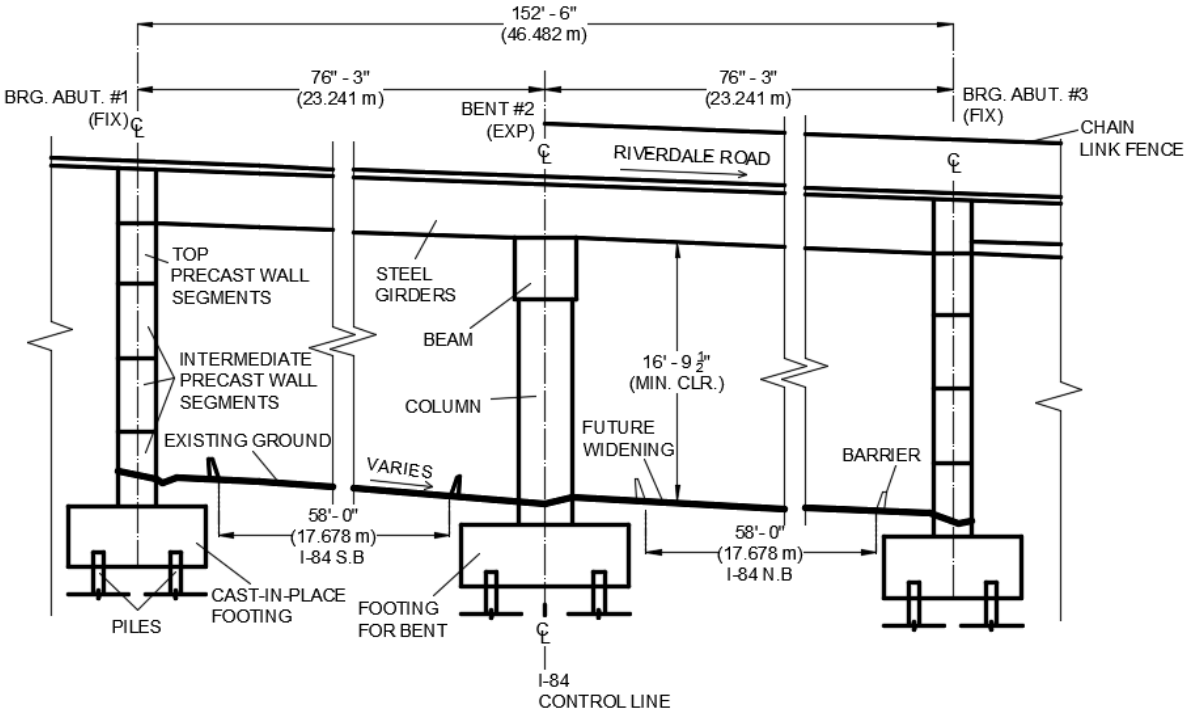

Figure 2.1 Riverdale bridge elevation (Elevation normal to highway I-84)

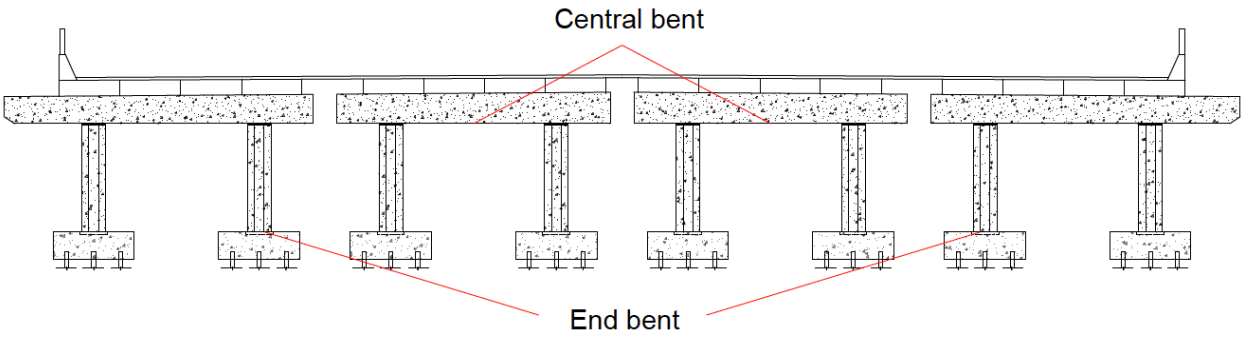

Figure 2.2 Section at Bent #2

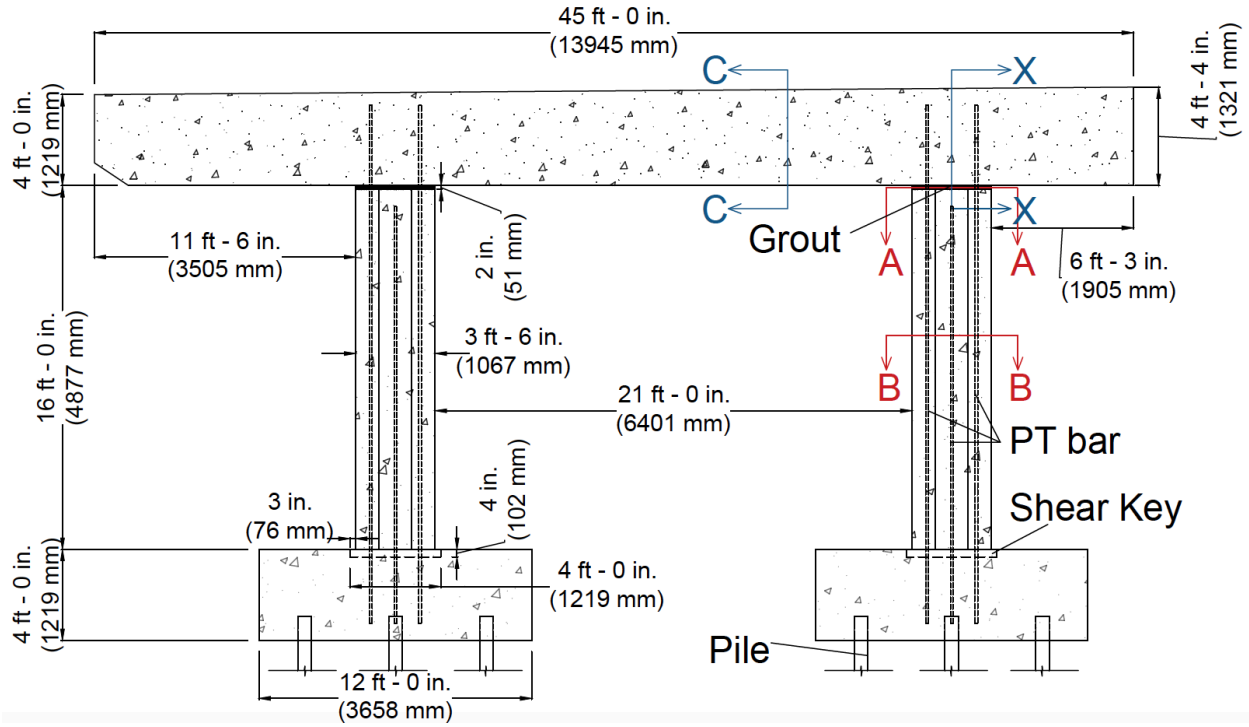

Figure 2.3 End bent of Bent #2

The grade of the reinforcing bars used at the bridge bent is Grade 60, while the concrete compressive strength of all the precast elements is 5 ksi (35 MPa). All the columns of the Riverdale Bridge Bent are 16 ft (4.90 m) high, and 42 in. (1.10 m) octagonal in diameter. Twelve No 6 (19M) longitudinal mild steel bars are equally spaced circumferentially, which are then connected and confined by No. 4 (13M) spiral hoops with a pitch of 6 in. (152 mm) and diameter equal to 38 in. (965 mm). For the protection of rebar against corrosion and other different environmental factors, 1½ in. (38 mm) clear cover is used. Six 1⅜ in. (35 mm) grade 150 ksi (1034 MPa) PT bars compliant to ASTM A-722 were used in both columns for the self-centering of the bridge bent. Galvanized corrugated steel ducts, 2⅛ in. (54 mm) (outer diameter) 36 gauge were placed inside the column to accommodate the PT bars. The reinforcement ratio of the longitudinal mild steel bars is 0.36%, and the PT bar reinforcement ratio is 0.64%. Only four PT bars are projected inside the cap beam directly above the column, as shown in Figure 2.4 and Figure 2.5.

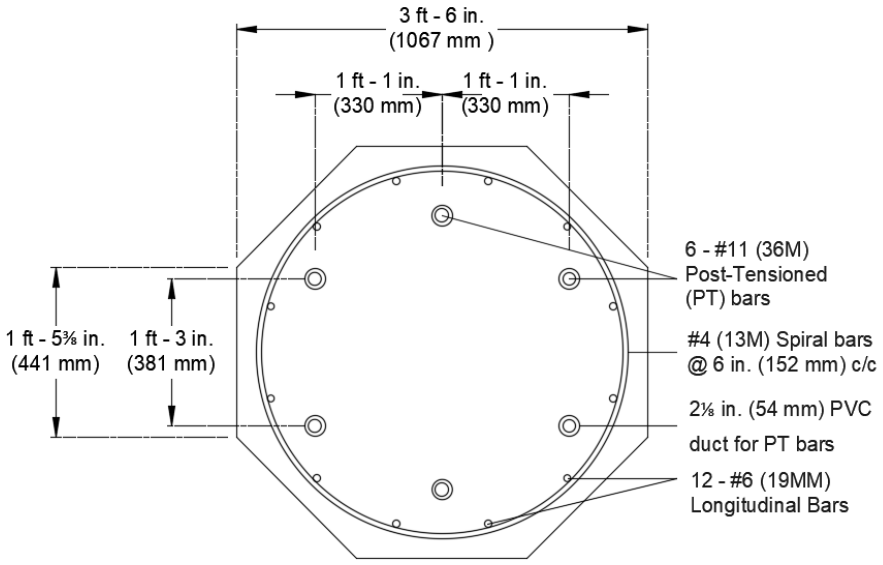

Figure 2.4 Section @ B-B

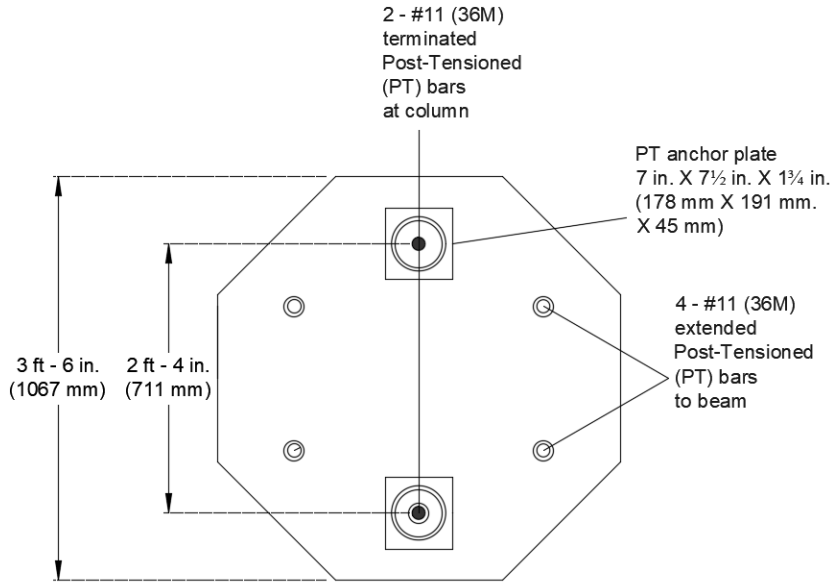

Figure 2.5 Section @ A-A

The center-to-center spacing of the columns for the end bents is 24 ft 6 in. (7.47 m); it is 6 in. (0.152 m) shorter in the case of the two central bents. The original Riverdale Bridge consists of two rectangular beams of different lengths but of the same width, 4 ft (1.219 m), as seen in Figure 2.3. The total length of the cap beam at the end bents is 45 ft 9 in. (13.95 m), while the length of the two central bents is 40 ft (12.2 m). The two central bents have a cantilever of 8 ft (2.40 m) on either side from the center of the column. The end bents have the same cantilever length as the two central bents on the inner side, but the cantilever section at the ends is 13 ft 3 in. (4.04 m) from the center of the extreme column. The gap between two cap beams is 3 ft 6 in. (1.07 m). The height of the cap beam varied throughout the length from 4 ft (1.20 m) on the outer side to 4 ft 4 in. (1.32 m) on the inner side. The width of the cap beam was 4 ft (1.20 m). Typical reinforcement details of the cap beam can be seen in Figure 2.6.

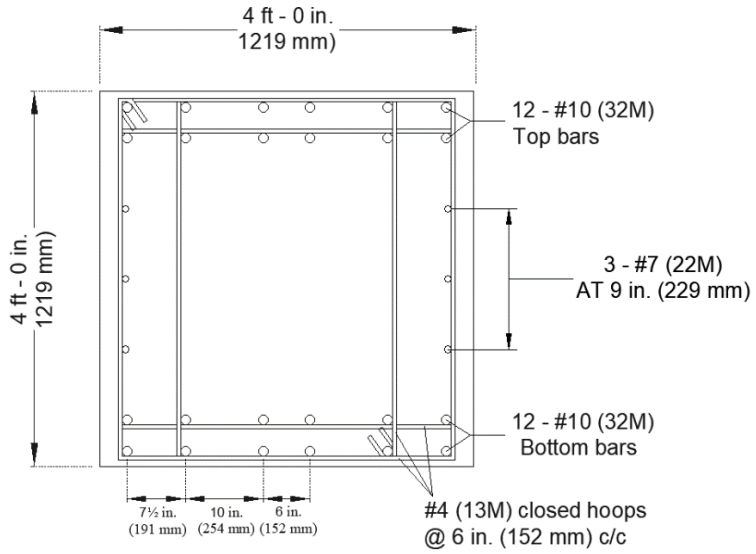

Figure 2.6 Section @ C-C

At the top and bottom of the beam, No. 10 (32M) longitudinal bars with two rows and six bars on each row extend throughout the beam. Three No. 7(22M) longitudinal bars are present on either side of the beam, and the rectangular loop formed by those longitudinal bars is tied with No 4. (13M) closed hoops, as shown in Figure 2.6. Four 1⅜ in. (35 mm) grade 150 ksi (1034 MPa) PT bars from the columns are extended to the beam, while two are terminated at the top of the column at the column-to-cap beam interface. The place where these PT bars are projected into the beam is heavily reinforced with an extra spiral reinforcement cage, as seen in Figure 2.7. A 2 in. (51 mm) layer of non-shrink grout is filled between the beam-column interface.

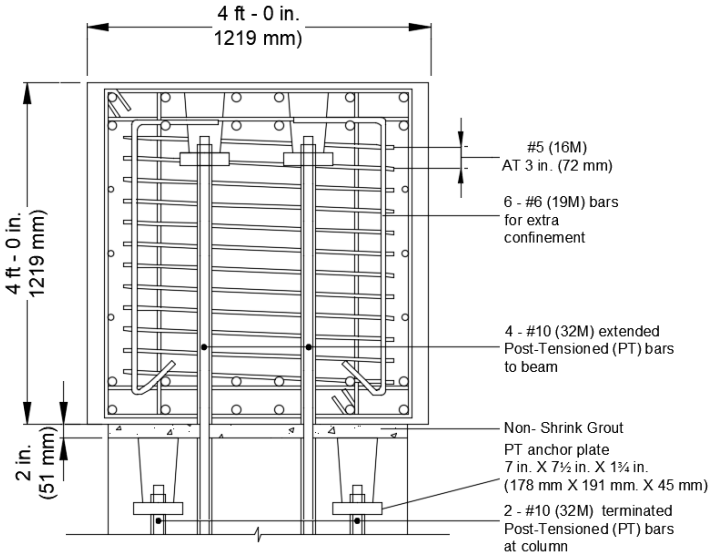

Figure 2.7 Section @ X-X

2.2 Specimen Design

The post-tensioned bridge bent with BRB, termed as PT-BRB bent specimen, was built in the Structures Laboratory of the University of Utah; it is a 42% reduced scale specimen in terms of the size of the Riverdale bridge bent. (Dangol and Pantelides 2022; Dangol et al. 2022) Following the design recommendations of the California Department of Transportation (Caltrans) seismic design criteria (SDC), the bent was designed using the capacity design approach. The BRB as a secondary external earthquake resisting element was incorporated for energy dissipation, and the bent was designed to remain elastic throughout the test (Caltrans 2019). The columns, footings, and cap beam act as capacity protected members in this hybrid bridge system, while the BRB is a sacrificial energy-dissipating element.

For transferring the shear force from the superstructure to the substructure, a shear key was built in the footing as an octagonal shear key in the form of a recess, precisely at the center of the footing, 21 in. (533 mm) in diameter and 1 in. (25 mm) deep. Both the top and bottom longitudinal bars were bent 90° toward the footing depth near the edge of the footing to satisfy anchorage and development length criteria. Below the octagonal recess of the footing, supplementary confinement was provided to improve the compressive capacity of the footing. This was achieved by means of 12 No. 5 (16M) straight vertical bars, equally spaced along the circumferential path, with 135° hooks on the top end and 90° hooks on the bottom end tied with No. 3 (10M) spiral hoops at a 2.5 in. (64 mm) pitch. To accompany the unbonded 1 in. (25 mm) diameter post-tensioned bars, two 2 7/8 in. (73 mm) schedule 80 polyvinyl chloride (PVC) pipes were installed in the middle of the footing, which passed from the bottom to the top. The concrete cover of the footing was approximately 1 in. (25 mm) at top and bottom, while it was 2 in. (51 mm) on the sides. Detailed drawings of the footing specimen are shown in Figure 2.8 to Figure 2.10.

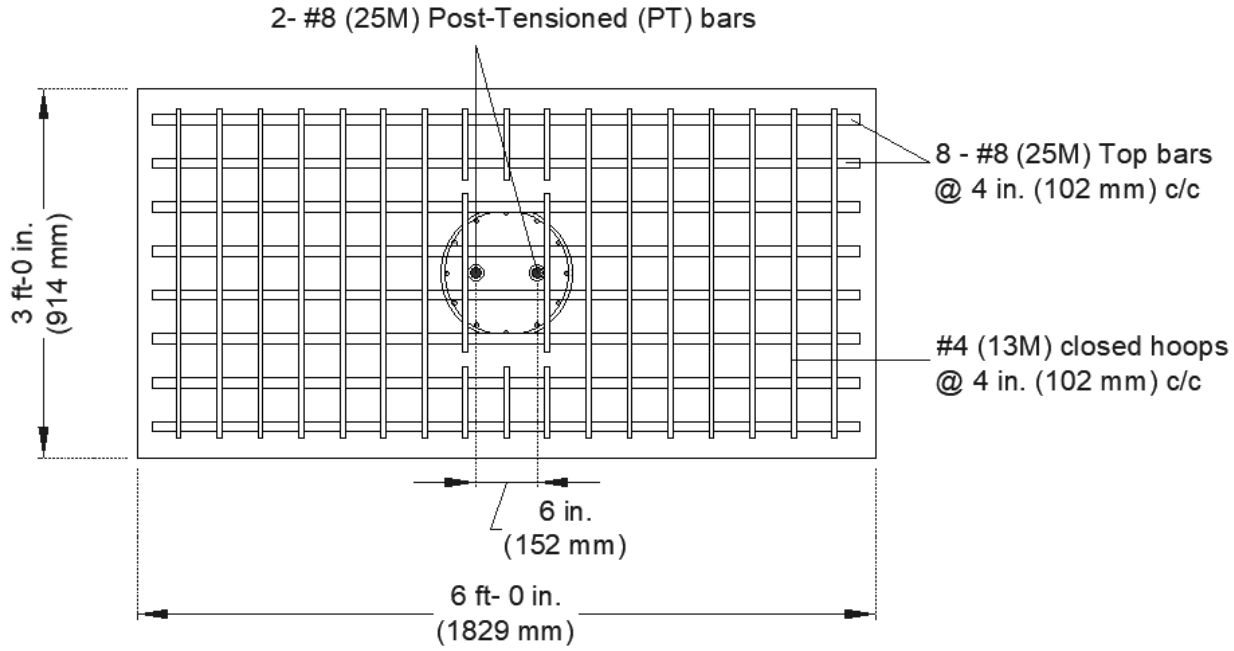

Figure 2.8 Top view of footing reinforcement

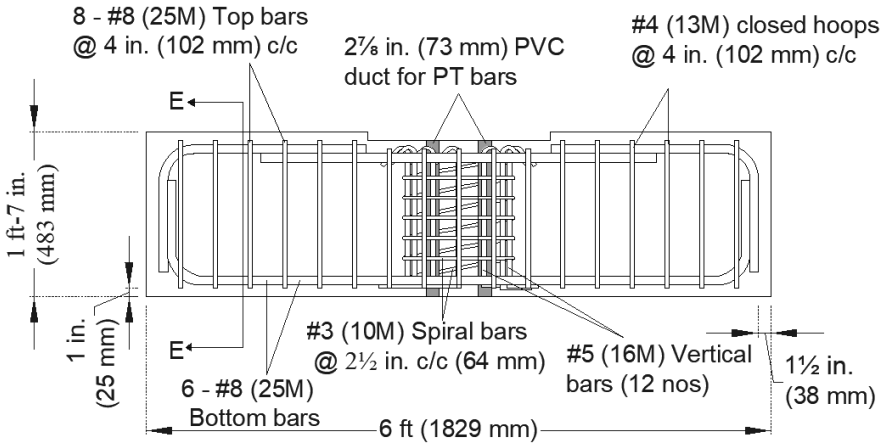

Figure 2.9 Reinforcement details of the footing

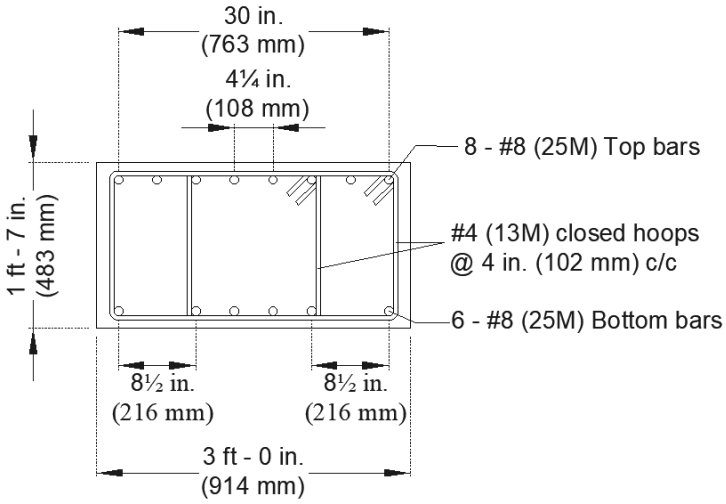

Figure 2.10 Section E-E of the footing

The diameter of the octagonal column was 1 ft. 6 in. (457 mm). The column was 7.0 ft. (2.10 m) long reinforced with 12 No. 5 (16M) longitudinal bars; spiral confining reinforcement was used with a No. 5 (16M) bar and a pitch of 3 in. (76 mm), as seen in Figure 2.11. The tensile yield strength of the mild steel longitudinal rebars was 68,000 psi (469 MPa). The concrete cover was 1.5 in. (38 mm). The reinforcement ratio of the longitudinal bars was 1%. To incorporate the unbonded post-tensioning tendons within the column, two 7 ft (2.124 m) long by 2 7/8 in. (83 mm) (outer diameter) 80 PVC pipes with a thickness of 1/5 in. (5 mm) were placed inside each column, as seen in Figure 2.12. The reason for using PVC is not only because of its high-pressure rating, but also to distribute the strains in the PT bars evenly throughout their length. Two No. 8 (25M) 150 ksi (1034 MPa) all threaded PT bars were used for post-tensioning each column. The distance between the PT bars was 6 in. (152 mm) with each being 3 in. (76 mm) from the centerline of the column. The PT bar reinforcement ratio is 0.59%. The 28-day compressive strength of concrete for the columns was 10,000 psi (69 MPa). On the day of testing, the concrete compressive strength of the columns was 14,000 psi (86 MPa).

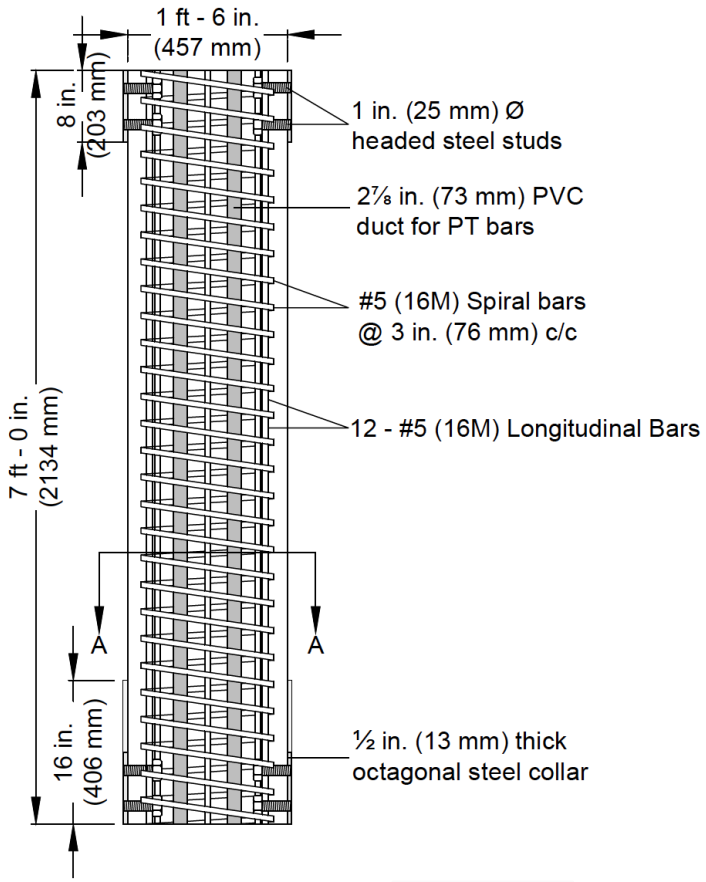

Figure 2.11 Reinforcement detail of column

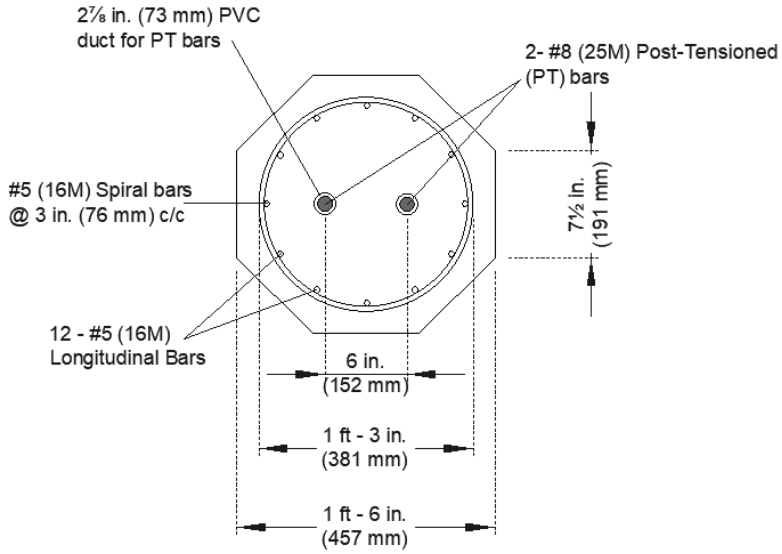

Figure 2.12 Section A-A of the column

Two-headed steel studs in each face of the octagonal column, 3 in. (76 mm) apart, were used to support the steel collar placed near the ends of the columns. The 3½ in. (90 mm) long studs had a shank diameter of 1 in. (25 mm), while the ½ in. (13 mm) thick head had a diameter of 2 in. (51 mm). With the head being inside the spirals, the headed studs were embedded 3 in. (77 mm) inside the concrete, and the remaining length of ½ in. (13 mm) protruded outside the concrete face to which a ½ in. (13 mm) steel collar was welded. Altogether 16 studs are placed at either end of the column for facilitating the ½ in. (13 mm) thick steel collar to be welded upon protruded ½ in. (13 mm) shank. The octagonal steel collar was 16 in. (406 mm) high at the bottom end, whereas it was only 8 in. (203 mm) at the top end.

The cap beam was designed to be placed on top of the two octagonal columns spaced at 10 ft (3.048 m) from the center to center. The dimensions of the cap beam used for the experiment were 14 ft 3½ in. (89 mm) long, 22 in. (559 mm) wide, and 19 in. (483 mm) high. Thirty-six No. 5 (16M) continuous longitudinal bars span across the length of the cap beam, as shown in Figure 2.13. Figure 2.14 shows the cross-section of the cap beam. The arrangement of the longitudinal bars had two rectangular groups of the same shape but of different sizes, namely an inner and outer group. The outer group, which had 22 longitudinal bars, was tied with No. 3 (10M) rectangular stirrups. The center-to-center spacing of the stirrups was 6 in. (152 mm). Single-legged No. 3 (10M) shear stirrups were used to tie the 14 bars of the inner group, which connected the inner longitudinal bars with the outer ones; these bars were spaced at 6 in. (152 mm). All the inner and outer longitudinal bars were cross-tied to each other. The single-legged stirrups had 90° hooks on one end and 135° hooks on the other end. To fulfill the seismic hook requirement of ACI 318-14, a standard hook extension of 3 in. (76 mm) was employed. The reinforcement ratio of the cap beam was 2.5%. The purpose of using such a high reinforcement ratio was to make sure that the cap beam remains elastic. A clear cover of 1½ in. (38 mm) was used. In order to satisfy the anchorage and development length criteria, the bars were bent at the corners, similar to the footing. Extra confinement was provided at two different locations, where the precast column aligns directly underneath the cap beam. This additional supplementary confinement was accomplished by providing 12 No. 5 (16M) vertical bent bars (135° hooks at one end and 90° hooks at the other end) confined with No. 3 (10M) spirals at a pitch of 2½ in. (64 mm). A pair of 2⅞ in. (83 mm) schedule non-threaded 80 PVC 19 in. (482 mm) long pipes were embedded in the cap beam to facilitate placement of the unbonded post-tensioned bars from the columns.

All-threaded bars with ultimate tensile strength of 150 ksi (1034 MPa) were used as PT tendons with 1 in. (26 mm) diameter. The length of PT tendons was 10 ft 10½ in. (3.315 m) and stretches from the top of the cap beam to the bottom of the footing. The minimum net area through the threads is 0.85 $in.^2$ (549 mm^2). The minimum ultimate strength of the bars is 128 kip (567 kN). The all-threaded bars perform elastically up to 80% of their ultimate tensile strength and thus are particularly useful for self-centering systems. These bars are manufactured in strict accordance with ASTM A722 and AASHTO M275 highway specifications. The strength of the prestressing steel bars is not only high-level but also ductile enough to exceed the necessary elongation and reduction of area conditions. PT rod, 1 in. (25 mm) 150 ksi (1034 MPa) all threaded bar was used for fixing the gusset plate assembly at the column-footing interface and gusset assembly at the cap beam to attach the BRB. Six 25 in. (635 mm) long PT rods were used to fasten the ¾ in. (19 mm) base plate of the lower gusset assembly to the footing, and another six PT rods of 28 in. (711 mm) in length were used to fix the faceplates of the upper gusset assembly to the cap beam.

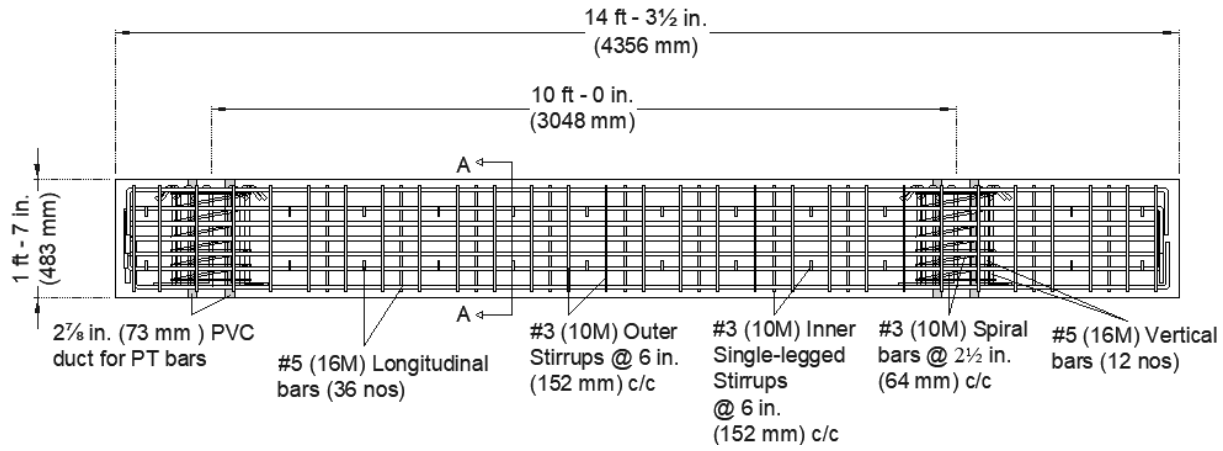

Figure 2.13 Reinforcement detail of beam

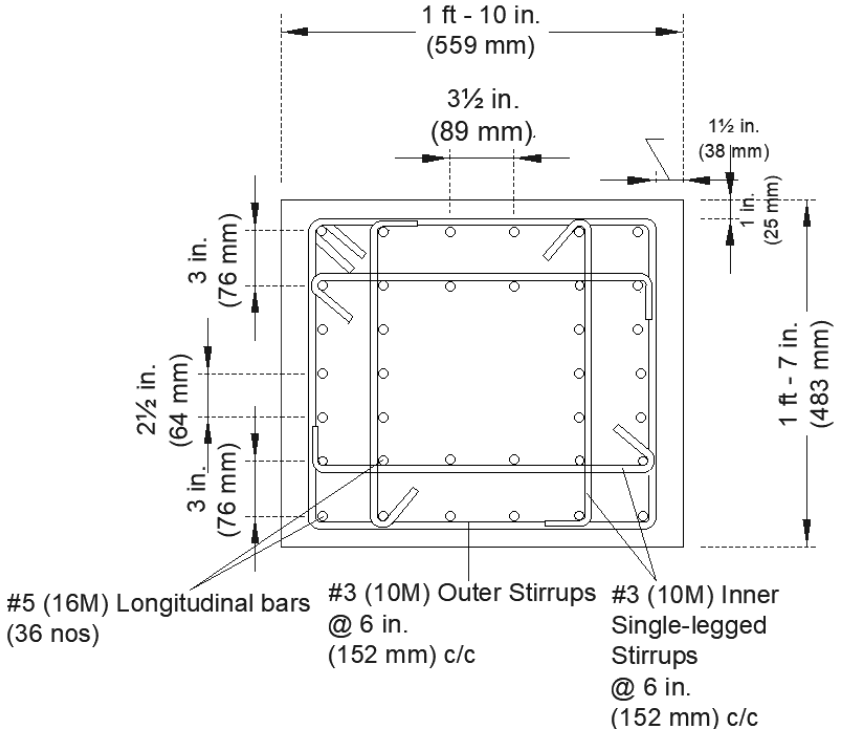

Figure 2.14 Section at A-A of beam

2.3 BRB and its Mechanism in Frame

Figure 2.15 shows the arrangement of the diagonal BRB in the self-centering bridge bent. Initially, the dotted line in the diagram represents the typical BRBF with two columns, one rigid cap beam, and a BRB as the diagonal member. The BRB is inclined at an angle γ with respect to the horizontal.

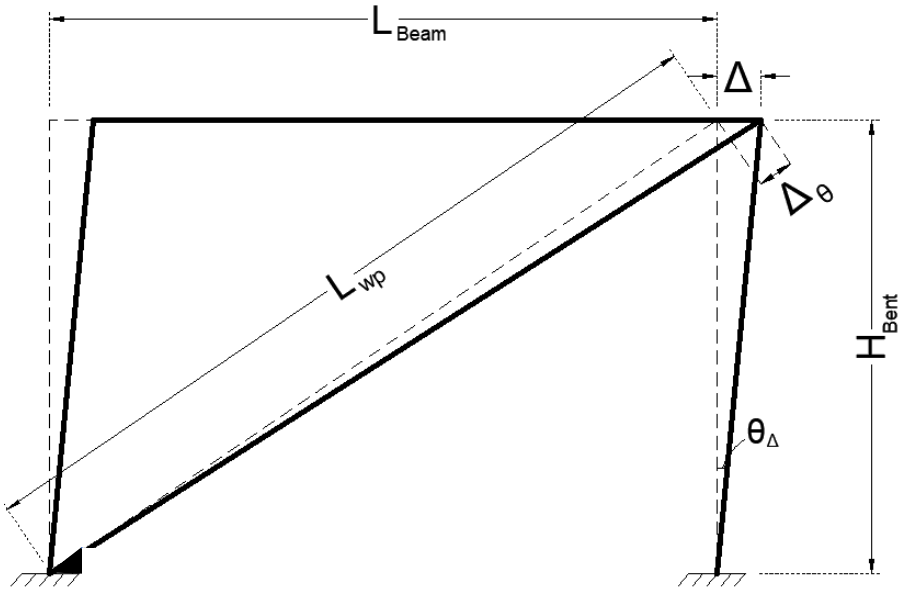

Figure 2.15 Mechanism of BRB in a frame

With the increase in lateral displacement of the bridge bent, Δ, as shown by the solid line, the BRBF kinematic behavior with the rigid beam shown in Figure 2.15 illustrates that, under the assumption of small changes of angles, the BRB axial deformation is given by,

$$\Delta_\theta = \Delta.\cos(\gamma) \tag{2.1}$$

This equation can be simplified in terms of the brace work-point length, L_{wp}, and the design story drift angle due to the drift, θ_Δ, as:

$$\theta_\Delta = \frac{\Delta}{H_{Bent}} \tag{2.2}$$

where H_{Bent} is the height of the bent. Thus:

$$\Delta_\theta = \theta_\Delta.H_{Bent}.\cos(\gamma) \tag{2.3a}$$
$$\Delta_\theta = \theta_\Delta.L_{wp}.\sin(\gamma).\cos(\gamma) \tag{2.3b}$$
$$\Delta_\theta = \frac{1}{2}.\theta_\Delta.L_{wp}.\sin(2\gamma) \tag{2.3c}$$

Then, if we define the yield length ratio (YLR) as:

$$YLR = \frac{L_y}{L_{wp}} \tag{2.4}$$

where L_y is the length of the yielding region of the BRB steel core with steel core area (A_{sc}). Assuming rigid beam and the elastic deformation in the non-yielding section of the BRB steel core is small, the strain in the BRB core, ε_{sc}, is calculated as:

$$\Delta_\theta = \frac{1}{2}.\theta_\Delta.\frac{L_y}{YLR}.\sin(2\gamma) \tag{2.5a}$$

$$\frac{\Delta_\theta}{L_y} = \frac{\theta_\Delta \sin(2\gamma)}{2\,YLR} \tag{2.5b}$$

$$\varepsilon_{sc} = \frac{\theta_\Delta \sin(2\gamma)}{2\,YLR} \tag{2.5c}$$

The core strain demand can be easily evaluated with the above equation. When the drift is increased, there will be an increase of core strain demand. The BRB core strain is inversely proportional to the *YLR*; this means that large core strains will develop at relatively modest drifts for small yield length ratios, which should be avoided.

2.4 Design of Initial Post-tensioning Forces for Hybrid PT-BRB Bent

Two PT bars were used in each column; 1.00 in. (25 mm) diameter unbonded all-threaded bars were used with a tensile strength of 150 ksi (1034 MPa) and minimum net area of 0.85 in.^{2} (548 mm^2). The PT bars were manufactured per ASTM A722 (ASTM 2015); the yield strength of the PT bars was 102 kip (454 kN) with an ultimate strength of 128 kip (569 kN).

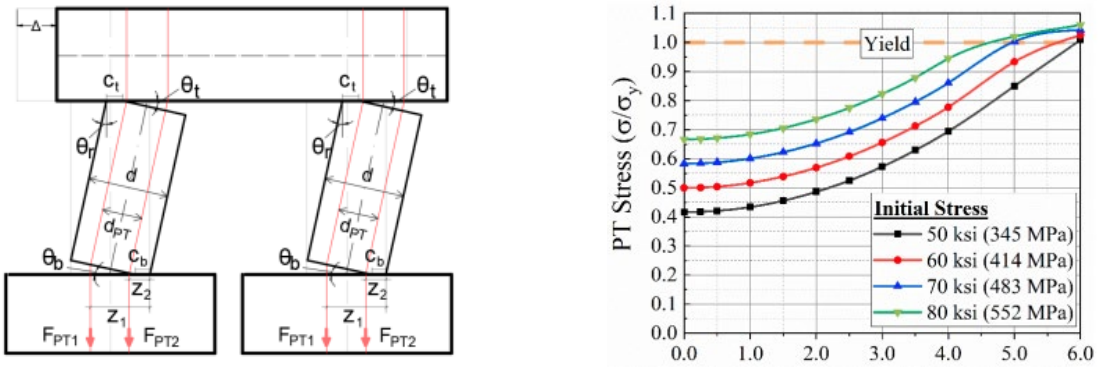

(a) (b)

Figure 2.16 Post-tensioned bridge bent (PT-Bent): (a) schematic layout of PT-Bent during push cycle; (b) variation of PT stress for various levels of initial post-tensioning

The maximum value of initial post-tensioning force should not exceed 50% of the ultimate tensile strength of the PT bar (FHWA 2013). The initial value of post-tensioning force was determined using a rigid body analogy for the columns of the bridge bent without the BRB; frictional forces at the joints were ignored. The post-tensioned bridge bent without the BRB was the basis for design and was termed the PT-Bent. Even though this method overestimates the PT bar forces, it is acceptable for initial design. Column rotation is calculated from the horizontal displacement and height of the bent; this rotation causes uplift of the column toe as shown in Figure 2.16(a). The column-to-cap beam and column-to-footing joints are connected through PT bars. Joint rotation increases PT bar strain; four initial stresses were used to find the post-tensioning force for drift ratios up to 6.0%, as shown in Figure 2.16(b). The initial post-tensioning stress was selected as 60 ksi (414 MPa), or 50% of the PT bar yield strength, for a post-

tensioning force of 51 kip (227 kN) in each bar, which postpones yielding until a 5.0% drift ratio (Figure 2.16b).

The initial post-tensioning force in the PT bars should be such that yielding of PT bars or total loss of post-tensioning is avoided at the target rotation, θ_T. The decompression region occurs at the top and bottom of the column due to rotation on the top (θ_t) and bottom ends of the column (θ_b) caused by the lateral displacement Δ in Figure 2.16(a). The forces in each PT bar are a function of the rotation at the top and bottom of the column and are obtained as follows (Freddi et al. 2017; 2020):

$$F_{PT} = T_{PT} + K_{PT}(Z_1 - c_b)\theta_b + K_{PT}(Z_2 - c_t)\theta_t \quad (2.6a)$$

$$\theta_b \leq \theta_{PT,y};\ \theta_t \leq \theta_{PT,y} \quad (2.6b)$$

where, F_{PT} is the force in the PT bars at a lateral displacement Δ; T_{PT} is the initial post-tensioning force in the PT bars; $K_{PT} = A_{PT}E_{PT}/L_{PT}$ is the stiffness of the PT bars; E_{PT}, A_{PT}, and L_{PT} are, respectively, the elastic modulus, cross-sectional area, and length of the PT bars; $\theta_{PT,y}$ is the rotation at which the PT bars yield; $(Z_1 - c_b)$ and $(Z_2 - c_t)$ are the lever arms of the PT bar forces within a column with respect to the center of rotation; Z_1 and Z_2 are the distances from the edge of the column toe to each of the two PT bars; and c_b and c_t are the neutral axis depths at the column bottom and top, respectively, as shown in Figure 2.16(a). Assuming the same rotation at the top and bottom for simplicity, $\theta_b = \theta_t = \theta_r$:

$$F_{PT} = T_{PT} + K_{PT}\theta_r(d - c_b - c_t) \quad (2.7)$$

To determine whether the selected value of initial post-tensioning stress in the PT bars is satisfied in the PT-Bent, the chosen value of initial post-tensioning stress should be such that the PT bars do not yield at the design target rotation (θ_T), which leads to the following inequality from Eq. (2.7):

$$L_{PT} \geq \frac{E_{PT}A_{PT}\theta_T(d - c_b - c_t)}{F_{PT\_Y} - T_{PT}} \quad (2.8)$$

The values of E_{PT} and A_{PT} are assumed as 27,000 ksi (186 GPa) and 0.85 in.^{2} (548 mm^2), respectively; the design target rotation, θ_T, is assumed as 0.02 rad; $Z_{PT,u}$ and $Z_{PT,d}$ are calculated and the diameter of the column is 18 in. (457 mm). The values of T_{PT} and $F_{PT,y}$ are 51 kip (227 kN) and 102 kip (454 kN), respectively. From numerical analysis, the value of c_b and c_t can be conservatively assumed as 4.5 in. (114 mm). The length of the PT bars used in the experiment was 124 in. (3,150 mm), which is greater than 80 in. (2,032 mm) obtained from Eq. (2.8). Loss of stress from initial post-tensioning stress at the target rotation will not occur since the gap opening at the column top and bottom will increase the strain in the PT bars with increasing drift ratio.

2.5 Design of BRB for Hybrid PT-BRB Bent

The hybrid PT-BRB Bent in Figure 2.17 consists of the PT-Bent and a diagonal BRB placed at an angle (γ) with the horizontal. The BRB prevents damage to structural elements by acting as a primary energy dissipation device or fuse. The BRB steel core is the yielding element in tension and compression, which experiences significant inelastic deformations during a design-level earthquake while all other structural elements are capacity-designed and remain elastic (AISC 341, 2016). Figure 2.18 shows the proposed hybrid bridge bent concept, which is that the post-tensioning forces and gravity load re-center the bridge bent and that the BRB dissipates hysteretic energy. The initial stiffness of the hybrid bridge bent is provided by both the BRB and post-tensioned columns. A BRB with low yield force allows yielding of

the PT bars, which is undesirable and may not provide sufficient re-centering; a BRB with a large yield force would yield at high drift ratios and hysteretic energy dissipation might be inadequate. For the PT-BRB Bent, four criteria are used for selection of an appropriate BRB.

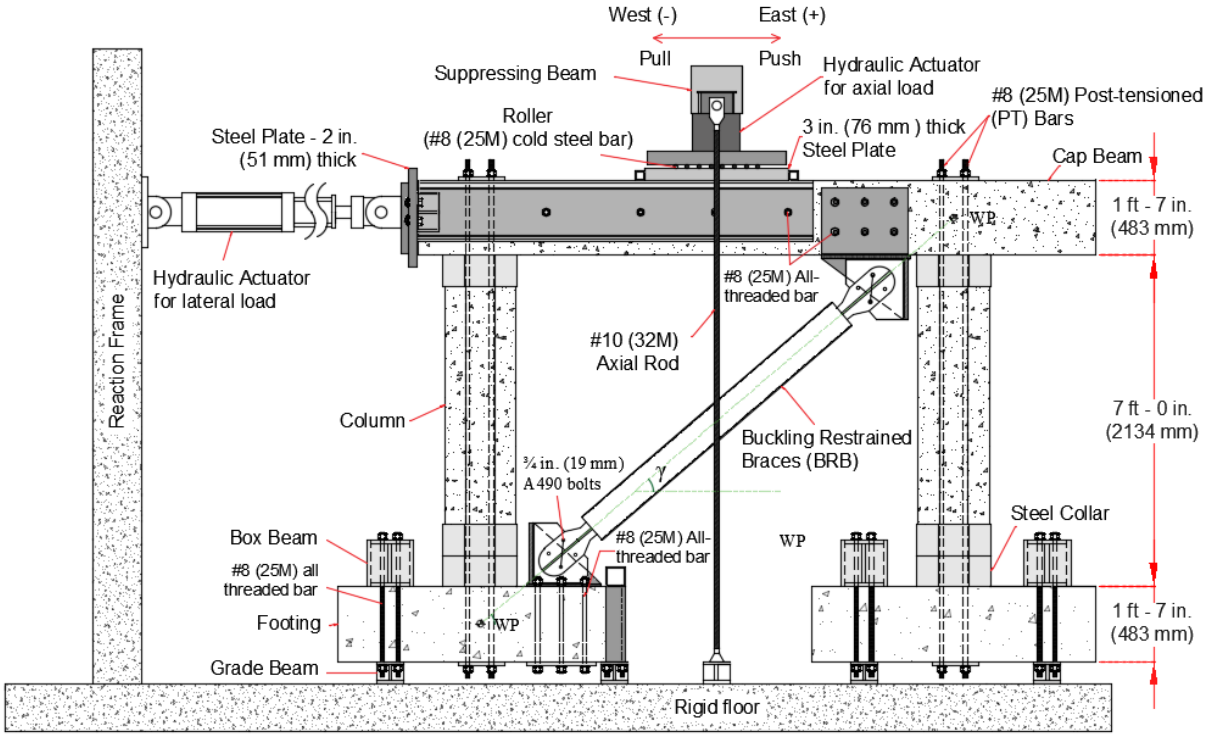

Figure 2.17 Schematic layout of PT-BRB Bent test

The first criterion is the yield displacement of the BRB relative to the yield displacement of the PT-Bent. As shown in Figure 2.18(b), Δ_{PT_Y} and Δ_{BRB_Y} are the yield displacements of the PT-Bent, and the BRB, respectively; $\Delta_{PT\_BRB\_Y}$ is the yield displacement of the PT-BRB Bent, which is equal to Δ_{BRB_Y}, and Δ_D is the difference between the yield displacement of the PT-Bent and the BRB. For efficient functioning of the hybrid bent, the columns should not yield before the BRB; the BRB yield displacement is selected to be less than 50% of the yield displacement of the PT-Bent [Eq. (2.9)]:

$$\Delta_{BRB\_Y} \leq \frac{\Delta_{PT\_Y}}{2} \tag{2.9}$$

In the hybrid PT-BRB Bent, the total lateral force is resisted by the combination of the PT-Bent and BRB. To be considered a dual structural system, the bridge bent should be designed in such a way that, at yield, it can resist at least 25% of the total design lateral force (ASCE/SEI 7–16 2017). If α is defined as the ratio of the BBR yield force (F_{BRB_Y}) to the yield force of the PT-Bent (F_{PT_Y}), as shown in Figure 2.18(b), then α should be less than 3.0 so that the system can be considered as a dual system (Freddi et al. 2021):

$$\frac{F_{PT\_Y}}{F_{BRB\_Y} + F_{PT\_Y}} \geq \frac{1}{\alpha + 1} \tag{2.10}$$

The relationship between the stiffness of the two systems, i.e., stiffness of the BRB (K_{BRB}) and stiffness of the PT-Bent (K_{PT}), can be derived as:

$$K_{BRB} \leq K_{PT}\left(\frac{3\Delta_{PT\_Y}}{\Delta_{BRB\_Y}}\right) \tag{2.11}$$

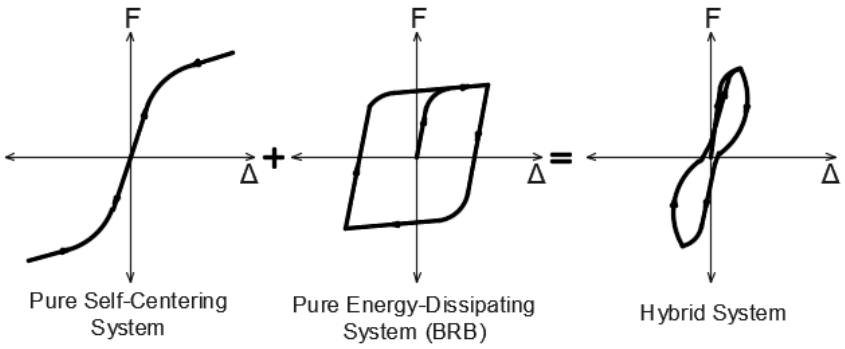

(a)

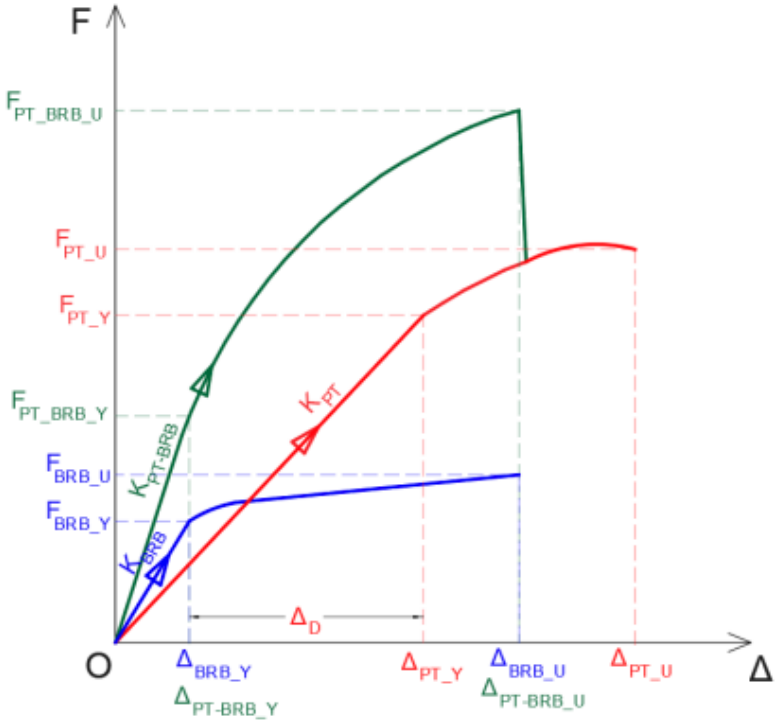

(b)

Figure 2.18 PT-BRB Bent hybrid concepts: (a) hybrid system; (b) force-displacement behavior

The stiffness of the BRB from principles of mechanics is equal to:

$$K_{BRB=}\frac{A_{BRB}E_{BRB}}{L_{BRB}}(cos\gamma)^2 \tag{2.12}$$

where, A_{BRB} is the core area of the BRB, E_{BRB} is the modulus of elasticity of the steel core, L_{BRB} is the length of the yielding steel core of the BRB, and γ is the angle of the BRB with the horizontal. Since angle γ and the modulus of elasticity of steel cannot be changed, the desired BRB is obtained either by changing the steel core yielding length or the steel core area; the resulting BRB stiffness from Eq. (2.12) satisfies the condition specified in Eq. (2.11).

The second criterion is the relationship between the lateral force at yield of the PT-BRB Bent and the PT-Bent, as shown in Figure 2.18(b). The lateral force at yield displacement of the PT-BRB Bent ($F_{PT\_BRB\_Y}$) should be less than the lateral force at yield displacement of the PT-Bent (F_{PT_Y}), as shown in Eq. (2.13a); this is so that the majority of hysteretic energy is dissipated by the BRB and not the bridge bent. Simplification of Eq. (2.13a) using Figure 2.18(b) results in Eq. (2.13b):

$$F_{PT\_BRB\_Y} \leq F_{PT\_Y} \tag{2.13a}$$

$$F_{BRB\_Y} \leq K_{PT}\Delta_D \tag{2.13b}$$

Using Eq. (2.13b), the initial stiffness of the PT-Bent (K_{PT}) from the pushover curve helps determine an appropriate BRB strength; the maximum BRB strength can thus be obtained.

The third criterion is that in order to promote re-centering, yielding of the PT bars should be avoided. According to AISC 341 (2016), the BRB strain (ε_{brb}) can be expressed in terms of the drift angle (θ_r), the brace angle with respect to the horizontal direction (γ), and the yield length ratio (YLR), defined as the ratio of the steel core yielding length to the work point length (distance between two work points, WP, as shown in Figure 2.17), as obtained from Eq. (2.5c) as:

$$\varepsilon_{BRB} = \frac{\theta_r \sin(2\gamma)}{2YLR} \tag{2.14}$$

Assuming that the ultimate strain in the BRB steel core is ε_{BRB_U}, then the drift angle at which the BRB fractures ($\theta_{r\_BRB\_U}$) is given as:

$$\theta_{r\_BRB\_U} = \frac{2YLR\ \varepsilon_{BRB\_U}}{\sin(2\gamma)} \tag{2.15}$$

Using 4.0% as the ultimate strain of the BRB steel core, *YLR* as 0.3, and γ as 41°, $\theta_{r\_BRB\_U}$ was found as 0.024 rad. From Eq. (2.6a), the post-tensioning force at BRB fracture is obtained as 90 kip (400 kN), which is less than 102 kip (454 kN), the yield force of the PT bar; the PT rods should not yield until the BRB steel core fractures.

The fourth criterion concerns the lateral strength of the PT-BRB Bent ($F_{PT\_BRB\_U}$), shown in Figure 2.18(b), which should not exceed 1.5 times the lateral strength of the PT-Bent (F_{PT_U}) to reduce the demand on other members of the bridge system:

$$F_{PT\_BRB\_U} \leq 1.5F_{PT\_U} \tag{2.16}$$

2.6 BRB Parametric Design

Frames that incorporate BRBs are known as BRB frames (BRBFs), and they have comparatively more advantages than other braced frames. The main aim of the BRB used in a resilient frame is to limit the maximum damage in the structural elements by absorbing the damage itself; it acts as a primary energy dissipation device and restricts damage in the joints. Here, BRBFs are proportioned using the fundamental philosophy for all ductile seismic design. The BRBs are the yielding elements, which are sized for a reduced seismic force level and are likely to experience significant inelastic deformation during a design-level earthquake, while all other elements in the system are capacity-designed so they remain essentially elastic at the expected strength of the BRBs. The American Institute of Steel Construction (AISC 341) states that BRBFs shall be designed so that inelastic deformations under the design earthquake will occur primarily as brace yielding in tension and compression. For the BRB, the adjusted strength in tension (T) and compression (C) of a BRB is given as:

$$T = \omega R_y F_{BRB\_Y} \tag{2.17a}$$

$$C = \omega \beta R_y F_{BRB\_Y} \tag{2.17b}$$

Here, ω is the strain hardening adjustment factor (ratio of the maximum tension force to the measured tensile yield strength), β is the compression strength adjustment factor (the ratio of the maximum compression force to the maximum tension force), F_{BRB_Y} is the axial yield strength of the steel core; and R_y is the ratio of expected yield stress to specified yield stress, equal to 1.0 since coupon tests were used to determine the yield stress. The compression strength adjustment factor (β) is determined from:

$$\beta = \frac{P_{max}}{T_{max}} \tag{2.18}$$

which is the ratio of maximum measured compressive force (P_{max}) to maximum measured tensile force (T_{max}) per loading cycle; to reduce the demand on brace connections and adjoining members, this ratio must remain below 1.5 per AISC 341 (2016). Similarly, the strain hardening adjustment factor (ω) is:

$$\omega = \frac{T_{max}}{R_y P_{ysc}} \tag{2.19}$$

which is the ratio of maximum measured tensile force to the yield force per cycle. The resulting value of ω should be greater than 1.0 according to AISC 341 (2016). Brace connections and adjoining precast members are designed to resist forces obtained from the adjusted BRB strength in compression and tension. In tests of BRBs similar to the one used in this experiment, factor β_{max} ranged from 1.02 to 1.22 and ω_{max} from 1.81 to 1.98.

Parametric numerical studies were carried out to determine the contribution of the BRB to the base shear capacity of the hybrid PT-BRB Bent. From Figure 2.19, a preliminary pushover analysis using OpenSees (Mazzoni et al. 2005) shows that for an initial post-tensioning force equal to 50% of the PT bar yield capacity, a BRB with 40 kip (178 kN) yield force satisfies the four criteria. In this case, the BRB contributes 30.1 kip (134 kN) to the lateral force at yield of the BRB. From Figure 2.22, the estimated yield strength of the PT-Bent is 60 kip (267 kN); thus, the PT-Bent alone is estimated to contribute 66% of the total design lateral force. The resulting bridge bent acts as a dual frame since the PT-Bent alone contributes more than 25% of the total design lateral force. Hence, a BRB with a steel core area of 0.9 in.^{2} (581 mm^2) was chosen, with actual yield strength of 44.6 ksi (308 Mpa). One BRB, 116 in. (2.95 m) long

with a steel core length of 46 in. (1.16 m) was placed diagonally at an angle (γ) of 41° to the horizontal, connecting the cap beam to the footing using steel gussets, as shown in Figure 2.17.

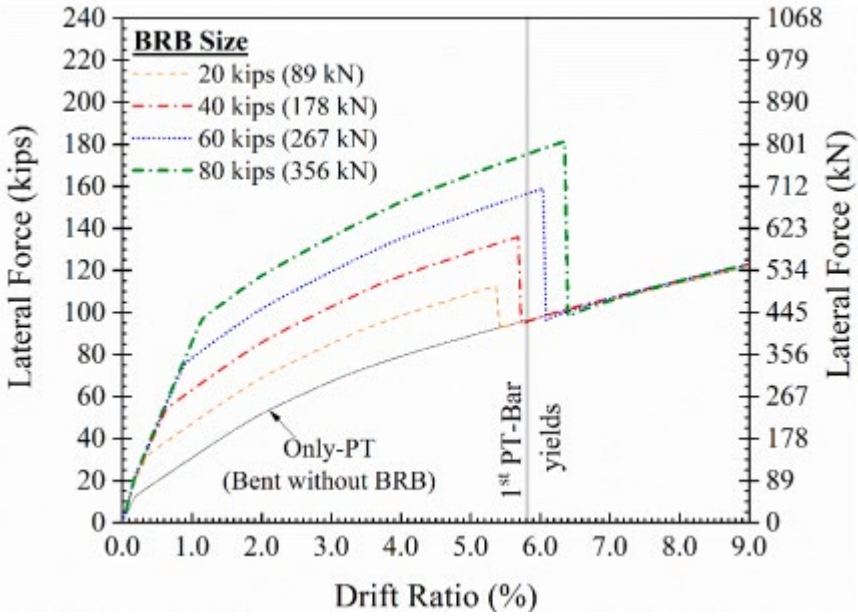

Figure 2.19 Pushover curve of PT-BRB Bent with different BRB capacities for initial post-tensioning force equal to 50% of PT bar yield force

2.7 Design of Hybrid PT-BRB Bent for Re-centering

After the selection of the initial post-tensioning forces and the BRB size and yield force, the hybrid system was checked to verify that the given combination would achieve re-centering. A re-centering condition can be accomplished by ensuring that the re-centering bending moment is able to overcome the bending moment from the non-prestressed reinforcement to close the gap at the column joints (Pampanin et al. 2010). To achieve this goal, the ratio of bending moment from the energy dissipator (M_s) to the total bending moment of the system (M_{tot}) should satisfy:

$$\frac{M_s}{M_{tot}} \leq 0.5 \tag{2.20}$$

Accounting for the expected material overstrength factor (α_0) associated with the BRB as the energy dissipation device, the moment contribution ratio (λ) defined as the ratio of self-centering moment contribution (Pampanin et al. 2010), provided by the unbonded bars (M_{pt}) and gravity load (M_N) to $\alpha_0 M_s$, should satisfy:

$$\lambda = \frac{M_{pt} + M_N}{\alpha_0 M_s} \geq 1.0 \tag{2.21}$$

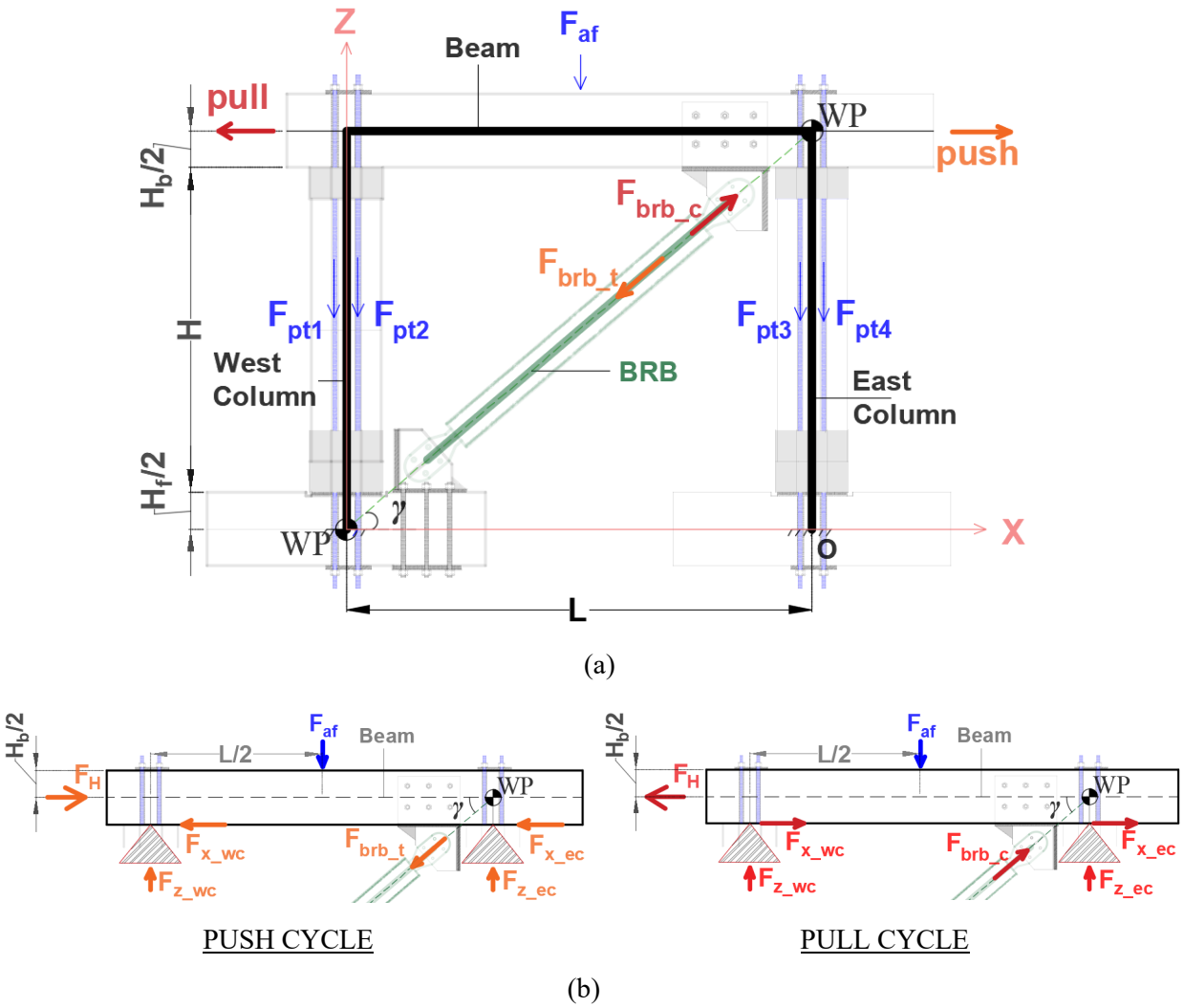

Figure 2.20 PT-BRB Bent analysis: (a) system dissipative and self-centering forces; (b) forces at the cap beam

Figure 2.20 shows the BRB, the post-tensioned columns and cap beam, and the forces involved in the bridge bent. The center-to-center distance between the two columns (L) is 120 in. (3,048 mm); the height of the column (H) is 84 in. (2,134 mm), and the height of the cap beam (H_b) and footing (H_f) is 19 in. (483 mm). A diagonal BRB connects the cap beam with the west footing. The dark line shows the arrangement of the system joining the work point (WP) of the BRB to the footing and cap beam. The initial post-tensioning force (F_{pt}) in each PT bar was taken as 50 kip (222 kN). Using the brace adjustment values in tension and compression, the adjusted BRB strength was estimated as 79 kip (351 kN) in tension, and 97 kip (431 kN) in compression. The total axial force (F_{af}) was taken as 140 kip (623 kN), which was applied at the midspan of the cap beam. The maximum value of the ratio in Eq. (2.20) was found as 0.27, which is less than the recommended 0.50. The maximum value of ratio λ in Eq. (2.21) was 2.7, which is greater than 1.0; thus, re-centering was expected to occur.

2.8 Design of BRB Connections and Clear Gap of Gusset Plate

The purpose of a BRB is to dissipate hysteretic energy and act as a fuse. The connections of the BRB to the bridge bent should be designed so they do not fail before the BRB fractures. The connections of the BRB to the cap beam and footing were designed using grade A572-50 steel gusset plates. A ¾ in. (19 mm) thick gusset plate was used to connect the BRB to the footing, as shown in Figure 2.21(a). The lower gusset assembly consisted of a 1.0 in. (25 mm) vertical steel plate and two ½ in. (13 mm) triangular stiffener steel plates, on either side of the gusset plate, welded to a ¾ in. (19 mm) steel base plate, as shown in Figure 2.21(a) and 2.21(b). The center-to-center distance between the gusset plate and triangular stiffener steel plates was 8 in. (203 mm). The stiffener plates were designed to prevent twisting or buckling of the gusset plate and the BRB.

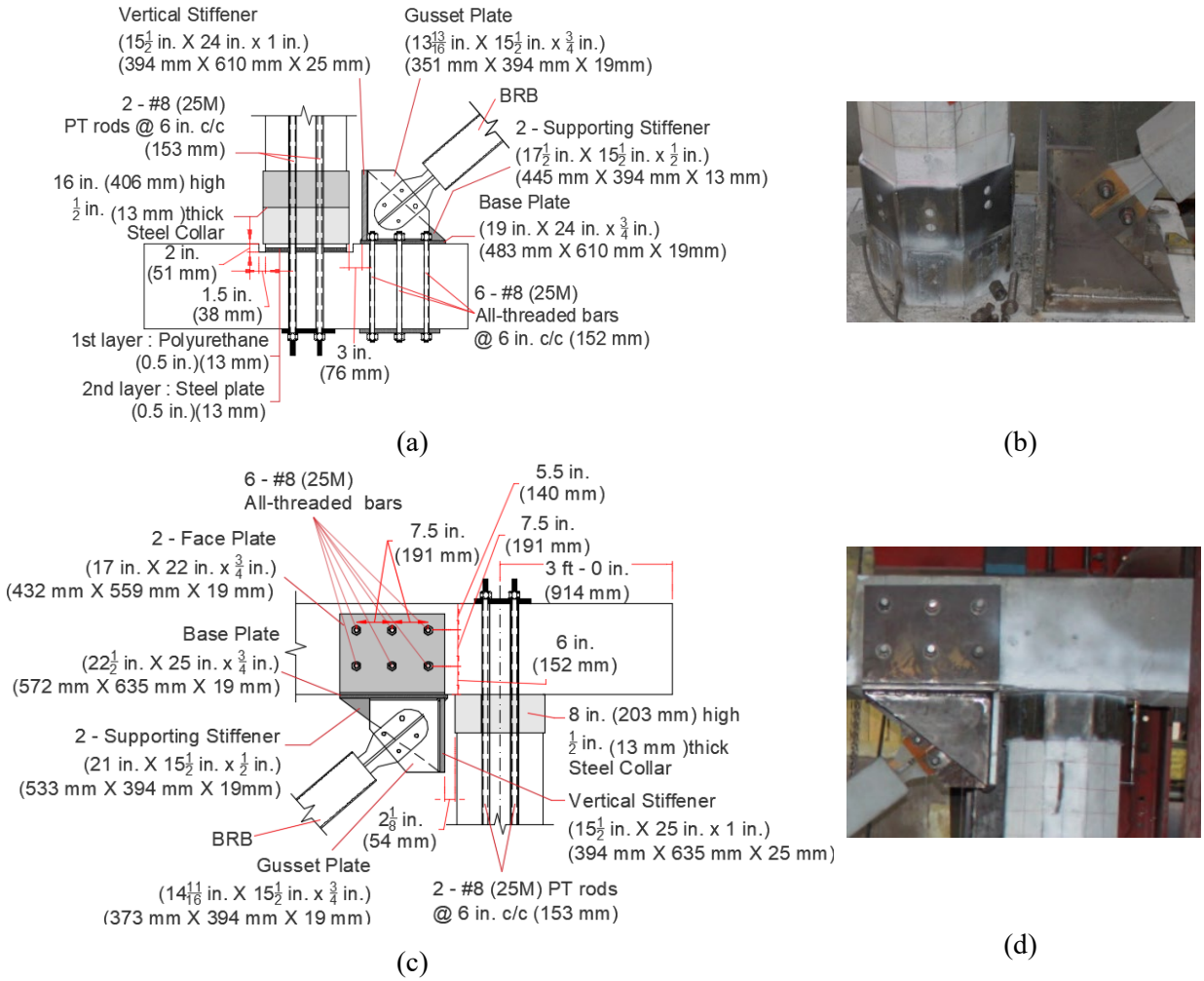

Figure 2.21 Gusset assemblies: (a) lower gusset assembly details; (b) gap between lower gusset and column; (c) upper gusset assembly details; (d) gap between upper gusset assembly and column

The vertical steel plate was designed to support the gusset plate, transfer the BRB forces in the vertical direction, and prevent contact with the rocking column. For fastening the lower gusset assembly to the footing, six 1.0 in. (25 mm) all threaded bars with the same properties as the PT bars were used. Six 1¼ in. (32 mm) diameter through-holes were drilled in the footing for connecting the base plate; six 25 in. (635 mm) long all-threaded bars were used to fasten the base plate to the footing. The design was checked against local and global failure of the concrete in the footing and the threaded bars according to ACI 318 (2019).

Two ½ in. (13 mm) triangular stiffener steel plates, 8 in. (203 mm) from the center of the ¾ in. (19 mm) thick gusset plate, were welded to the base plate of the upper-gusset assembly. The base plate was then welded to ¾ in. (19 mm) thick face-plates to form a U-shaped section around the cap beam, as shown in Figure 2.21(c); the distance between the face plates was 23 in. (584 mm). Six 1¼ in. (32 mm) holes were drilled through the cap beam to facilitate the connection with the upper-gusset assembly, and six identical holes were drilled in each of the steel face-plates. Six 1.0 in. (25 mm) all-threaded bars, 28 in. (711 mm) long, were used to attach the face-plates to the cap beam, as shown in Figure 2.21(d).

The distance between the vertical steel plates of the bottom and top gusset assemblies and the face of the column is designed so that no interaction is possible at high drift ratios. Both gusset assemblies had a clear distance from the column face to enable rocking of the columns freely. The clear gap of the lower gusset assembly to the west column was 3 in. (76 mm), as shown in Figure 2.21(b). The clear gap was 2⅛ in. (54 mm) between the upper gusset assembly and the face of the east column, as shown in Figure 2.21(d).

3. FABRICATION AND TEST PROCEDURE

3.1 Fabrication of Bridge Bent Specimen

The first task involved building the rebar cage necessary for the footings, columns, and beam for PT-BRB Bent. The rebar cage was constructed in the Structures Laboratory of the University of Utah. On the top of the footing rebar cage, it included eight No. 8 (25M) longitudinal bars evenly spaced at 4 in. (102 mm), while there were only six bars at the bottom. All bottom longitudinal rebars were approximately 8 ft 4 in. (2,540 mm) long and bent around the corner at each end to form a C-shape with arms of length nearly equal to the height of the footing. The top longitudinal bars consisted of three bars, one straight bar and two bent bars, tied into one to form the C-shape similar to the bottom bars. The elevation of the straight bar was less than the bent bars to facilitate building a 1 in. (25 mm) deep octagonal recess precisely at the center of the footing with a radius equal to 10½ in. (267 mm). These longitudinal bars were tied with No. 4 (13M) double hoops at 4 in. (102 mm) center-to-center spacing.

An additional supplementary reinforcement block cage in the form of 12 No. 5 (16M) straight vertical bars, equally spaced along the circumferential path, with 135° hooks on the top end and 90° hooks on the bottom end that were tied with No. 3 (10M) spirals with a pitch of 2.5 in. (64 mm), was placed at the center inside the main reinforcement cage. To accompany the unbonded 1 in. (25 mm) diameter post-tensioned bars, two 2 7/8 in. (73 mm) schedule 80 PVC pipes slightly longer than the footing height were fastened with straight steel bars and ties to preserve their original position at the time of concrete casting. The duct was sealed with duct tape to prevent concrete or any other material from entering the ducts during concrete casting. The reinforcement cage of the footing is shown in Figure 3.1.

Figure 3.1 Reinforcement cage of footing

To make the reinforcement cage for the column, two identical octagonal 1 in. (25 mm) thick wooden templates of 9¾ in. (248 mm) radius were cut and used for construction. Twelve holes, with a diameter of ¾ in. (19 mm), were drilled evenly at a radius of 6½ in. (165 mm) from the center. Two holes of 3 in. (76 mm) diameter were drilled at a distance of 3 in. (76 mm) on either side from the center for allowing the PVC pipe to pass through. The wooden template was used to make the reinforcement cage for the column. Twelve bars were kept inside the spirals of No. 5 (16M) and passed through the evenly spaced holes of wooden templates, whose distance was slightly greater than 7 ft (2,134 mm). The spiral hoop was

extended, with a pitch of 2½ in. (64 in.) over the length of 7 ft (2,134 mm), and the longitudinal bars were tied to the spirals. The PVC pipes were placed inside the reinforcement cage with the support of the holes at the templates, which were secured with extra bars. To confine the column ends, ½ in. (13 mm) thick octagonal steel collars were used. For this purpose, headed studs were used in the column so the octagonal steel collar could be welded. The headed studs were supported by ties and supporting rods wherever needed. The reinforcement cage for the column is shown in Figure 3.2.

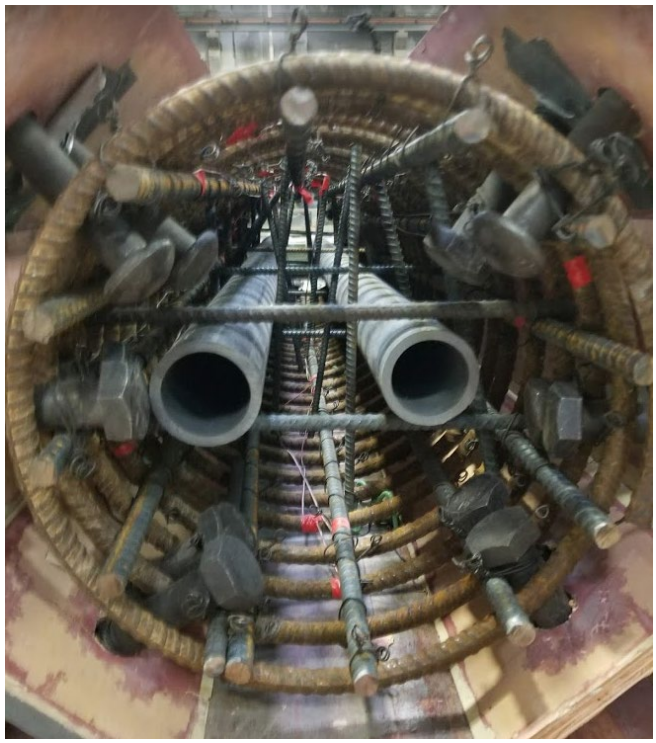

Figure 3.2 Reinforcement cage of column

For the main reinforcement cage of the cap beam, 36 No. 5 (16M) longitudinal bars were spanned across the cap beam and tied with No. 3 (10M) stirrups every 6 in. (152 mm). Initially, the 14 longitudinal bars of the inner loop were tied to the No. 3 (10M) stirrups at 6 in. (152 in) spacing. The remaining 22 longitudinal bars of the outer loop were tied to closed No. 3 (10M) stirrups every 6 in. (152 mm). These longitudinal bars were bent inwards at the end of the span at 90^{o} for the adequate development length. Similar to the footing, additional spiral confinement is placed, where the expected column would be directly underneath, inside the main reinforcement cage at a distance of 10 ft. (3,048 mm) apart. Two pairs of PVC pipes, 6 in. (152 mm) apart from each other, were placed inside the spiral and main reinforcement where the PT rods pass through. Since the point of application of the lateral load was the middle of the cap beam, four 30 in. (762 mm) long and 1 in. (25 mm) diameter 150 ksi (1,034 MPa) threaded bars were inserted through the cap beam reinforcement cage along the transverse direction, held by supplementary rebar and ties, at the correct position. The reinforcement cage of the cap beam is shown in Figure 3.3.

Figure 3.3 Reinforcement cage of cap beam

All reinforcement cages were transported to Forterra Structural Precast in Utah for casting of the concrete. For all specimens, formwork using plywood was built. For the footings and columns, only one formwork was built, and it was used twice. The footing formwork had an octagonal recess at the center. Concrete spacers were placed in the footings, columns, and cap beam for maintaining the concrete cover.

In order to place the strain gauges at the point of interest, the rebar surface was correctly ground before placement of the strain gauges. Once the strain gauges were held firmly in the rebars, they were sealed using silica gel so that even when the concrete was cast, they would not be destroyed or give false readings. The target compressive strength of the concrete was 10,000 psi (69 MPa). Self-consolidating concrete was used for the specimen, and a mechanical vibrator was used to ensure homogeneity of the concrete throughout the specimen. According to ASTM C3, concrete cylinders 4 in. x 8 in. (102 mm x 203 mm) were prepared for self-consolidating concrete. A total of 18 cylinders were cast in the first pour, while in the second pour, only 15 cylinders were cast to obtain the concrete compressive strength at the 7^{th}, 14^{th}, and 28^{th} days, and test day.

3.2 Test Procedure

3.2.1 Experimental Setup

Four W12x53 steel beams were bolted to the existing rigid fixed beams on the strong floor to raise the height of the whole test setup and bolt down the PT bars that would protrude from the footing surface underneath. Once the footings were located in the final position on top of the steel beams, ½ in. (13 mm) thick octagonal steel plates with two 3 in. (76 mm) holes, which were 6 in. (152 mm) apart, were placed in the octagonal recess of both footings. Similarly, one ½ in. (13 mm) thick polyurethane (PU) of the same size and shape as the steel plate was placed on top of the steel plate in both footings. The polyurethane plate was used to absorb the compressive stress from the column and transfer it to the footing to prevent crushing the toe of the column. The gap between the octagonal column and the recess in the footings was packed using grout to prevent sliding the column and ensuring adequate shear transfer between columns and footings. The polyurethane plate and shear key in the footing is shown in Figure 3.4.

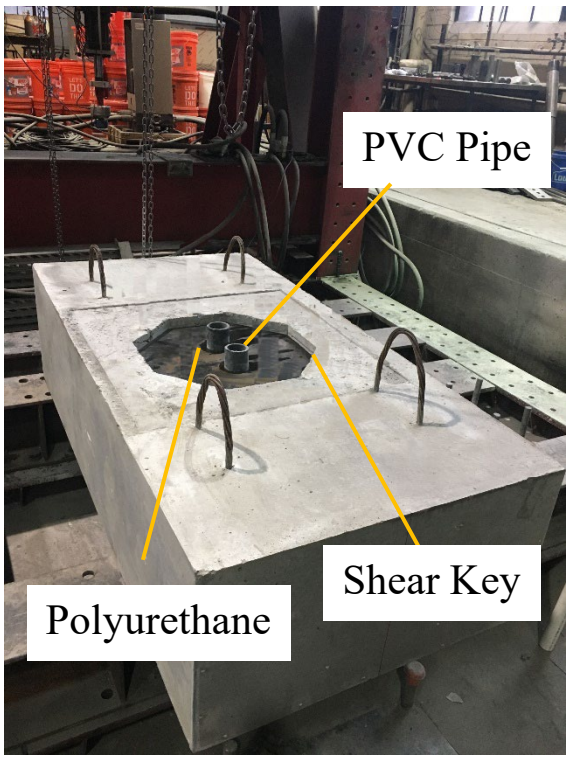

Figure 3.4 Polyurethane and shear key in octagonal recess of footing

Before placing the columns on top of the footings, an 8 in. x 7 ½ in. x ½ in. (203 mm x 190 mm x 13 mm) steel plate, which had two appropriate holes slightly greater than that of the shank of headed studs, was welded to the protruding studs, going around the perimeter both at the top and bottom of the column. Polyurethane is an amorphous thermosetting polyether polyol-based polymer. PU pads of ½ in. (13 mm) thickness were installed in the octagonal recess in the footing, as shown in Figure 3.4. PU pads were used because of their high deformation and damage resistant properties. PU exhibits large elastic deformation capacity, and its viscoelastic properties permit large deformation without damage (Nikoukalam and Sideris 2017).

At 10 ft (3,048 mm) apart, the two columns were placed vertically on top of the footings. The purpose of the BRB is to dissipate a high amount of energy and prevent damage to the cap beam and columns. Hence, the connection of the BRB to the cap beam and footing was designed to be very strong. The design of the gusset plate assembly and its connection was performed according to the AISC steel design manual. Two ¾ in. (19 mm) thick gusset plates were used to connect the BRB diagonally from the column-footing interface on the west side to the column-beam interface on the east side. The gusset plate assembly at the bottom contained one ¾ in. (19 mm) base plate, one 1 in. (25.4 mm) vertical stiffening plate, and two additional ½ in. (12.7 mm) triangular plates, as shown in Figure 3.5. These plates were designed to prevent twisting or buckling of the gusset plates. The upper gusset plate assembly at the top had two additional ¾ in. (19 mm) face-plates, as shown in Figure 3.6. Both gusset assemblies had a clear distance from the column's face to facilitate rocking of the columns. The grade of all steel plates used for the gusset plate assemblies was A572-50.

(a)

(b)

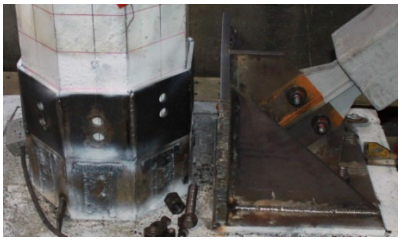

(c)

Figure 3.5 Lower gusset assembly details: (a) stiffener in the lower gusset assembly; (b) lower gusset in footing; (c) gusset assembly and gap

Six holes at the west footing were drilled vertically for the connection of the prestressing rods to the base plate of the gusset assembly. Similarly, six holes were drilled transversely at the top of the cap beam for the connection of the upper gusset assembly to the cap beam. These rods were prestressed up to half of their capacity, i.e., 60 kip (267 kN). There was a gap between the gusset assembly and the column so that the column could rock without any contact with the gusset assembly both at the beam-column interface and footing-column interface. The BRB was bolted in the final position, with one end connected to the lower gusset assembly and the other end connected to the upper gusset assembly. Box beams were bolted down with the grade beam of the floor for fixing the footings. To prevent against a sliding mechanism, hollow beams were welded near the ends of the footings.

(a)

(b)

Figure 3.6 Upper gusset assembly details: (a) stiffener in the upper gusset assembly; (b) connection of upper gusset assembly with beam

Two channel beams were attached to the cap beam with four bolted assemblies at the different intervals, which were connected to the hydraulic actuator to establish displacement-controlled quasi-static cyclic lateral force. Along with the increase in lateral load, the axial force in the axial rods used to apply axial load would gradually increase either in pull or push. A rolling assembly was developed with rollers and steel plates and a hydraulic jack was used with an I-beam to apply the axial load, as shown in Figure 3.7.

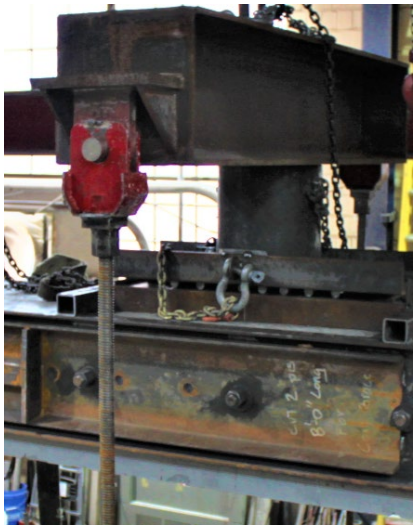

(a)

(b)

(c)

Figure 3.7 Axial load assembly and placement of rollers: (a) axial load assembly; (b) placement of rollers; (c) rollers at connection

The lateral load was applied using a horizontal 220-kip (890 kN) servo-controlled hydraulic actuator that was attached to the self-reacting strong frame. Before starting the test, an axial load was applied with the hydraulic jack at the top surface of the mid-span of the cap beam in the vertically downward direction. The two vertical axial rods represent the gravity load applied to the system. The primary purpose of the axial rods is to transfer a constant axial load to the bent throughout the test. The applied axial load was set to 6.0% of the axial capacity of the columns to simulate vertical loads on the bridge bent. After applying the axial load, the post-tensioning force was applied to two PT bars in each column up to the required value after losses with a torque wrench. The setup of the PT-BRB Bent test is shown schematically in Figure 3.8.

Figure 3.8 Experimental setup of PT-BRB Bent test

3.2.2 Instrumentation

Since the cap beam and footings were rigid, no strain gauges were attached to any rebars inside the reinforcement cage. Thirty-two strain gauges were placed in the two columns for recording the strain in the longitudinal bars and spiral hoops, as seen in Figure 3.9. They were installed in the plastic hinge region of the columns, at a height equivalent to half of the column width, i.e., 9 in. (229 mm), from both ends of the columns. Four strain gauges were placed at the outermost longitudinal bars in the four directions at the top and bottom. Similarly, four additional gauges were placed at adjacent spiral hoops in the east, west, north, and south direction of the top and bottom ends of the columns. Several strain gauges were attached to the steel plates of both the lower and upper gusset assemblies to record the strain.

Four load cells were placed at the top portion of the PT rods to measure the post-tensioning force in each tendon, as seen in Figure 3.9. The load cells were placed over the 1 in. (25 mm) steel plate situated just on top of the cap beam surface. During the test, one LVDT, attached at the end of the cap beam to a fixed surface, was used to record the actual displacement of the bridge bent. Linear variable differential transformers (LVDTs) were used to find the gap opening, base rotation, and global vertical movement of the specimen. A total of four LVDTs were installed on each column, one on either side of the top and

bottom of the column, as seen in Figure 3.9. Two LVDTs were used to calculate the elongation of the BRB steel core by placing them on either end of the BRB.

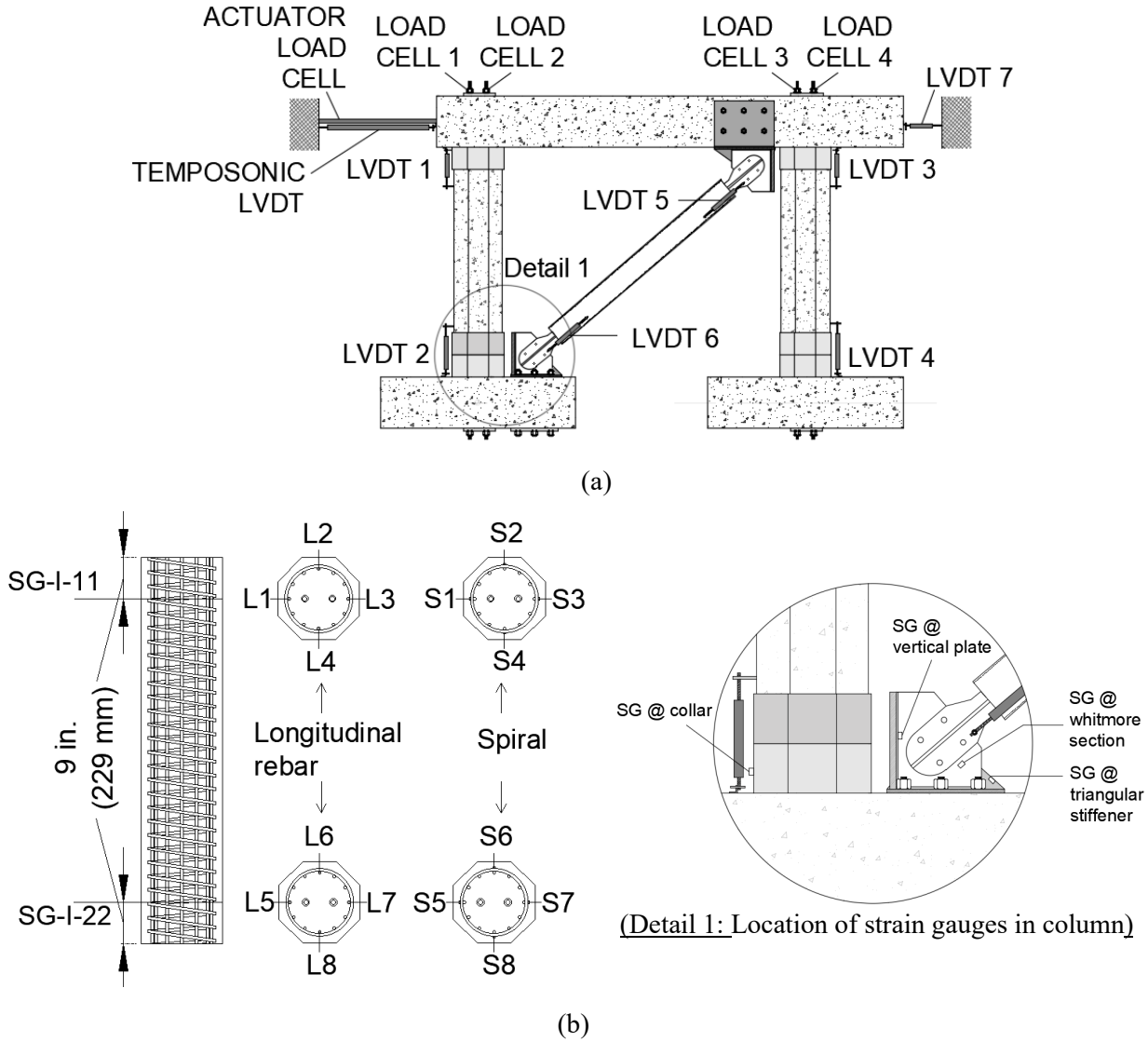

Figure 3.9 Instrumentation scheme: (a) load cells and LVDTs; (b) strain gauges

3.2.3 Displacement History

A quasi-static lateral cyclic load was applied to the bent specimen using displacement control at a vertical distance of 94 in. (2.40 m) from the top surface of the footing. The loading protocol used had increasing drift ratios, as shown in Figure 3.10. The drift ratio is defined as the ratio of lateral displacement to the effective column height of the structure. For each drift ratio, two complete cycles were employed at 0.25%, 0.5%, 1.0%, 1.5%, 2.0%, 2.5%, 3.0%, 3.5%, 4.0%, 5.0% and 6.0%. During the entire test, the displacement rate was programmed to be 0.02 in./s (30.5 mm/min); the test was stopped manually when the cycle of 6.0% drift ratio was completed, i.e., after the completion of 22 cycles.

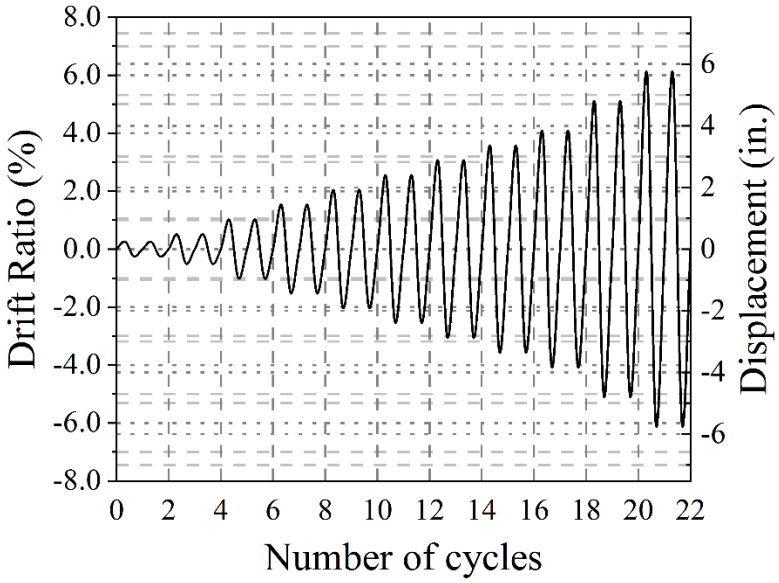

Figure 3.10 Loading protocol

4. EXPERIMENTAL OBSERVATIONS

The PT-BRB Bent specimen was tested under reversed cyclic quasi-static lateral load with constant axial load up to a 6.0% drift ratio. The test was terminated after the BRB fractured during the first cycle of the 6.0% drift ratio. In the test, no cracks were seen during the whole experiment, and the residual drift was low even at high drift ratios. In the following sections, the experimental results and visual observations are discussed; the hysteretic response, post-tensioning forces in the PT bars inside the columns, the response of the BRB, the energy dissipation, the stiffness degradation, and the residual drift are discussed in detail.

4.1 Hysteretic Response

Figure 4.1 shows the hysteresis curves of the PT-BRB Bent. The peak lateral strength was 139 kip (725 kN) during the second positive cycle of 5.0% drift ratio (push) and 160 kip (681 kN) during the first negative cycle of 6.0% drift ratio (pull). The BRB added additional lateral strength to the PT-BRB Bent. In most cycles, the PT-BRB Bent gained maximum strength in the compression cycle because the BRB has more strength in compression than in tension. Even after the BRB fractured in the tension cycle during the 6.0% drift ratio, the strength in the compression cycle was still high due to brace action of the BRB, which provides a sizeable compressive force. No significant loss in the lateral strength of the specimen was observed until the BRB fractured in the 5.0% drift ratio push cycle. The strength of the system then dropped during the first cycle of the 6.0% drift ratio by 21 kip (43 kN). The lateral force vs. drift ratio curve shows symmetric and stable curves with good energy dissipation. The hysteresis curves indicate that the overall force-displacement performance of the test specimen was controlled by the presence of the BRB.

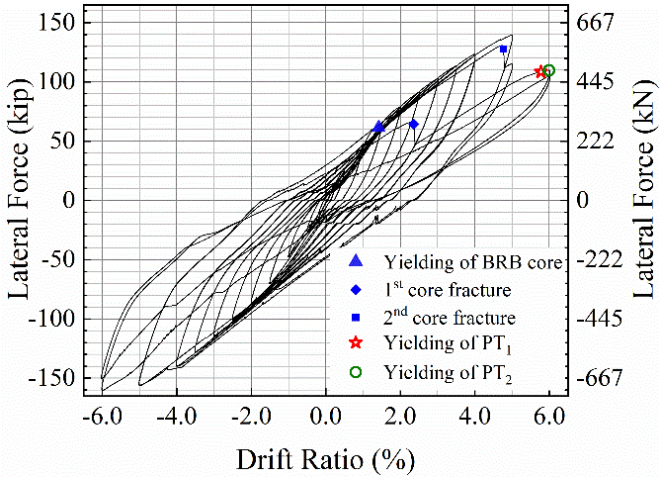

Figure 4.1 Load-displacement hysteretic curve of PT-BRB Bent specimen

The highlight of the test was the absence of concrete cracking or spalling during the entire experiment. Both columns started rocking at the 0.25% drift ratio; vertical opening at the column-to-footing and column-to-cap beam joints was visible. Gap opening was maximum at the end of the 6.0% drift ratio, as shown in Figure 4.2(a). Rotation of the bottom joint of the west column was found using LVDT 2 of Figure 3.9(b) and is shown in Figure 4.2(b) with a blue line; rotation of the top joint was found using LVDT 1 and is shown with an orange line. The rotation at the top and bottom of the columns was

symmetric up to a drift ratio of 5.0%. Once the BRB steel core fractured, the rotation of the bottom of the west column in the push direction reached approximately 2.0 times the rotation in the pull direction; similarly, the rotation of the top of the west column in the pull direction reached approximately 2.5 times the rotation in the push direction.

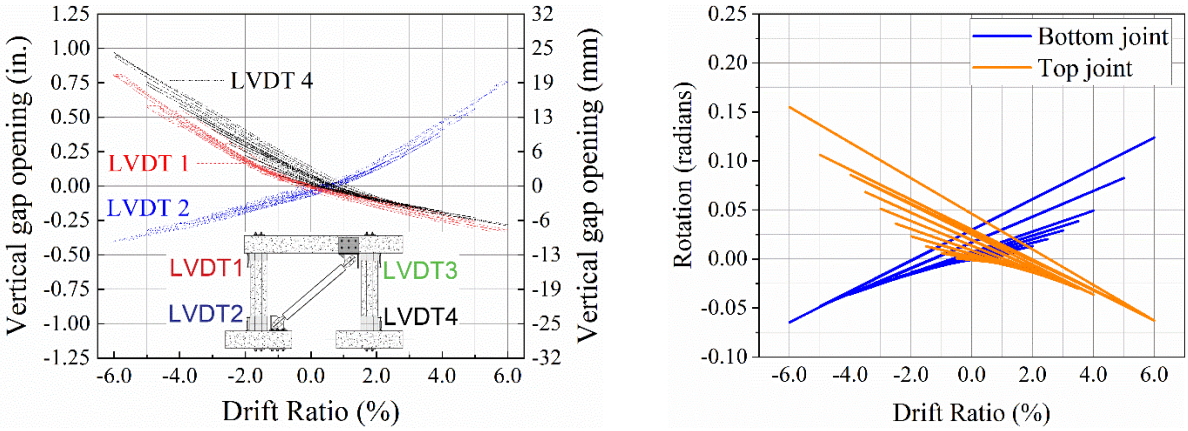

(a) (b)

Figure 4.2 Joint gap opening and column rotation: (a) vertical gap opening recorded by LVDTs; (b) rotation of top and bottom joints of west column

The grout in the octagonal recess of the west footing started cracking at the 5.0% drift ratio due to rocking of the post-tensioned column. The BRB steel core elongated and was exposed during the push cycle as the drift ratio increased. There were two audible sounds: (a) during the second push cycle of the 5.0% drift ratio and (b) during the first push cycle of the 6.0% drift ratio, from tensile fracture of the BRB steel double core. After the test, the end concrete surfaces at the top and bottom of the columns had minimal cracks, as shown in Figure 4.3(a). The PU plate and PVC pipes were not damaged. The PT bars were slightly bent at the column-to-footing and cap beam-to-footing interfaces due to stress concentrations, as shown in Figure 4.3(b).

(a) (b)

Figure 4.3 Column and PT bar condition after test completion: (a) top of column; (b) PT bars

The red paint drawn at the BRB steel core-to-casing interface separated from the original markings during the first push cycle of the 1.5% drift ratio due to yielding of the steel core, as shown in Figure 4.4(a). The steel core inside the casing was exposed at the peak of each successive drift ratio due to BRB steel core elongation, as shown in Figure 4.4(b) and Figure 4.4(c), for the first push cycle of the 5.0% drift ratio. One of the BRB steel cores fractured in the second push cycle of the 5.0% drift ratio; the second steel core fractured in the first push cycle of the 6.0% drift ratio, after which the steel core moved freely, as shown in Figure 4.4(d).

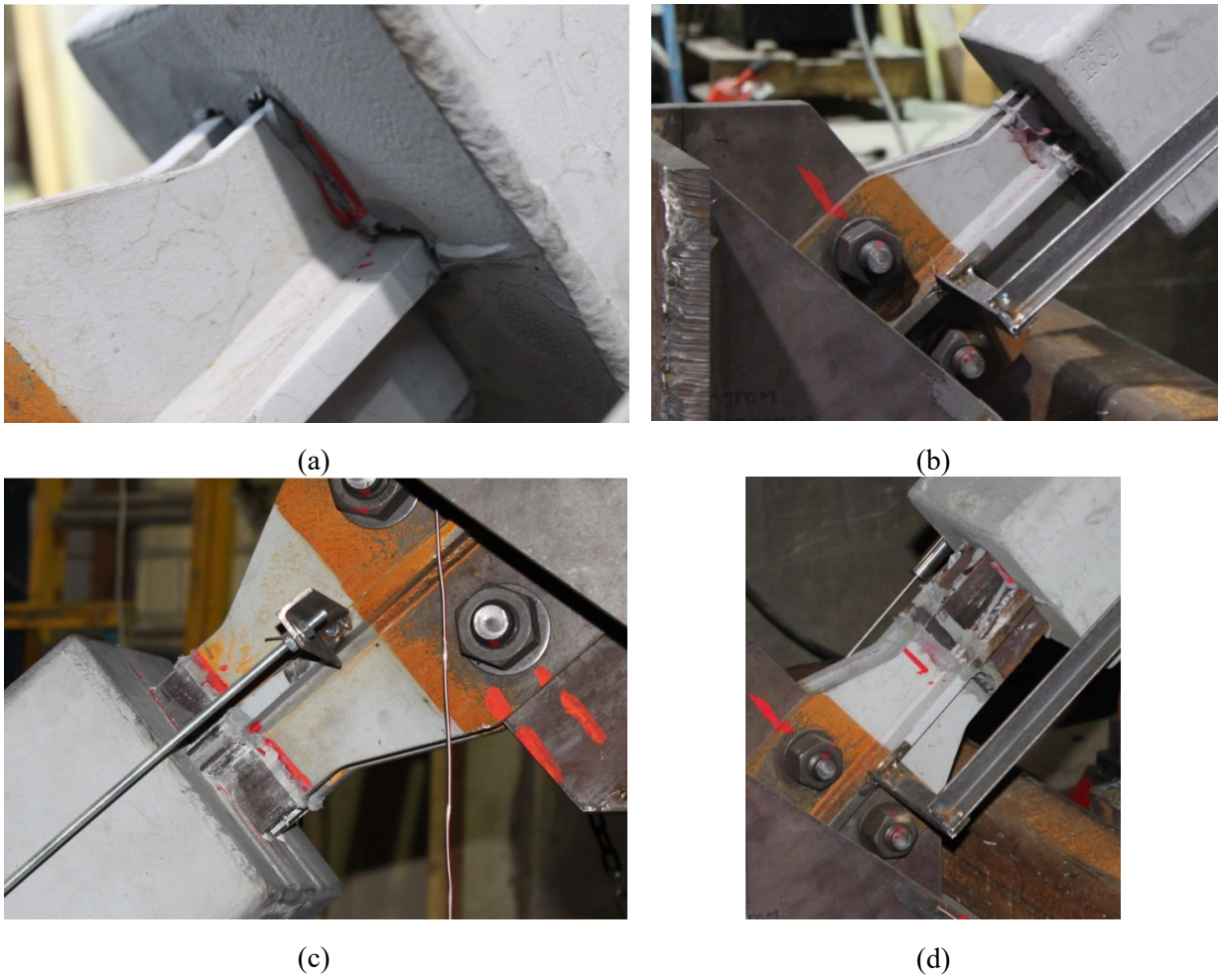

Figure 4.4 Elongation of BRB: (a) yielding of steel core at 1.5% drift ratio; (b) bottom at first push cycle of 5.0% drift ratio; (c) top at first push cycle of 5.0% drift; (d) bottom after fracture at second push cycle of 6.0% drift ratio.

4.2 Axial Force

Figure 4.5 shows the force in the two rods used to apply the axial load. The axial load application system with rollers performed very well, and the maximum axial load reached was 40% greater than the initial axial load. The axial load first decreased when returning to the initial position of the horizontal actuator after completing one-half cycle. It was only at the 4.0% drift ratio that the axial force increased from the initial value (Figure 4.5). The increase in axial load is attributed to elongation of the axial rods. The axial rods never yielded in this test.

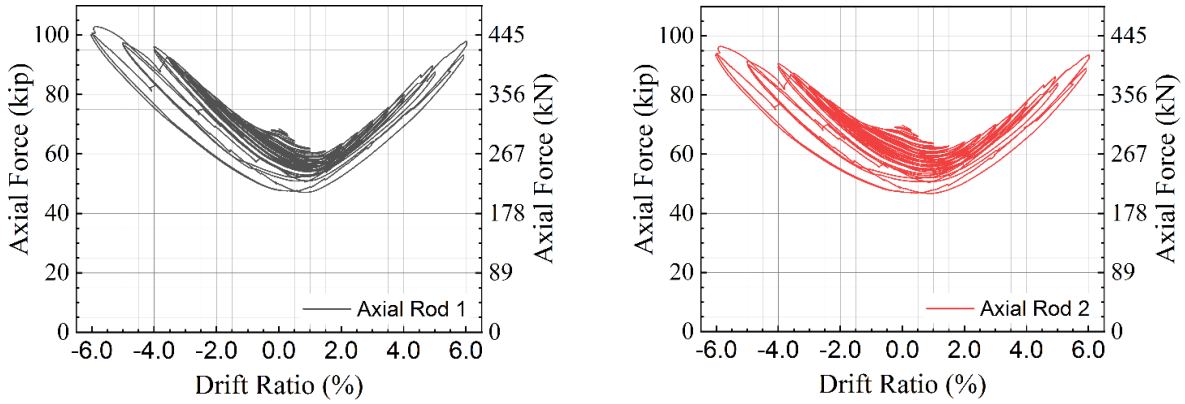

(a) (b)

Figure 4.5 Axial force at every drift level; (a) axial rod 1; (b) axial rod 2

4.3 Post-tensioning Force

All PT bars in the columns were stressed until the post-tensioning force reached 50 kip (222 kN), as recorded by the load cells. The initial post-tensioning forces in each PT bar are shown in Table 4.1. All post-tensioning force values are plotted against the drift ratio, as shown in Figure 4.6. As the test progressed, the post-tensioning forces in all tendons gradually dropped until the end of the first two cycles, i.e., up to 0.5% drift ratio. Up to the first half negative cycle of the 1.0% drift ratio, the post-tensioning forces in the tendons remain below the initial post-tensioning forces; subsequently, the two tendons in the east column reached a value of 51 kip (226 kN) and 50 kip (223 kN), slightly greater than the initially applied stress in those tendons. However, the stress in the PT bars was still less than the initial stress in the east column. During the peak of the first negative cycle of 1.5% drift ratio, all tendons recorded post-tensioning forces greater than the initial values. Until the end of 2.5% drift ratio, the average force in PT bars of the west column had higher values than the tendons of the east column during positive cycles; during negative cycles, the opposite was true.

Table 4.1 Post-tensioning force and losses

Specimen	PT-BRB Bent			
	West Column		East Column	
	PT_1	PT_2	PT_3	PT_4
Initial post-tensioning force (kip)	48.27	50.08	50.61	49.78
Maximum post-tensioning force (kip)	103.15	104.94	98.56	97.32
Increment percentage (%)	113.69	109.53	94.74	95.48
Minimum post-tensioning force (kip)	19.03	20.61	19.37	20.89
Loss Percentage (%)	60.58	58.85	61.72	58.05

Note: 1 kip = 4.448 kN

From the 3.0% drift ratio, the two PT bars at the west column were always stressed higher than the PT bars at the east column during both push and pull. Similarly, the force in all PT bars at the peak drift was always greater than the initially applied stress from this cycle onward.

All the tendons were stressed to the maximum value in the last cycle, as seen in Figure 4.6. The highest post-tensioning force can be seen in Table 4.1 for each PT bar. Among all the PT bars, the maximum force was recorded in PT_2 at 105 kip (467 kN), which is about 109.53% more than the initially applied stress. The two PT bars in the west column (PT_1 and PT_2) just barely yielded, whereas the PT bars in the east column did not yield, as seen in Figure 4.6. Even though all the PT bars recorded their highest value at 6.0% drift ratio, these occurred in different cycles. PT_1, PT_3, and PT_4 reached the maximum value in the peak drift of the first positive half cycle, while PT_2 recorded the maximum in the first negative half cycle. The post-tensioning forces in all the tendons after completing each cycle were always less than the initial value at that cycle.

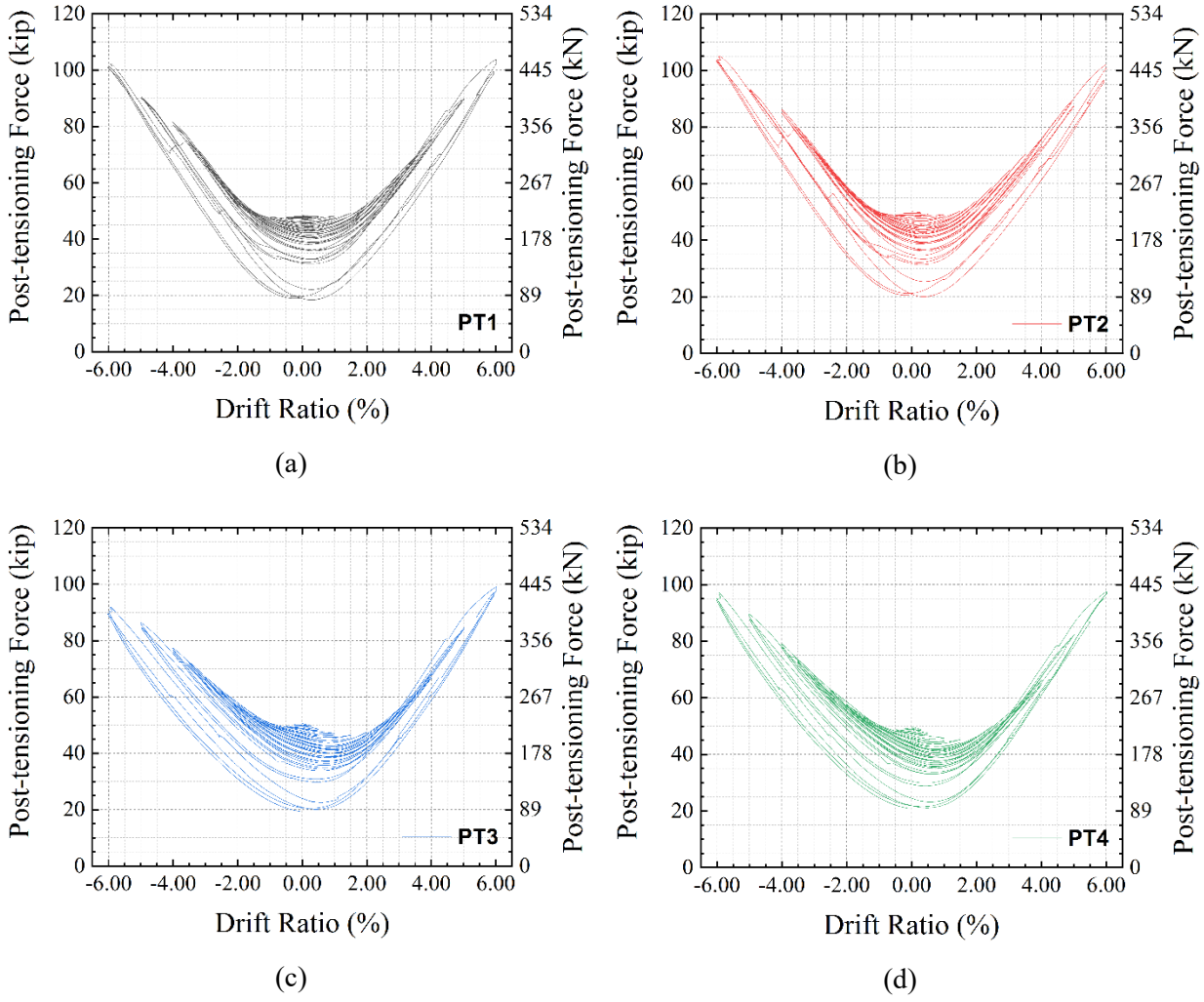

Figure 4.6 Post-tensioning force vs. drift ratio for PT bars in PT-BRB Bent

Up to the 4.0% drift ratio, the post-tensioning force losses after completion of each cycle were below 2.5 kip (11 kN) than the post-tensioning force at the start of a cycle, as seen in Figure 4.7. At the end of the 5.0% drift ratio, the post-tensioning force in all the PT bars decreased by 5 kip (22 kN) than the post-tensioning force at the start of 5.0% drift ratio, which is almost double the value of previous cycles. The

main reason for the increased losses is due to the two PT bars yielding in the west column. At the end of the 6.0% drift ratio, there was a tremendous drop in the post-tensioning force because of the yielding of all PT bars.

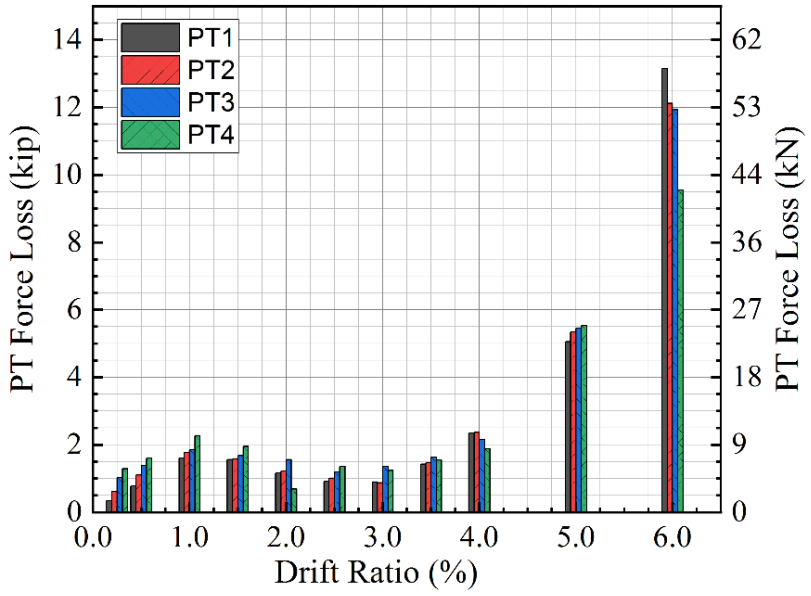

(a)

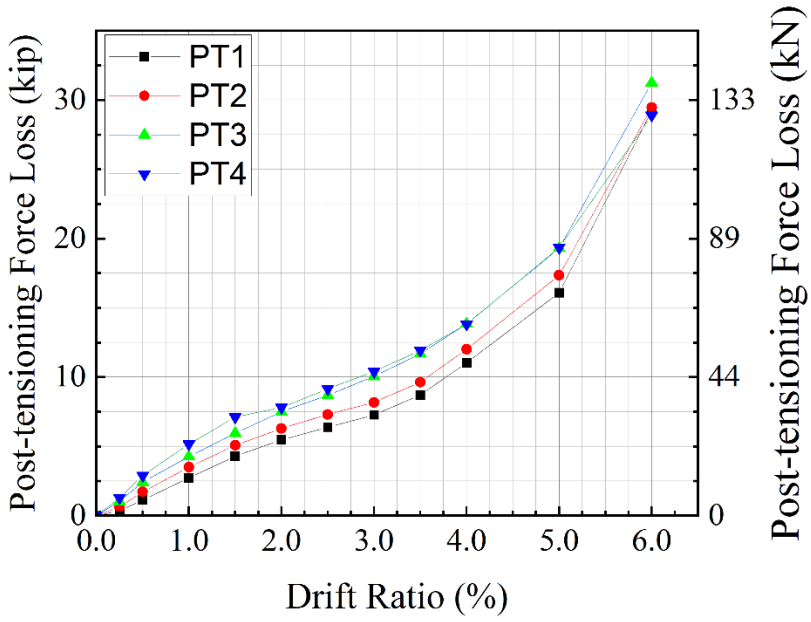

(b)

Figure 4.7 Post-tensioning force loss: (a) post-tensioning force losses in between every drift ratio cycle in PT-BRB Bent; (b) post-tensioning force loss from initial post-tensioning force in PT-BRB Bent

4.4 BRB and Gusset-Assembly Response

Figure 4.8(a) shows the strain in the Whitmore section at the lower steel gusset plate, which experienced tensile strains during the push cycles and compressive strains during the pull cycles; the low strains demonstrate low levels of stress. Once the steel core fractured, the strain dropped from 0.15 to 0.07 times the yield strain; after fracture of the second steel core, a negligible strain was recorded in tension. Figure 4.8(b) shows that the vertical steel plate experienced a very low strain of 0.03 times the yield strain, which implies that it functioned as designed. Figure 4.8(c) shows the strain in the north triangular stiffener; the plate experienced compressive stresses during the push cycle up to 0.14 times the yield strain and tensile stresses during the pull cycle up to 0.11 times the yield strain. The two stiffeners, in conjunction with the gusset plate, prevented twisting and buckling of the gusset and vertical steel plate. The nonlinear response of the gusset assembly was affected by the inelastic response of the BRB.

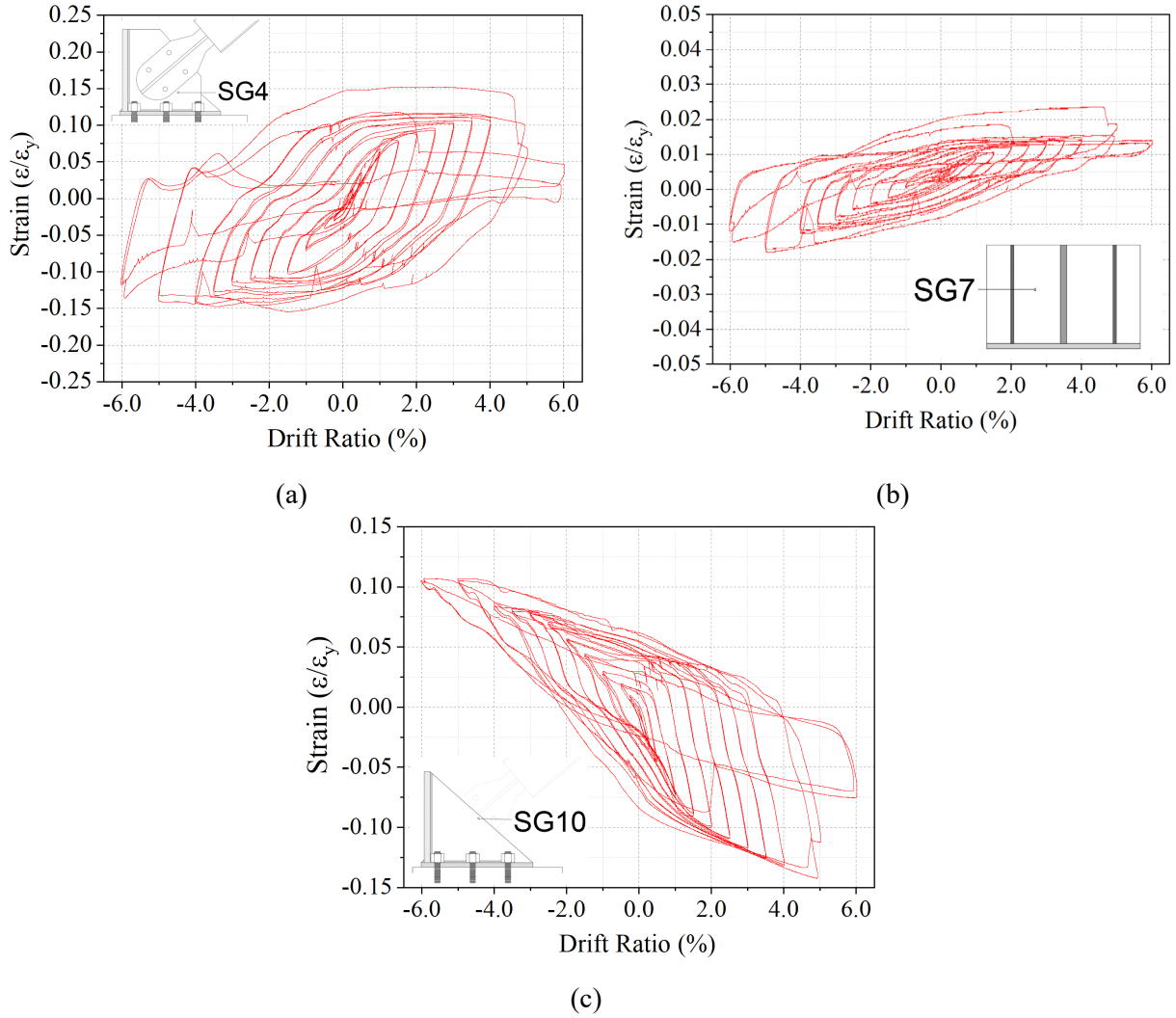

Figure 4.8 Strain in lower steel gusset assembly: (a) strain gauge 4 at Whitmore section; (b) strain gauge 7 at vertical plate; (c) strain gauge 10 at triangular stiffener

The axial deformation of the steel core at each drift ratio was measured by two LVDTs, one attached at the top end and one at the bottom end of the BRB, as indicated in Figure 3.9(a). Figure 4.9 shows BRB axial deformation versus horizontal drift ratio where the graph is linear up to 1.0% drift ratio. The yield strain of the steel core of 1,540 microstrain was exceeded at 1.5% drift ratio. The axial deformation curves starting at the 1.5% drift ratio and at greater drift ratios become highly nonlinear. At fracture of the first steel core at 5.0% drift ratio, the strain in the steel core was equal to 32 times the yield strain.

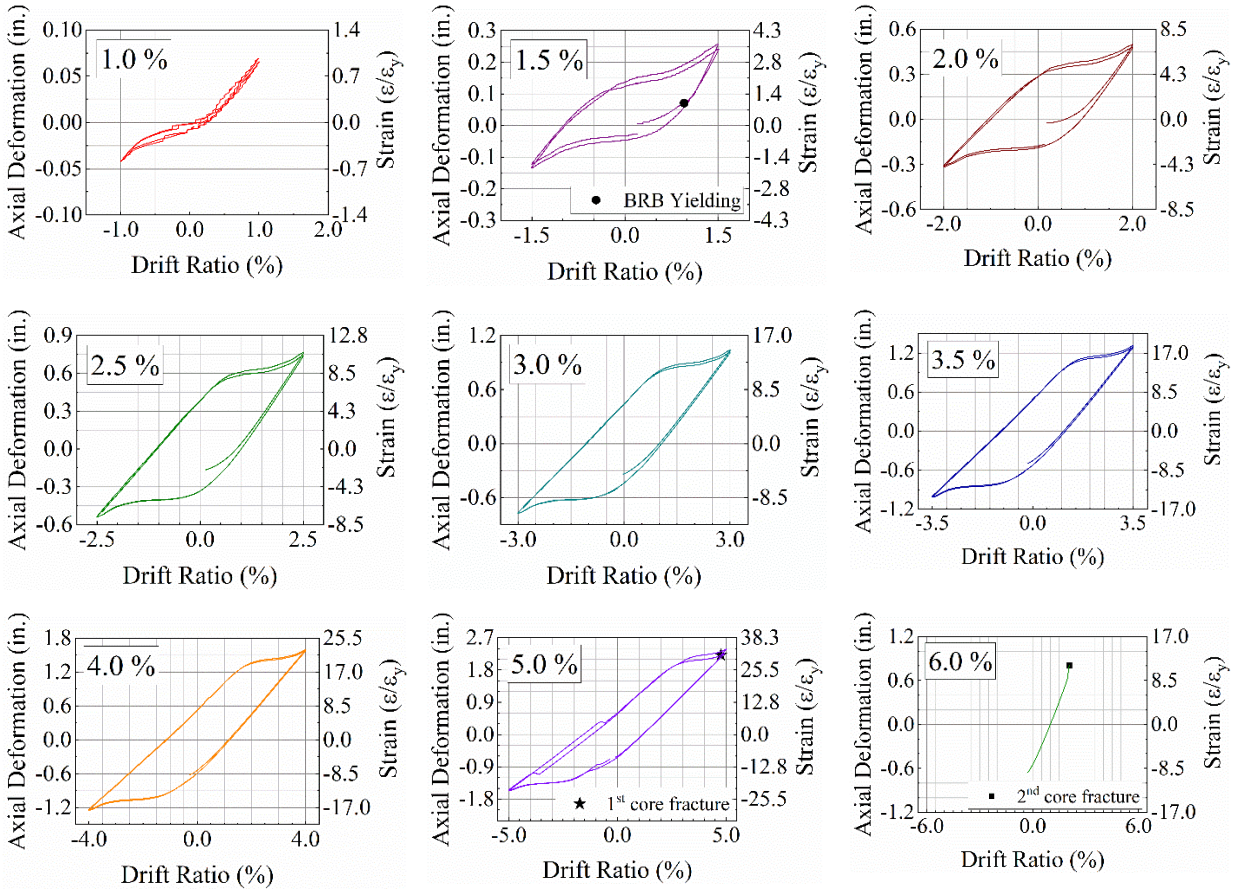

Figure 4.9 Axial deformation of BRB core at different loading cycles

4.5 Residual Drifts and Self-centering

A comparison of residual and maximum horizontal displacements is shown in Figure 4.10. Re-centering is due to axial forces from gravity and post-tensioning forces. Once the BRB steel core yields at 1.5% drift ratio, strain hardening creates a permanent residual displacement. As the drift ratio increases from 1.5% up to the second cycle of the 5.0% drift ratio, when the steel core fractured, excessive accumulation of plastic deformation of the steel core impedes re-centering. The maximum residual drift was 2.3% [2.19 in. (56 mm)] in the first push cycle and 1.6% [1.53 in. (39 mm)] in the first pull cycle of the 5.0% drift ratio when the steel core fractured. Residual drift was smaller during the pull cycles compared with the push cycles because the buckled BRB steel core was in compression.

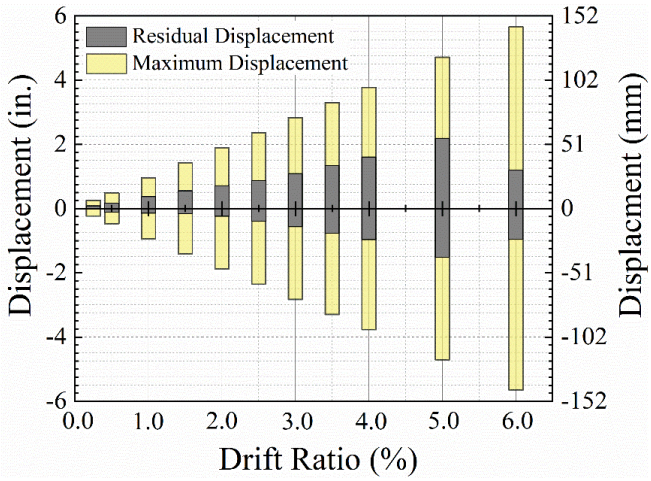

Figure 4.10 Residual displacement at every drift ratio

In this type of hybrid system with both post-tensioning and a BRB, the system returns to its original position upon unloading. Provided the energy dissipating device (BRB) dissipates energy within a certain threshold, the axial force from the superstructure and the prestressing force brings the structure back to its original position by overcoming the bending moments created by the lateral force. The permanent residual drift obtained in the PT-BRB Bent was high since it resulted from the residual strains of a BRB. The relative self-centering index for the PT-BRB Bent at every drift ratio is seen in Figure 4.11. The relative self-centering index is defined as the ratio of the difference of the maximum displacement minus residual displacement divided by the maximum displacement at a particular drift ratio. For perfect self-centering systems, the value of the index is 1.0. The PT-BRB Bent shows a higher self-centering index at the beginning of the test; the index gradually decreases due to the residual strain in the BRB. After the BRB fractures, the re-centering index increases at 6.0% drift ratio because the specimen is technically now a bent without a BRB and has a high re-centering capability.

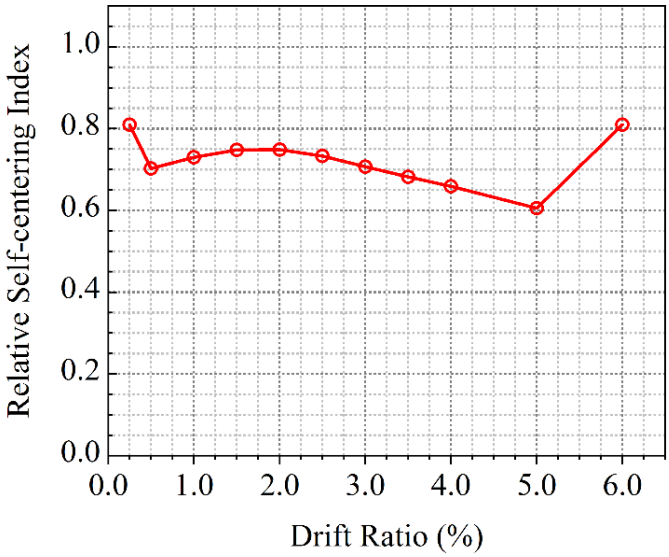

Figure 4.11 Re-centering index at every drift ratio

4.6 Cumulative Hysteretic Energy Dissipation

One of the essential parameters of a ductile system is the hysteretic energy dissipating capability, which is the ability of the structure to dissipate energy through a combination of elastic and inelastic deformations. The energy dissipation of the hybrid post-tensioned rocking system is usually less than a conventional monolithic system because a high amount of energy is dissipated by concrete cracking, crushing and spalling, and yielding and buckling of the longitudinal bars and spirals in the conventional monolithic system. The main objective of using a BRB in a self-centering hybrid bridge bent was to ensure that the bridge dissipates large amounts of hysteretic energy, while providing good self-centering.

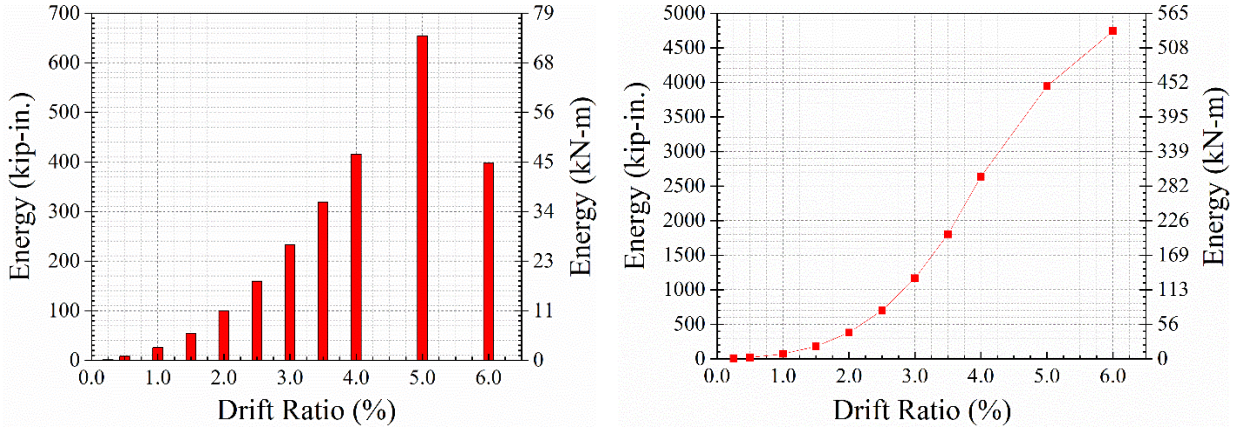

(a) (b)

Figure 4.12 Energy dissipation of PT-BRB Bent: (a) average hysteretic energy per cycle; (b) cumulative hysteretic energy

The area enclosed by the hysteresis curve gives the hysteretic energy dissipated. The total average energy at each drift level is presented in Figure 4.12(a). Figure 4.12(b) presents the hysteretic energy accumulated at all drift ratios. There is an excellent energy dissipation by the PT-BRB Bent specimen above the 1% drift ratio. The hysteretic energy dissipated by the PT-BRB Bent even after the BRB fractures is appreciable since the BRB is acting as a brace in compression.

The system equivalent viscous damping ratio was relatively constant throughout the experiment because the system is a precast post-tensioned bridge bent with minimal damage, as shown in Figure 4.13. As the drift level is increasing, the energy dissipated by the BRB is increasing. As seen in the Figure 4.13, the BRB has not yielded until 1.5% drift ratio, so the equivalent damping ratio is almost the same as in previous cycles. The BRB yields after 1.5% drift ratio, after which it is clear that the damping ratio increases until the 5.0% drift ratio, when the BRB fractures. The sharp fall marks the fact that the BRB is fractured; after the 5.0% drift ratio, no energy is being dissipated, and no additional damping is introduced to the bridge bent.

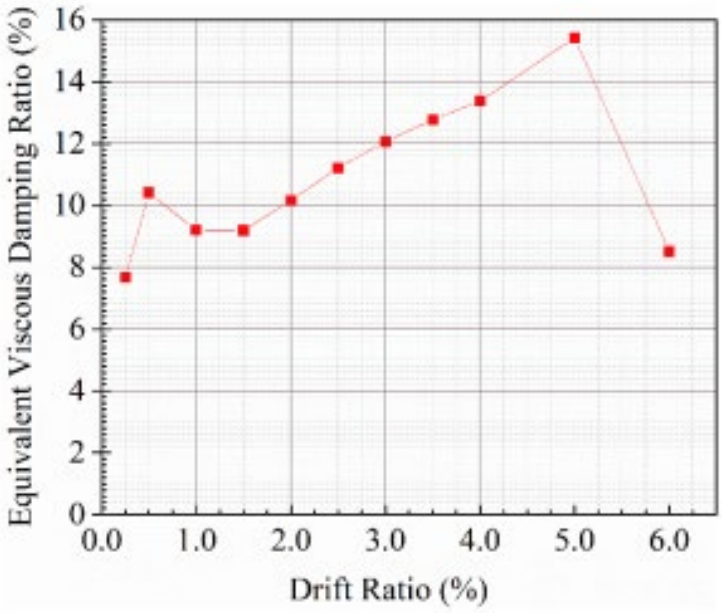

Figure 4.13 Equivalent viscous damping ratio

4.7 Performance of Columns

The strains in the outermost longitudinal bars at the bottom of the east column and top of the west column are presented in Figure 4.14(a) and 4.14(b). The longitudinal bars on the east side at the bottom of the east column experienced maximum strains throughout the test compared with the remaining longitudinal bars or spirals due to high compressive stresses applied at the column toe. These bars yielded in the first cycle of the 6.0% drift ratio, and reached 1.1 times the yield strain in compression, as shown in Figure 4.14(a). When the specimen was subjected to push cycles, the compressive force at the toe was maximum in both columns, causing the east longitudinal bars to experience maximum compressive strain, while the longitudinal bars at the bottom west face had a minimal strain due to opening of the joint. The longitudinal bars at the top experienced the maximum compressive strain when the specimen was subjected to pull cycles, as shown in Figure 4.14(b); however, because of the smaller bending moments at the column top due to absence of shear keys at the top of the columns, the top bars experienced only 0.5 times the yield strain in compression.

The hoop strain in the spiral at the 6.0% drift ratio was only 0.07 times the tensile yield strain, as shown in Figure 4.14(c) for the west column bottom; the concrete column is confined by the steel collar, and this reduces the demand on the steel spiral inside the column. Figure 4.14(d) corroborates this fact and shows the hoop strain of the bottom steel collar of the west column, which reached 0.44 times the yield strain during the second pull cycle of the 6.0% drift ratio.

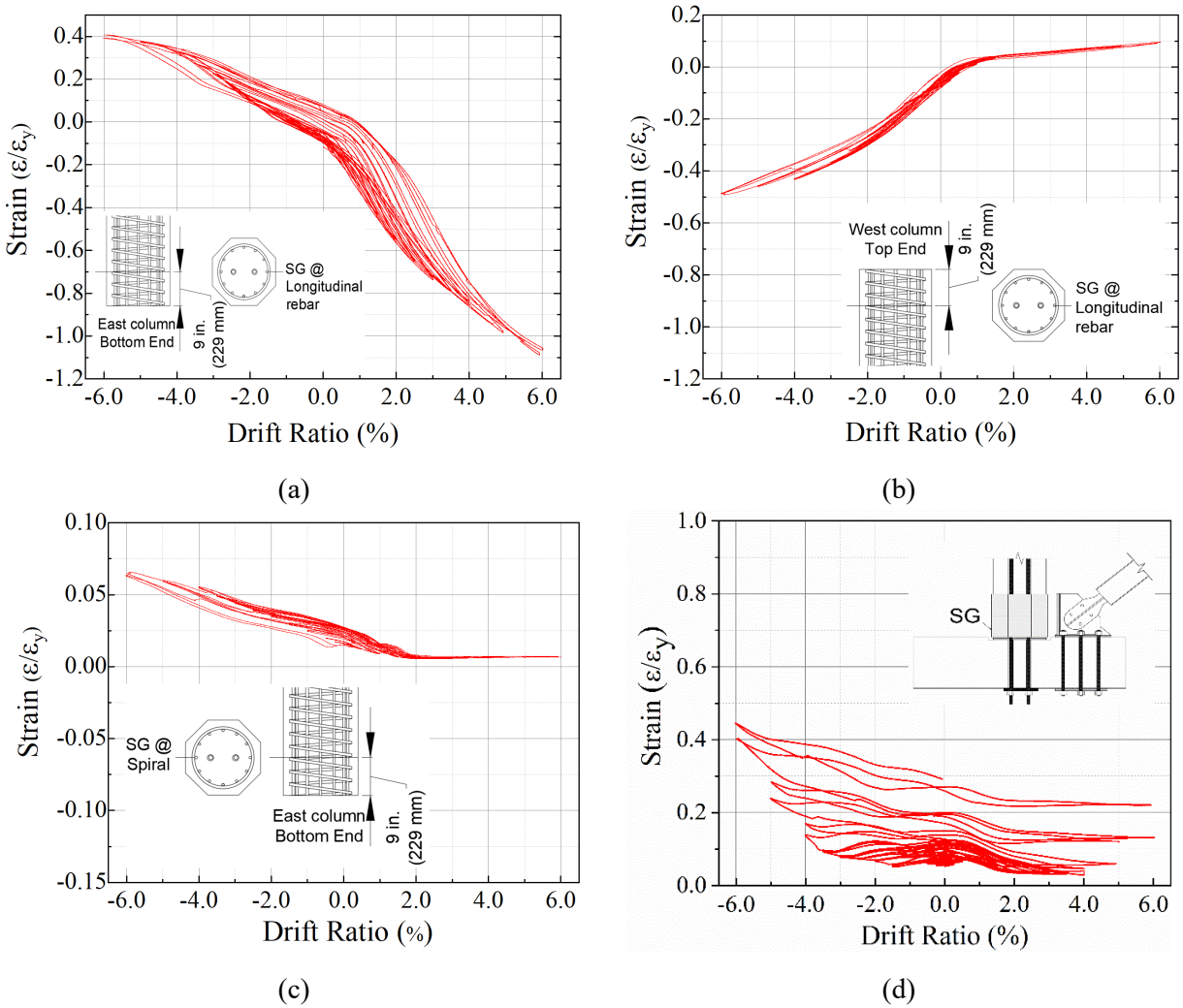

Figure 4.14 Normalized strain gauge in plastic hinge regions: (a) longitudinal bars at east face of east column bottom; (b) longitudinal bars at east face of west column top; (c) hoop strain in spiral of west column bottom; (d) strain in steel collar of west column bottom.

4.8 Stiffness Degradation

The stiffness of the specimen is degraded as drift increases, as seen in Figure 4.15. The stiffness at each cycle is the average of the secant stiffness through the origin to the maximum displacement in both the positive and negative direction. The stiffness of the system was high at the beginning of the test and decreased at higher drift ratios. This degradation of stiffness can be attributed to yielding and fracture of the BRB and prestressing losses. The stiffness is decreasing because the core is yielding steadily until it finally fractures at the 5.0% drift ratio. The sharp drop in stiffness between the last two drift ratios is due to the BRB core fracture.

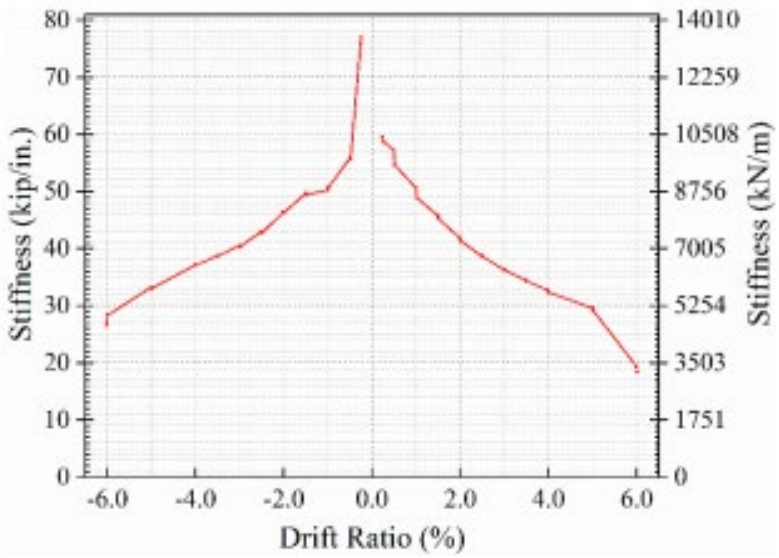

Figure 4.15 Stiffness degradation of PT-BRB Bent

5. ANALYTICAL MODEL OF THE PT-BRB BENT

5.1 Background

Early observations in the 1952 Arvin-Tehachapi and 1960 Chilean earthquakes, showed that even though some of the box-like electric power transformers rocked as rigid bodies and overturned, most structures that displayed rocking behavior survived (Housner 1963). The overturning phenomenon of such bodies could be avoided by connecting internal or external members using pre-tensioning or post-tensioning (Rahmzadeh et al. 2018). Most of the research on post-tensioning elements was carried out in the 1990s in which beam-column building joints were connected with bonded or unbonded post-tensioning elements. Research on piers and bridge bents included seven-wire strands or high strength bars, which prevented overturning of the structures (Priestley and Tao 1993; Priestley and MacRae 1996; Sritharan et al. 1999). The PT elements did not just prevent overturning of the structures but also displayed excellent re-centering of the system and prevented damage in the joints that would have otherwise occurred in monolithically built structures. When external energy dissipating elements are included, these systems display high energy-dissipation ability similar to monolithically built structures and exhibit less or no residual displacements during large earthquakes.

ABC is a construction technique that involves assembling rigid bodies such as precast concrete elements into one system, which drastically lowers total construction time (Culmo 2011). Bridge structures in seismic regions require suitably detailed analytical models to predict precise behavior patterns during large earthquakes. Most of the damage in such structures is concentrated near the joints and plastic hinge regions during large seismic events. Moreover, the post-tensioning force may completely die out with incorrect structural analysis modeling (Erkmen and Schultz 2009). Analytical models of structures built with ABC hybrid systems are limited, and widespread use of such models is still in its infancy.

Structural integrity of bridges built in seismic regions with ABC technologies can be maintained, and damage can be minimized if the analytical model is accurate. As an example, if there is only one PT bar inside a precast concrete column, inaccurate analysis and design may lead to a large gap and inefficient re-centering of the column. Hence, the number and size of PT bars as well as the value of initial post-tensioning stress should be carefully chosen so that structural efficiency is not reduced, thus delivering the intended performance. By using an accurate numerical model, the design procedure can be improved, the gap opening can be reduced, and damage at the column toe due to rocking can be minimized. Moreover, with an accurate numerical model, a suitable value for initial post-tensioning stress and prevention of PT bar yielding can be achieved, which improves re-centering.

When two or more PT bars are required in a column, exact placement of the PT bars is critical; the distance between the PT bars should not be small, since this might lead to crushing of the column core. The PT bars should not be placed near the exterior of the column since that would generate large tensile strains in the PT bars and potential crushing of the column surface. Correct numerical analysis gives useful input regarding the placement of the PT bars inside precast columns for good structural performance. A good model also provides accurate representation of the energy dissipating elements in a hybrid structure in earthquakes. Therefore, an accurate and reliable modeling method that is also efficient is required to predict the seismic response of structures built with ABC technologies.

Research on analytical models related to structures incorporating PT elements started as early as the 1990s. PRESSS (Precast Seismic Structural System) started a program in 1990 consisting of several studies over a decade, including testing a five-story precast, post-tensioned frame under simulated seismic conditions (Priestley et al. 1999). Most numerical modeling techniques were extensively developed in the

past two decades to model the response of precast post-tensioned columns, including 2-dimensional finite element (2D-FEM), 3-dimensional finite element (3D-FEM), and macro-models (multi-spring models). Hewes and Priestley (2002) established a simplified analytical three-stage model to predict the backbone curve of a column under cyclic loads. Kwan and Billington (2003a, 2003b) developed a 2D finite element model to simulate the behavior of unbonded post-tensioned substructure systems and studied model behavior for single-column piers and two-column bents under monotonic, cyclic, and seismic loads. Palermo et al. (2007) used section analysis concepts and lumped plasticity models to duplicate the cyclic behavior of post-tensioned columns with satisfactory accuracy and reliability compared with experimental results. Ou et al. (2007) develop a simplified 3D analytical model for static pushover analysis of segmental precast unbonded post-tensioned columns using ABAQUS, which could predict the behavior of the experiment with high accuracy.

Marriott et al. (2009) developed and tested the efficiency of macro-models (multi-spring model) based on a lumped plasticity model and found excellent agreement between global and local responses. Many researchers have developed analytical models of segmental precast systems for single column piers and found good coherence between analytical and experimental findings for monotonic pushover and cyclic analysis (ElGawady et al. 2010; Chou et al. 2013; Bu et al. 2016a, 2016b). Yamashita and Sanders (2009) carried out a shake table experiment and numerical modeling of a 1/4th scale hollow precast segmental column with unbonded prestressed bars (Yamashita and Sanders 2009). Han et al. (2019) performed analytical finite element modeling of a two-column post-tensioned bridge bent and a hybrid bridge bent, accurately predicting the re-centering and energy dissipating behavior (Han et al. 2019). In most of the experimental and analytical findings, damage is primarily concentrated in the joint region, and the vertical load-carrying members, such as columns of the bridge bent, are damaged. After a large earthquake, severe damage or collapse of poorly designed monolithic bridge bents is high. With the correct design procedures for bridge bents built with ABC technologies, damage in the joints or columns can be reduced or eliminated (Khan 2014).

BRBs have been extensively used as energy dissipating devices in steel buildings (Xie 2005). Many researchers have modeled BRBs in Finite Element Model (FEM) software and OpenSees (McKenna et al. 2014) with excellent matching (Hoveidae and Rafezy 2012; Upadhyay et al. 2019; Dong et al. 2021). Researchers have also used BRBs as a means of retrofit in bridge bents using analytical models and found that BRBs improve the seismic performance of bridges under serviceability and ultimate limit states by decreasing drift demand in the bents and by reducing the steel and concrete strains of the original RC columns (Wang et al. 2016; Upadhyay et al. 2019). Analytical modeling of a BRB in a deficient monolithic reinforced concrete bridge bent has been carried out (Bazaez and Dusicka 2018). Analytical findings have shown that when BRBs are used in frames, performance has been superior by significantly increasing the lateral strength and energy dissipating ability of the system. Even though many researchers have correctly modeled BRBs using numerical techniques, numerical modeling of a BRB in a post-tensioned bridge bent has not been performed. This report first describes the methodology and procedure for a numerical model of a post-tensioned bridge bent, which is then taken as the basis for a numerical model of a PT-BRB Bent. This report describes the development of the analytical model to predict the quasi-static cyclic behavior of a PT-BRB Bent using OpenSees (McKenna et al. 2014) and compares the numerical results with experimental findings. This model is then expanded to a three-column bridge bent, which was previously tested under cyclic loads.

5.2 Analytical Study and Objective

The objective of the computational study was to create a predictive modeling approach for the correct simulation of a post-tensioned bridge bent with a BRB. Non-linear analysis has become a tool for designing and evaluating the seismic performance of structures. In an actual earthquake, non-linear material behavior can occur in a cross-sectional element of the structural component, which can be

approximately modeled using distributed plasticity models or force-based beam-column elements with fiber sections. A discretized finite number of fibers along different cross-sections are assigned with appropriate uniaxial material stress-strain relationships. The global response can be obtained using numerical integration along the element. These findings offer a deeper understanding of the structural response and the failure mechanisms associated with the elements used in the model. A reliable model for designing, analyzing, and predicting the seismic response of a post-tensioned precast and hybrid bridge bent with a BRB is required for numerical modeling. The current state-of-the-art permits simulation of the hysteretic behavior of monolithic bridge bents with acceptable accuracy. There are still significant challenges in analyzing the response of hybrid post-tensioned bridge bents, including the non-linear behavior of reinforced concrete columns, the joint behavior in post-tensioned systems, and the performance of the energy dissipator (BRB).

5.3 Description of Proposed Computational Model

OpenSees, an open-source finite element framework, was used to develop a 2D model (McKenna et al. 2014). The model includes a definition of material models, rocking interfaces between column-to-footing and column-to-cap beam joints, and an unbonded post-tensioning element; in addition, the numerical model includes modeling the BRB in the post-tensioned bent.

5.3.1 Material Models

5.3.1.1 Concrete

The concrete was modeled with two different properties in the column. The core concrete behaves as a stronger material than the cover concrete because the encased core concrete within the confined spiral transverse reinforcement develops higher confining pressure, thus increasing the compressive strength of the core (Mander et al. 1988). The core concrete is confined and is modeled considering the confining pressure provided by the steel spiral. The cover concrete is unconfined and is modeled using the compressive strength from concrete cylinder compression tests. The cover concrete inside the steel collar was modeled as core concrete in the numerical model. *UniaxialMaterial Concrete04* was used to model the cover concrete that can simulate total loss of compressive strength after concrete crushing, which leads to spalling. *UniaxialMaterial Concrete02* was selected to model the core concrete with some residual strength once the crushing limit was reached (Upadhyay et al. 2019). The properties of the concrete used in the OpenSees numerical model are shown in Table 5.1.

Table 5.1 Properties of the *UniaxialMaterial* material models for bent specimens

Material	**Concrete**				**Mild Steel**		**Steel Collar**	
	Confined		**Unconfined**		**Longitudinal bar**			
UniaxialMaterial	***Concrete02***		***Concrete04***		***ReinforcingSteel***		***Steel02***	
	f_c'	13.18 ksi	f_c'	10 ksi	f_{ys}	68 ksi	f_{yp}	50 ksi
	ε_{cc}	0.002	ε_{cc}	0.002	f_{us}	92 ksi	E_{sp}	29000 ksi
	ε_{cu}	0.02	ε_{cu}	0.004	E_s	29000 ksi	B_{sp}	0.005
	f_{cu}	6.57 ksi	E_c	5755 ksi	E_{sh}	4350 ksi	R_{op}	18
	lambda	0.1			e_{sh}	0.004	c_{R1p}	0.925
		No tensile strength*			e_u	0.06	c_{R2p}	0.15

5.3.1.2 Steel Collar and Reinforcing Steel Rebar

The steel collar surrounding the end of the column is modeled as *UniaxialMaterial Steel02* with the properties shown in Table 5.1**.** *UniaxialMaterial Reinforcingsteel* was used to define the stress-strain relationship of mild steel longitudinal reinforcing bars in the column fiber section, which was modeled with isotropic strain hardening defined by the following parameters: yield strength (f_{ys}), ultimate strength (f_{us}), Young's modulus (E_s), tangent at initial strain hardening (E_{sh}), strain corresponding to initial strain hardening (e_{sh}), and strain corresponding to ultimate peak stress (e_u). *UniaxialMaterial Reinforcingsteel* incorporates the buckling simulations that involve a variation on Gomes and Appleton (1997) and Dhakal and Maekawa (2002). The values of amplification factor (β), constant (r), and constant (γ) used for the buckling parameters in the model are equal to 1, 0.4, and 0.5, respectively. The remaining values used for *UniaxialMaterial Reinforcingsteel* are provided in Table 5.1.

5.3.1.3 PT Bars

UniaxialMaterial Steel4 is used to define the tensile stress-strain behavior of threaded PT bars. The value of PT bar yield stress (F_{y-pt}) is 827 MPa (120 ksi), and Young's modulus of elasticity (E_{pt}) is 186 GPa (27,000 ksi). The kinematic properties of the PT bar are as follows: hardening ratio is 0.095, the value that controls the exponential transition from linear elastic to hardening asymptote is taken as 16.0, and constant parameters *r1* and *r2* are taken as 0.9 and 0.1, respectively. The value of ultimate tensile stress was 150 ksi (1034 MPa), and the quantity that controls the exponential transition from kinematic hardening to perfectly plastic asymptote is taken equal to 2.0. The PT bar was modeled without isotropic hardening since the yield surface does not expand proportionally in all directions when yield stress is surpassed. *UniaxialMaterial Steel4* can accommodate the initial value of post-tensioning force. The PT bar fractures at ultimate strength, but the *UniaxialMaterial Steel4* will still function even after the ultimate load is attained. Therefore, the maximum strain value at failure is used in conjunction with *UniaxialMaterial Steel4* as *UniaxialMaterial MinMax* material, and the maximum strain value is set at 0.06. The load history memory option available in *UniaxialMaterial Steel4* is turned on, which records data from preceding load cycles. *UniaxialMaterial Steel4* is used rather than *UniaxialMaterial Steel02* because the available data on preceding cycles are currently used to correct a conventional error in the *UniaxialMaterial Steel02*, which stems from the formulation of the Menegotto-Pinto kinematic hardening model; it overestimates the stress response in the case of small unloading-reloading cycles. This phenomenon should be considered in design since seismic response of structures includes many such small cycles. The error is prevented by constraining the kinematic hardening component of the response to converge to previous load cycles. The monotonic and cyclic stress-strain diagram used for the PT bar is shown in Figure 5.1.

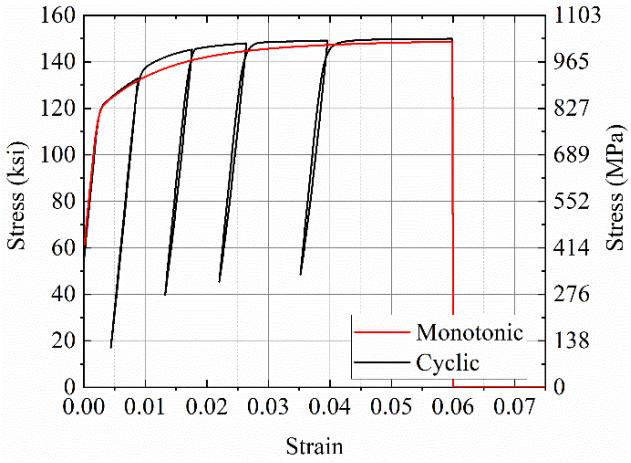

Figure 5.1 Stress-strain diagram of PT bar

5.3.1.3 BRB

In the PT-BRB Bent model, a diagonal BRB was added as an external dissipating element. The BRB was modeled with a *uniaxialMaterial steel02* in parallel with a *uniaxialMaterial pinching4* and *uniaxialMaterial fatigue*, as proposed by Upadhyay et al. (2019), with minor modifications. The *uniaxialMaterial pinching4* is used for reproducing the BRB compressive strength, which is higher than the tensile strength. The BRB is integrated with a fatigue material as the steel core; the steel core fractures in low-cycle fatigue due to successive bending and re-straightening of the steel core. The *uniaxialMaterial fatigue* was also incorporated into the *uniaxialMaterial steel2* to account for low-cycle fatigue.

The parameters used for BRB modeling were compared with experimental results performed on four similar BRBs showing excellent matching. Tables A1-A3 in the Appendix list the values of the parameters used for *uniaxialMaterial steel2*, *uniaxialMaterial pinching4*, and *uniaxialMaterial fatigue* to model the BRB. For one of the BRB tests, the experimental and numerical comparison is shown in Figure 5.2. The strength of the BRB matched well in both the tension and compression region, as shown in Figure 5.2 (Upadhyay and Pantelides 2019). The hysteretic energy (HE) per cycle in Figure 5.2 is normalized by the product of the experimental yield force times the experimental yield displacement. The error in the hysteretic energy dissipation is within 10%. The BRB yielded and fractured in the same cycle in the analytical model as in the experiment for all four specimens.

5.3.2 Analytical Model Assumptions

Certain assumptions are made to minimize the computational time to run the model and the errors associated with the experiment. These assumptions ease the complexity involved in the model to some extent. The foundations are assumed as fixed to the ground. The interaction between the columns, PT bars, and other structural members along the out-of-plane movement is not within the scope of the analytical model, and out-of-plane effects are ignored. The cap beam is assumed to behave as a highly elastic or rigid element.

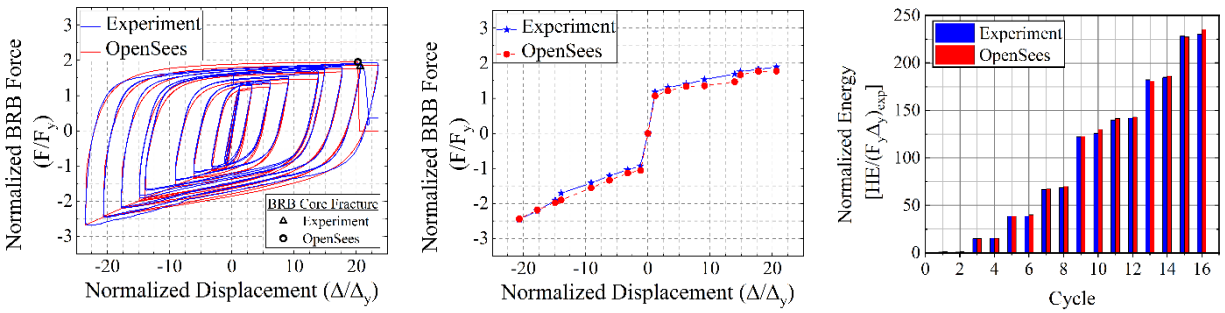

Figure 5.2 Model and experimental matching of the BRB

Experimental detailing is simplified: the deformation of the plates underneath the rollers at the axial roller assembly and the plates and channels connecting the hydraulic actuator to the cap beam are not considered. The frictional contact between the roller and channel section in the roller assembly provided for applying the axial load in the system is taken as a minimal numerical value for maintaining the stability of the model. The response of the compression-only contact elements is assumed to be bi-linear and inelastic to ensure that the lateral strength of the bent is not overestimated. Only a minimal value is considered for the shear action/shear slip at the joint interface occurring due to the force provided by the PT bars and axial rods. The PT bars behave as a straight element and buckling of the PT bars is ignored. The post-tensioning losses due to anchor seating are also neglected. The P-Δ moments are counterbalanced, and consequently, P-Δ effects are not considered for the computational model validation process. Torsional and out-of-plane deformations of gusset assemblies and BRB are not modeled since they were constrained in the experiment.

5.3.3 Model Layout of Test Specimen

The proposed computational model was developed in the OpenSees framework; it is a 2D model which uses beam-column elements with distributed plasticity along the columns. Rocking mechanisms are prevalent at the joint. The footings were restrained against sliding and rotation and were modeled as fixed elements.

Unlike monolithic joints, rocking is prevalent in joints where two separate precast concrete elements are joined together using external PT bars. To obtain the exact response of the specimen, rocking was modeled through a set of compression-only two-node contact zero-length vertical elements, spread over the top and bottom joint interface in parallel; all springs were rigidly connected to adjacent nodes (Spieth et al. 2004; Palermo et al. 2005; Marriott et al. 2009). This method, known as the multi-spring model approach, has the greatest potential to model a post-tensioned system in terms of accuracy versus computational effort (Marriott et al. 2009). A critical part of modeling the contact surface is assigning contact material properties; different properties were assigned to compression-only springs used at the rocking interface at the top and bottom joint interfaces to account for different interactions. Contact surfaces were simulated using *uniaxialMaterial ElasticPPGap*, capable of only being subjected to compression forces with no damage parameter; parameters used are modulus of elasticity of contact springs (E_{sp}) and yield stress of springs (f_{sp}). The value of modulus of elasticity of the spring in the other two directions is negligible when compared with the axial spring. However, a small value was employed for computational stability in the two directions.

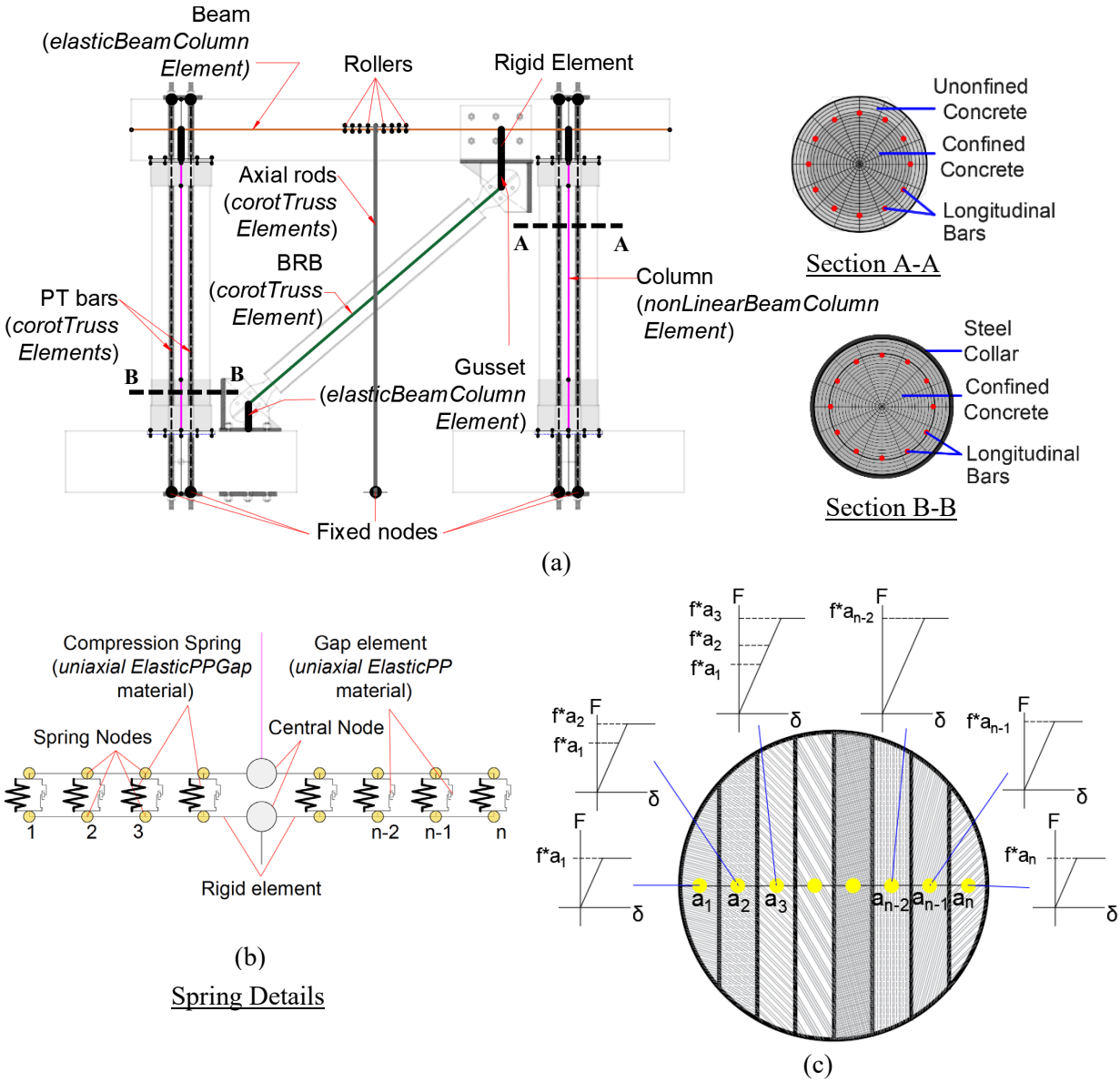

Figure 5.3 PT-BRB Bent numerical analysis model: (a) schematic layout; (b) spring details; (c) force-displacement relationship for compression springs

The first step in modeling the contact surface involves dividing the column diameter into an even number of segments (n), as shown in Figure 5.3. Each segment is equivalent to one spring, and all springs are distributed over the joint. The areas inside the chord length of the circular segment are used to generate the bilinear force-displacement curve for that spring, as shown in Figure 5.3(c). Each segmental area (a_i) is multiplied by the compressive stress (f) to get the force-displacement relationship for each spring. The value of f for the top contact surface is the concrete compressive stress, whereas f for the bottom contact surface is the PU plate compressive stress, placed at the column-to-footing interface. Since this is a 2-D model, the approximation resembles the experimental configuration; the concrete segment with the smallest area at the extreme fiber from the center will first reach its compressive strength and experience damage due to crushing earlier than the inner concrete fibers. The modulus of elasticity is the same for all concrete segments. The column is confined with a steel collar at the top joint, and thus compression springs at the top had the properties of high-strength concrete with a tangent modulus of 6,000 ksi (41,369

MPa). The compression springs at the bottom rocking interface have the properties of the PU plate with a tangent modulus of 333 ksi (2,296 MPa) that was obtained experimentally.

At the top and bottom joint interfaces, in order to simulate the compression springs, two overlapping nodes were defined with the same coordinates connected together by *ZeroLength elements,* as shown in Figure 5.4. At the column-to-footing interface, all the nodes of the lower layer were fixed, whereas the upper layer nodes were free to elongate vertically, simulating column uplift, as shown in Figure 5.4(a). However, both spring layers were free to move vertically at the column-to-cap beam interface, as shown in Figure 5.4(b). Since the springs had zero tensile resistance, they were designed to remain in compression during uplift of the rocking plane. The nodes in each layer were rigidly connected to the adjacent side nodes, ultimately connected to the central nodes to form the rigid horizontal plane shown in Figure 5.4. The column, which was modeled as a *nonlinearBeamColumn element*, was connected to the central nodes.

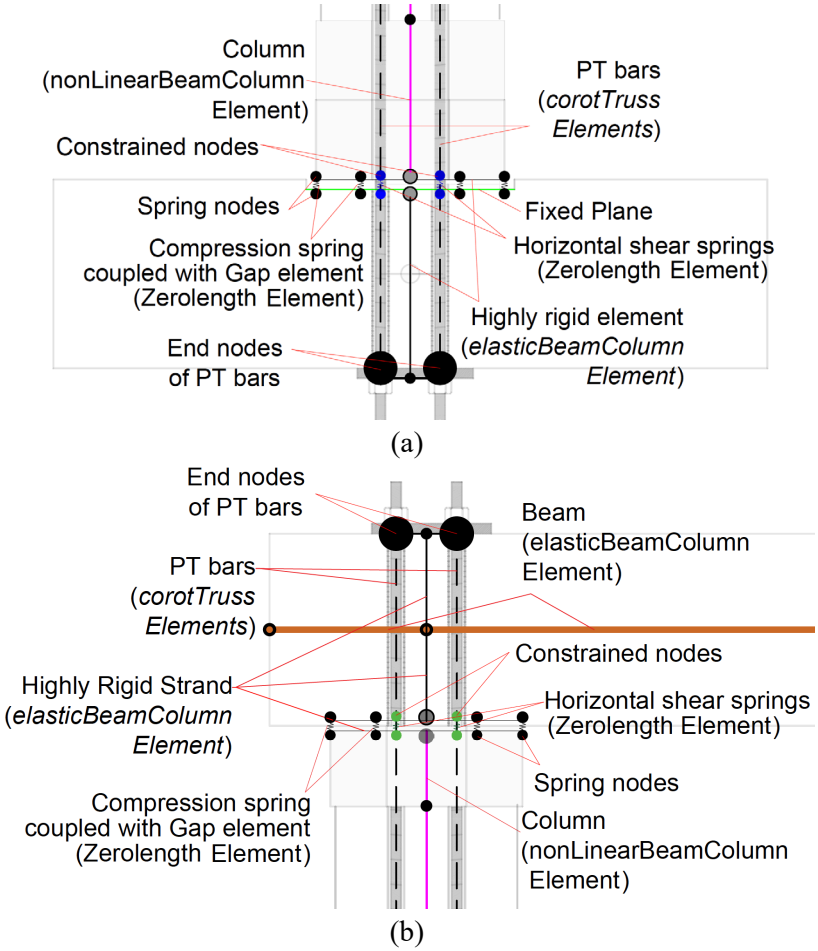

Figure 5.4 Schematic layout of arrangement of elements: (a) bottom joint; (b) top joint

The *nonlinearBeamColumn element*, based on iterative force-based formulation, was employed to simulate the octagonal precast concrete column. For simplicity, an equivalent circular section was used to model the octagonal shape of the column. Two different sections of the column are considered: (a) the bottom and top segment, where the column is protected by a steel collar, and (b) the middle segment. The end sections are modeled with confined concrete and steel collar (section B-B), and the middle section is modeled with core concrete and unconfined concrete at the perimeter (section A-A) in Figure 5.3(a). There were 16 circumferential and 16 radial subdivisions for the confined concrete core and 4

circumferential and 16 radial subdivisions for the unconfined cover concrete. Longitudinal mild steel bars were included within the column using the *Layer* command.

When the strain-softening sections of the structural members are used in modeling software, the response of the element changes depending upon the number of integration points (Coleman and Spacone 2001; Scott and Fenves 2006). Since deformations are only localized at the integration points, this method suffers from loss of objectivity; the response differs as the integration weight of a single integration point shifts when changing the total number of integration points used in any element (Ameli and Pantelides 2017). Since damage mainly occurs at either end of the column in this type of rocking structure, only two integration points are incorporated along the column element length. Similarly, damage was only concentrated at the ends of the columns in the experiment; hence, the *nonlinearBeamColumn element* was used with two integration points.

To incorporate the gap between PT bars and duct, i.e., the unbonded nature of the PT bar, all rocking nodes were coupled with gap elements modeled with the *uniaxialMaterial elasticPP*, as shown in Figure 5.3(b). The value of deformation at which the material reaches the plastic state in tension and compression is assumed as 2.0 mm (0.08 in.), and the tangent modulus is taken as a small value (1x10E-9) for maintaining model stability. Unbonded PT bars moved freely relative to the surrounding concrete, resulting in uniform distribution of bar strains and eliminating tensile stress transfer to the concrete. *CorotTruss element*, which considers non-linear elemental geometry, was used to model the PT bar since, when the column uplifts, the PT bar would be inclined by an amount approximately equal to the base rotation. For this reason, a non-linear transformation is chosen for the post-tensioning bars; thus, the non-linear effects associated with inclination of the PT truss element were included. Moreover, a horizontal shear spring between the constrained nodes was created using the *ZeroLength element* at the location where the PT bars cross the joint interface to simulate the behavior of the PT bars at the interface region, as shown in Figure 5.4, which was modeled with *uniaxialMaterial ENT*. The tangent modulus for these springs was assumed to range from 30 ksi (207 MPa) to 60 ksi (414 MPa).

The central node at the upper layer of the compression spring was connected to the cap beam using a rigid element, as shown in Figure 5.4(b). The PT bars were rigidly connected using the *elasticBeamColumn element* to the center node of the beam, whereas the lower node of the PT bars was restrained, as shown in Figure 5.4. The initial value of post-tensioning stress used in both experiments was incorporated in the *uniaxialMaterial steel4*. The cap beam was rigidly built and behaved elastically, and the *elasticBeamColumn element* was used to represent it, as shown in Figure 5.3.

To simulate the rollers placed between the cap beam and the hydraulic jack connected to the cap beam, which were part of the mechanism used to apply the axial load (Thapa and Pantelides 2021), the horizontal rigid layer of the highly elastic element was connected with eight nodes right above the center of the cap-beam, as shown in Figure 5.3(a). Eight compression-only springs were connected with *ZeroLength elements* between the rigid layer and cap beam with negligible stiffness in the horizontal and rotational directions. The axial load was applied at the midspan of the cap beam with the two *CorotTruss elements*, extending from the center of the rigid layer to the fixed node at the bottom. A schematic layout of the model can be seen in Figure 5.3(a).

A BRB is incorporated into the model as a diagonal energy-dissipating element, as shown in Figure 5.3(a). The gusset plate is modeled as elastic material using *ElasticBeamColumn element* with the properties of the gusset plate used in the experiment. As Figure 5.3(a) shows, one end of the BRB was connected to the footing and the other end was connected to the cap beam. The lower gusset plate is attached to the midpoint of the four bolt holes and extended vertically downward to the surface of the footing, which is fixed to the ground. The upper gusset plate is attached to the midpoint of the four bolt holes and extended vertically upward to be joined with the rigid cap beam. The BRB is modeled as a *CorotTruss element* with a steel core cross-sectional area of 581 mm^2 (0.9 $in.^2$). The parameters used for modeling the BRB in the PT-BRB Bent are within the range of values listed in Tables A1-A3 in the Appendix.

5.4 Specimen Model Validation

The proposed modeling strategy is based on the transformation of the model for the unbonded post-tensioned precast two-column bridge bent with BRB into an idealized equivalent bridge bent, which could replicate acceptable global and local performance. Similar to the experimental procedure, the analytical model was subjected to a displacement-controlled lateral loading protocol, which included symmetric double cycles of increasing amplitude with a peak drift ratio of 6.0%. The cyclic analysis of the PT-BRB Bent was terminated in the numerical model as soon as the BRB core fractured.

An iterative validation process was established for the proposed numerical model to match within satisfactory accuracy under quasi-static cyclic loading. In order to achieve the desired level of accuracy, two benchmarks were incorporated; the first is validation of the hysteretic performance, which refers to the overall response of the lateral force and displacement of the bridge bent. This validation is true when strength and stiffness are within 15% of the experimental value. A quantitative measure for this acceptance criterion is to compare the peak lateral force of the model with the hysteretic energy and loading-unloading stiffness of the test results for every drift ratio. The second criterion is the local response validation of member performance, which is validation of the axial deformation of the BRB in addition to the PT bar forces under cyclic loads; thus, yielding and fracture of the BRB are the main criteria for validating the PT-BRB Bent model in addition to PT bar force matching.

The bent is modeled by defining the sectional properties close to the experimental values. Initially, 10 compression springs at one joint interface to simulate the rocking column having the properties of polyurethane at the bottom and properties of concrete at the top were selected. The properties of gap element and horizontal spring are then defined; these values are modified until there is a close match between analytical and experimental results. Iteration was continued until global and local response of the computational model and the experiment were both within a 15% error. Modeling parameters of the BRB, as specified in Table A1-A3, were modified to get a similar response to that of the experiment. The flowchart of the model validation process is shown in Figure 5.5. The global and local response from the numerical model was compared with the experimental results regarding hysteretic response, hysteretic energy, stiffness, and PT bar cyclic response. The OpenSees model was able to capture local and global responses successfully.

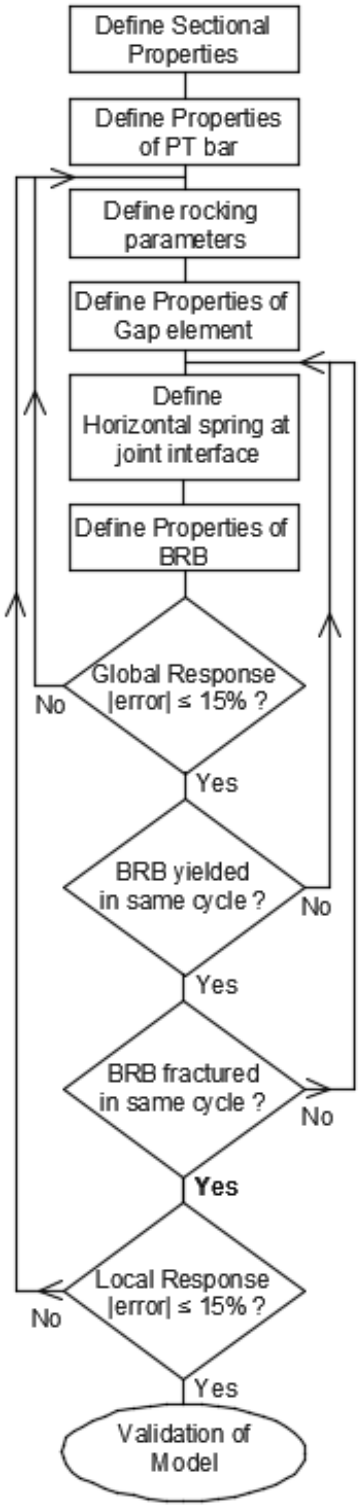

Figure 5.5 Model validation process

5.5 Numerical Model vs Experiment Model

5.5.1 Hysteretic Response

The hysteretic response results of the numerical model were compared to experimental results; an acceptable match was reached in terms of global response. The model predicted the backbone curve very well, capturing important characteristics, including peak lateral force, as shown in Figure 5.6. The loading and unloading curves were matched at every drift cycle with acceptable accuracy. The experimental and analytical backbone curves for the test are shown in Figure 5.6. The local response defined as the response of the PT bars and the response of the BRB were predicted well. The model also predicted that the concrete columns would not be damaged throughout the test, which agrees with the experimental results.

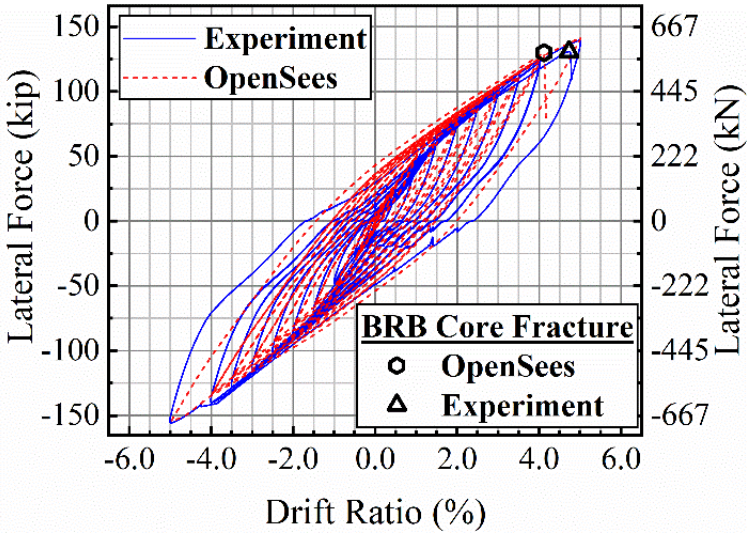

Figure 5.6 Numerical and experimental comparison of hysteresis curve

5.5.2 Hysteretic Energy

The hysteretic energy from the numerical model was compared with the experimental results at each drift ratio; Figure 5.7 shows that the model and experiment are in good agreement. The maximum error of 5.0% in hysteretic energy between analytical model and experimental result at each drift ratio confirms that the numerical model behaves similarly to the experiment.

5.5.3 Stiffness

The stiffness of the bent at every peak drift level from the numerical model and the experiment is plotted in Figure 5.8. The stiffness from the analytical model matches the experiment to an acceptable level. The maximum error in stiffness between analytical model and experimental result at each drift ratio was 10.0%, and this occurs early in the first few cycles.

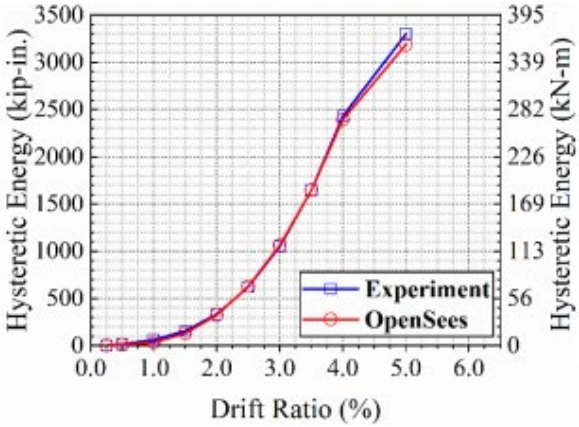

Figure 5.7 Numerical and experimental comparison of hysteretic energy

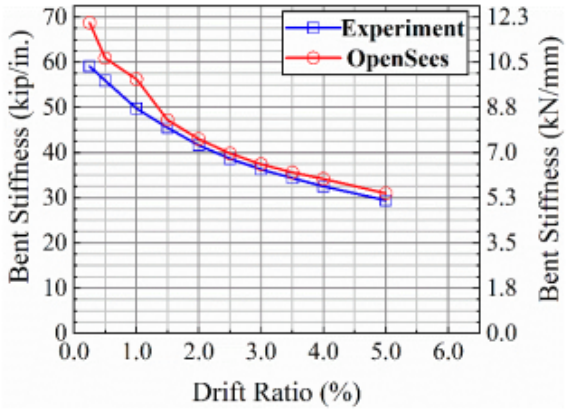

Figure 5.8 Analytical and experimental comparison of bent stiffness

5.5.4 Post-tensioning Forces

Figure 5.9 shows the post-tensioning forces in the numerical model versus the experiment for the PT-BRB Bent. The variability of column post-tensioning forces due to the presence of the BRB is captured by the numerical model. The maximum value of the post-tensioning force was within 10.0%; the numerical model was able to capture the losses at each drift ratio except at small drift levels.

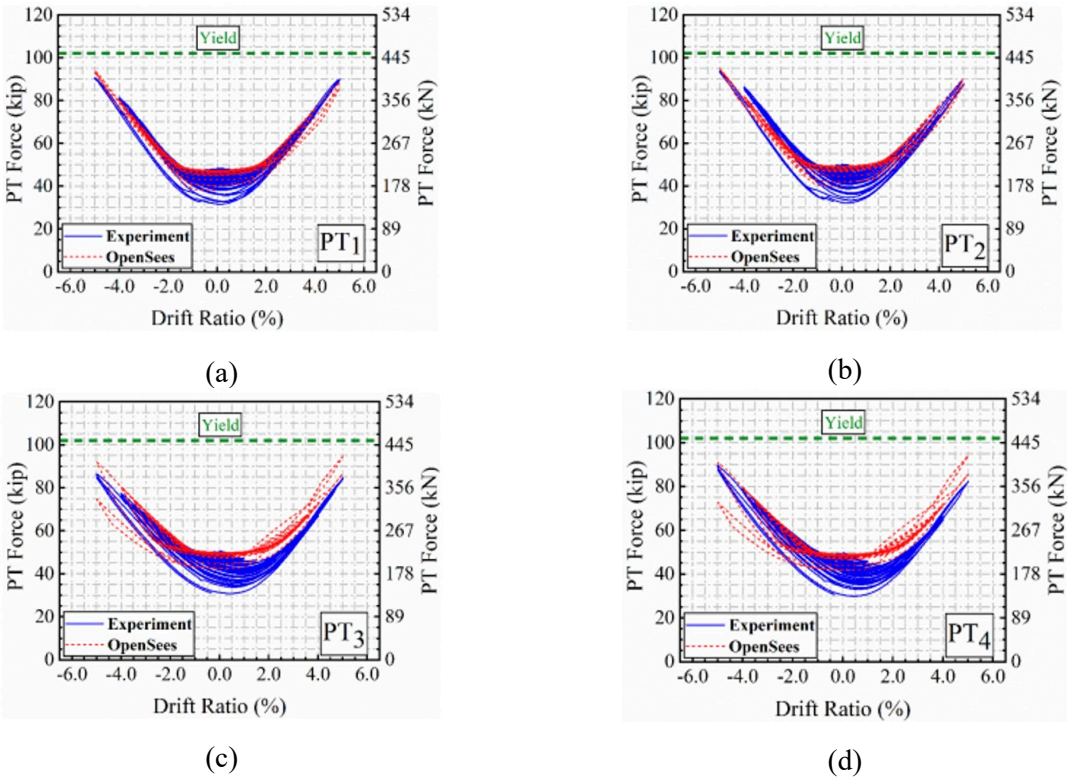

Figure 5.9 Numerical and experimental comparison of post-tensioning forces

5.5.5 BRB Response

The axial deformation of the BRB from the experiment and from the model shows an almost perfect match, as seen in Figure 5.10.

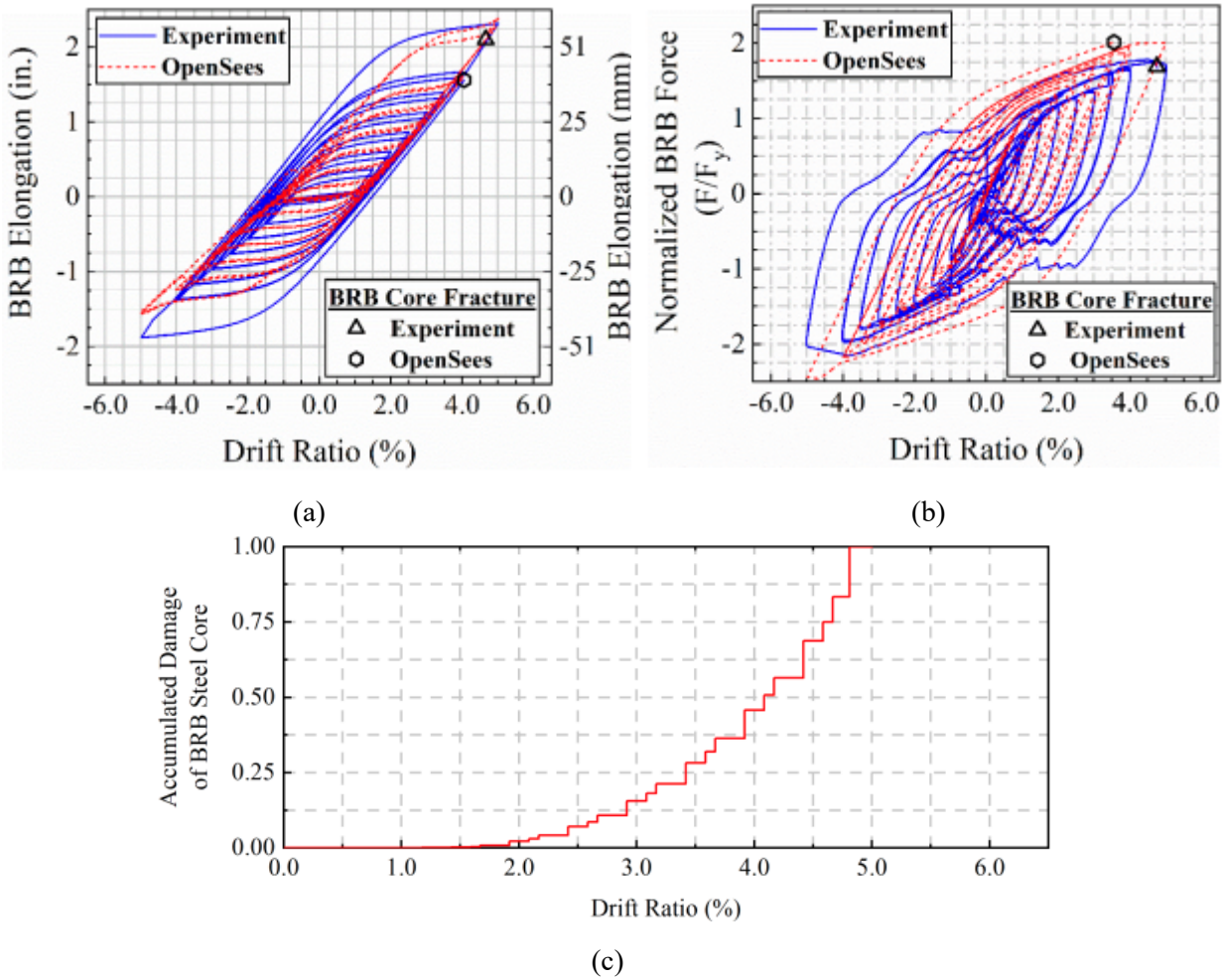

Figure 5.10 Numerical and experimental comparison of BRB response: (a) BRB axial strain; (b) BRB force comparison; (c) fatigue loss of the BRB at every cycle from OpenSees

Two LVDTs were used to measure the axial deformation of the BRB at each end in the experiment, and this established a reasonable estimate of BRB elongation and BRB strain. The BRB elongation shows almost a perfect match between experimental and numerical model, as seen in Figure 5.10(a). However, the exact level of axial force in the BRB could not be measured directly in terms of axial tension or compression due to the absence of a load cell. From the numerical analysis, the force versus deformation response of the BRB during the tension and compression cycles is shown in the Figure 5.10(b); the calculated axial force in the BRB and the numerical model show an acceptable match.

Low-cycle fatigue was incorporated in the numerical model; *UniaxialMaterial Fatigue* incorporates damage as soon as the material yields. Fatigue damage of the BRB steel core was included and is shown in Figure 5.10(c); fatigue damage increased after the 1.5% drift ratio due to yielding of the steel core, which agrees with the experimental findings. The steel core fractures when fatigue damage reaches 1.0,

according to the definition of material fatigue. The BRB steel core fractured during the same cycle of the 5.0% drift ratio in the experimental and the numerical model.

5.6 Application of Model to Actual Bridge

5.6.1 Design and Numerical Model of Bridge Bent

The three-column bridge bent tested in situ by Pantelides et al. (1999, 2003, 2004, 2007, 2012) was taken as a base model for numerical analysis using OpenSees. The dimension of the bent, including pile caps and the properties of the material used in the numerical model of the bent, are outlined in Upadhyay et al. (2019) and Wu and Pantelides (2019). A schematic of the numerical model of post-tensioned bent with BRB is created in OpenSees, as shown in Figure 5.11. *UniaxialMaterial Concrete02* was used to model the concrete for the column; longitudinal steel reinforcement was modeled using *UniaxialMaterial Reinforcingsteel02*, available in OpenSees, to consider both tension and compression behavior. The total post-tensioning bar area needed for the bent to prevent yielding of the PT bars at the target drift ratio was checked before designing the number of PT bars in the column. A $1\frac{1}{4}$in. (32M) diameter high strength alloy bar with an area of 1.25 in.^{2} (807 mm^2) is used. Four PT bars are used in each column, which run from the top of the cap-beam to the base of footing, as shown in Figure 5.11. The total area of PT bar used satisfies the area requirement needed for prevention of yielding of PT bars at the target drift ratio. The PT bar reinforcing ratio for each column is 0.4%. The value of the initial post-tensioning force in each PT bar is assumed as 90 kip (400 kN); each PT bar is modeled with *UniaxialMaterial steel4* with the same parameters used in the experiment.

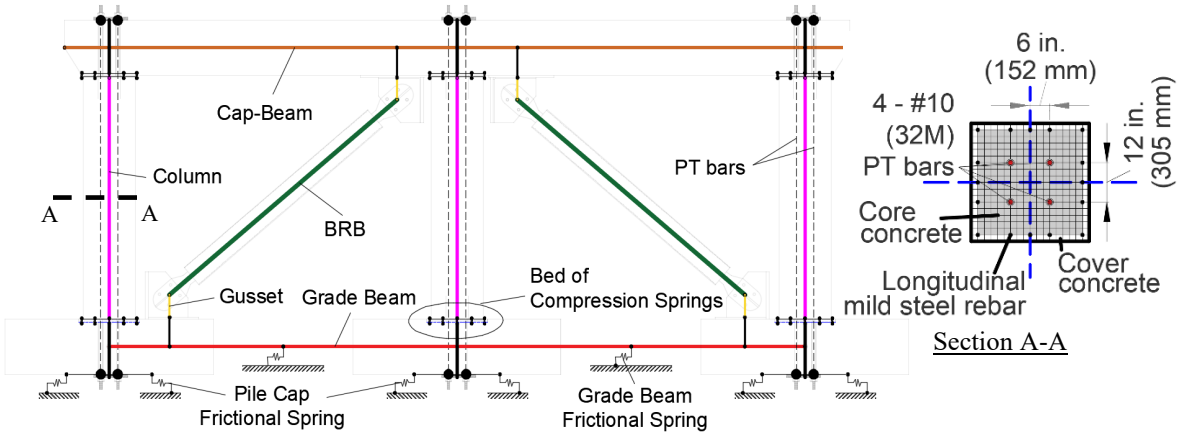

Figure 5.11 Model layout of three bent specimen: post-tensioned bridge bent with BRB

The bed of compression springs is modeled with the properties of concrete; horizontal shear springs are incorporated at the location where the PT bars cross both the top and bottom interface joints. The column-cap beam and grade beam are modeled as rigid beams. Since the seismic response of pile-supported structures depends on accurate numerical modeling of soil-pile-structure interaction, the soil was modeled with equivalent frictional springs to represent the soil-pile cap and equivalent frictional springs to represent the soil-pile cap soil-grade beam behavior (Wu and Pantelides 2019). As the CIP model has been validated with and without the soil interaction using the pushover curve, a post-tensioned bridge bent was numerically modeled with disjointed joints coupled by compression rocking springs and four PT bars with the same material properties for further analysis (Wu and Pantelides 2019; Upadhyay et. al 2019).

Two diagonal BRBs are configured in the bridge bent in a chevron arrangement, as shown in Figure 5.11. The BRB is designed to satisfy the four criteria discussed earlier. Two BRBs with a yield stress of 44.5 ksi (307 MPa) are used in the bent with a core area of a single BRB equal to 1.35 in^2 (871 mm^2); this results in a yield strength capacity of 60 kip (267 kN) for each BRB. BRBs are rigidly connected to the grade beam and cap-beam with gusset plates, which are modeled as *elasticBeamColumn element*. The BRB is modeled with the same material properties used for the experiment.

5.6.2 Design Details of Earthquake Analysis

The structural performance of the bridge bent was evaluated based on two hazard intensity levels that included DBE, i.e., 10% probability of exceedance in 50 years, and MCE, i.e., a 2% probability of exceedance in 50 years. Using the United States Geological Survey (USGS 2020) design maps tool, the design response spectrum was obtained for a downtown location of Salt Lake City, Utah. Site class D was assumed as the site; the soil can be categorized as soft to stiff clay with maximum and minimum shear wave velocities of 310 m/s (1,017 ft/s) and 100 m/s (328 ft/s), respectively. Since the bridge site is approximately 12 km (39,370 ft) from the Wasatch fault in Salt Lake City, far-field ground motions and near-field pulse-type ground motions are considered in the study.

5.6.3 Characterization of Damage/Limit States

In order to evaluate the performance of structures, several damage limit states (DS) have been specified, which are related to drift ratio limits (Dutta and Mander 1998; Mander et al. 2007; Billah et al. 2012). Three DS limit states based on the qualitative damage categories of slight, moderate, and extensive damage obtained from HAZUS (FEMA 2020) were implemented for the seismic bridge assessment based on a High-Code seismic design level, which applies to code lateral force design requirements for Seismic Zone 4.

5.6.4 Nonlinear Time History Analysis

The seismic performance of the post-tensioned bridge bent with BRBs was investigated using 22 far-field ground motions and 14 near-field ground motions using the Pacific Earthquake Engineering Research Center (PEER 2021) strong motion database. Acceleration records for reverse/oblique and strike-slip fault type with the shear wave velocity of the site were generated. Details of the ground motions in terms of the magnitude, name, station, occurrence year, recording station, epicentral distance, and peak ground acceleration (PGA) are shown in Table A4-A5 for both sets of earthquakes. For the nonlinear THA, PEER NGA West2 ground motion prediction attenuation relationship tool was used to estimate the conditional mean spectrum assuming the site location was in downtown Salt Lake City. The resulting conditional mean spectrum was utilized as the target spectrum. Since scaling GMs using spectral acceleration results in minimum dispersion in the output parameter values (Baker and Cornell 2006; Zareian et al. 2006), the spectral accelerations were matched to the target spectrum in SeismoMatch using a multi-step matching technique (Seismosoft 2022). The bridge bent was analyzed using scaled ground motions. Figure 5.12 shows the DBE level scaled response spectrum with 5.0% damping ratio for both near-field and far-field earthquakes.

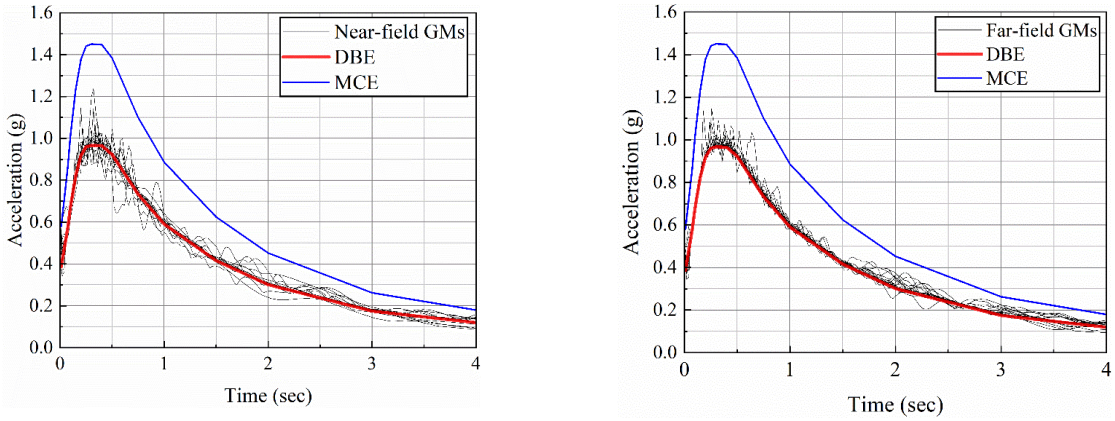

(a) (b)

Figure 5.12 DBE level scaled response spectrum: (a) near-field ground motion; (b) far-field ground motions

The responses of the post-tensioned bridge bent with BRB under the MCE level for both near-field and far-field earthquakes under GM4, 1987 Superstition Hills-02 earthquake recorded from Parachute Test Site and GM4, 1999 Hector Mine earthquake recorded from Hector station, respectively, are shown in Figure 5.13. The comparison of the responses, shown in Table 5.2, proves that when BRBs are added to the post-tensioned bridge bent, the seismic response is drastically reduced. Moreover, base shear force was slightly increased due to the increased structural stiffness in the case of a post-tensioned bridge bent with BRB.

Table 5.2 Seismic response comparison of post-tensioned bridge bent with BRB under near-field ground motion (GM N4) and far-field ground motion (GM F4)

Response	Near-field (GM N4)	Far-field (GM F4)
Maximum base shear (kip)	298	287
Maximum drift ratio (%)	1.60	1.58
Residual drift (%)	0.13	0.12
Maximum compressive strain (microstrain)	800	700
Maximum PT bar force (% of yield)	67	66

Note: 1 kip = 4.4482 kN

The seismic performance of the post-tensioned bridge bent and post-tensioned bridge bent with BRB is described statistically using cumulative distribution functions (CDFs). CDF for the PT-BRB Bent was created for several output parameters based on a lognormal distribution. The median parameter ($\bar{x}$) and dispersion parameter (β) of variable x was calculated using Eqs. (5.1) and (5.2).

$$x = \frac{1}{n}\sum_{i=1}^{n} x^i \tag{5.1}$$

$$\beta = \sigma_{\ln x} = \sqrt{\frac{(lnx_i - \mu_{\ln x})^2}{n-1}} \tag{5.2}$$

where n is the total number of data points, and $\sigma_{\ln x}$ is the mean of the natural logarithm of variable x.

CDF is calculated for maximum drift ratio, residual drift ratio, and maximum post-tensioning force for near-field and far-field earthquakes. Figure 5.14 shows the seismic evaluation of the bent under DBE and MCE level ground motions. CDF characterizes the predicted structural performance under both sets of ground motions and describes the cumulative probability of a structure that can reach out to a certain performance state; this provides a useful way to obtain the seismic performance of a post-tensioned bridge bent with BRB statistically. The maximum drift ratio of the post-tensioned bent with BRB will always be less than 2.0% and 2.5% for both near-field and far-field earthquakes, respectively, as shown in Figure 5.14(a). Vision 2000 (1995) recommends the serviceability threshold for residual drift ratio to be below 0.5%. The post-tensioned bridge bent with BRB displays higher recentering capabilities with negligible residual drift under both types of earthquakes, as shown in Figure 5.14(b). Figure 5.14(c) shows a comparison of the CDFs for PT bars under both types of earthquakes; the PT bar in post-tensioned bent with BRB will not yield at an MCE level earthquake. It is understood from the CDF that the post-tensioned bridge bent with BRB displays superior performance.

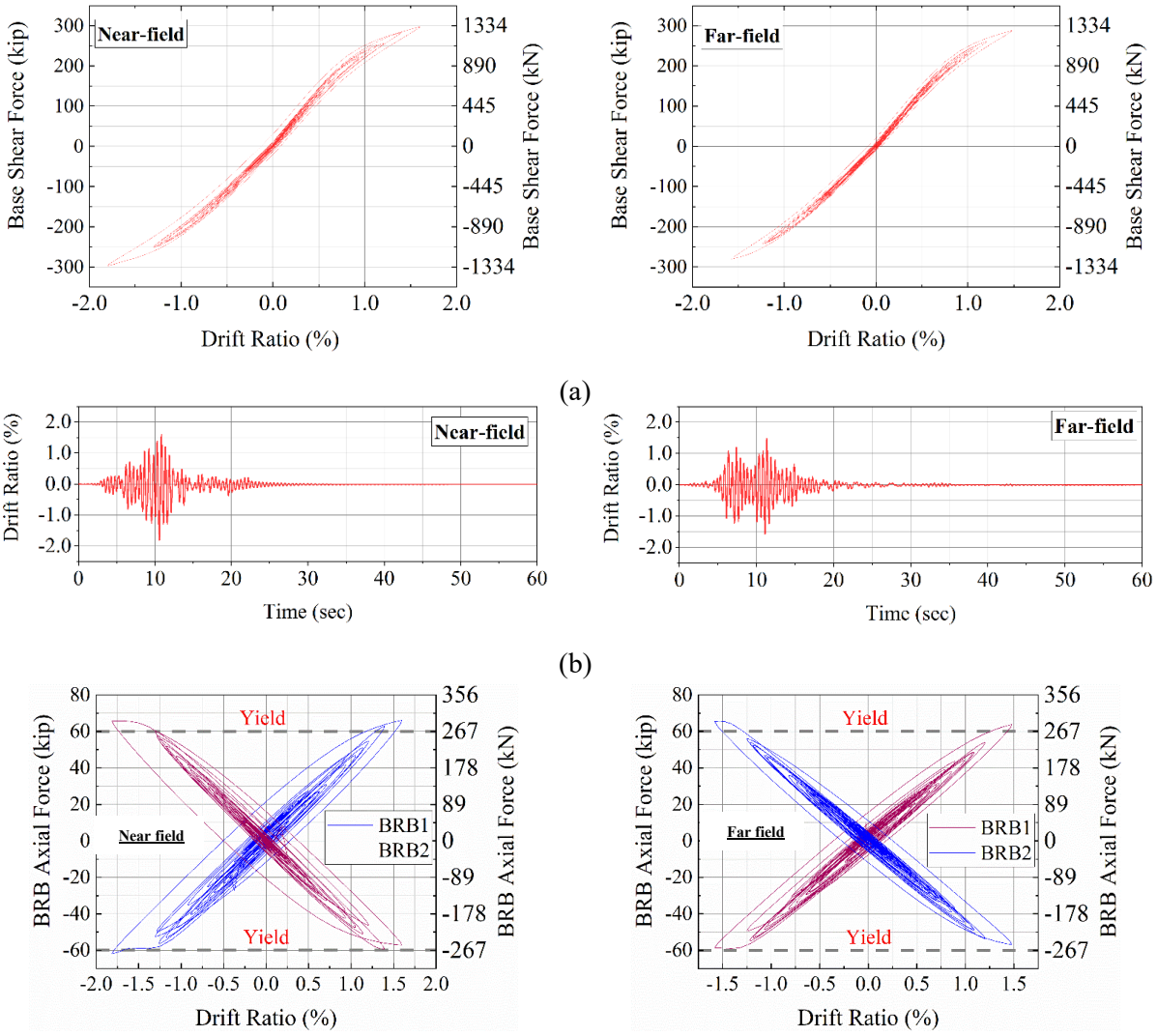

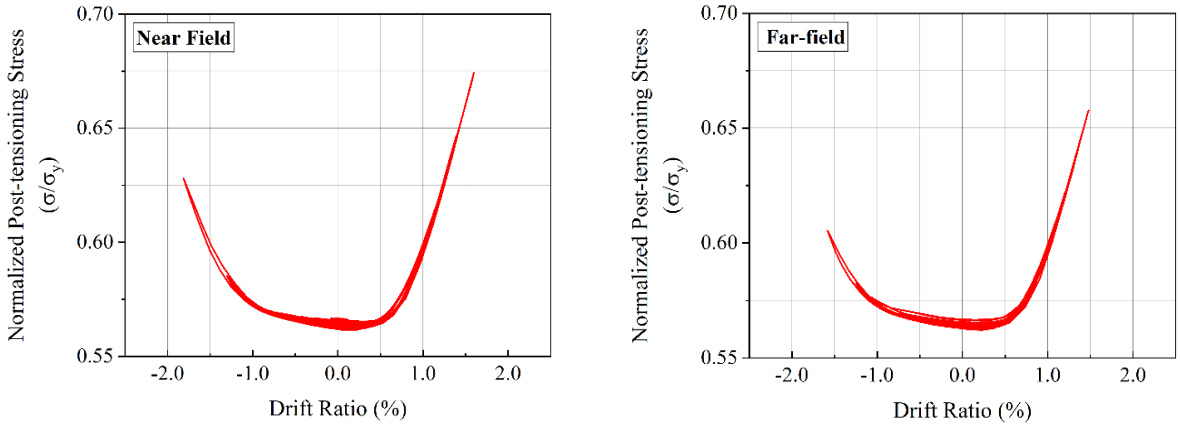

(d)

Figure 5.13 Responses of post-tensioned bridge bent with BRB MCE level GM 4: (a) hysteresis; (b) drift ratio; (c) BRB; (d) post-tensioning stress.

5.6.5 Multiple Stripes Analysis

Structural analyses are performed at a discrete set of intensity measure (IM) levels, at each of which different ground motions are used (Baker 2015). The multiple stripes analysis (MSA) approach is common when using the conditional spectrum or other approach to select GMs representative of a specific site and IM level, because the ground motion target properties change at each IM level and thus the representative ground motions do so as well (Baker 2015). With this approach, the structural analyses are limited up to IM amplitudes where all ground motions cause predefined responses. The ground motions at each IM level that cause a specific response are recorded from the structural analyses results. The appropriate fitting technique for these types of data is maximum likelihood. At each intensity level IM = x_j, the structural analyses produce some number of predefined responses out of a total number of ground motions. Assuming that observation of that particular response from each ground motion is independent of observations from other ground motions, the probability of observing z_j specific response out of n_j ground motions with IM = x_j, is given by the binomial distribution

$$P\left(z_j \text{ specific structural response in } n_j \text{ ground motions}\right) = \binom{n_j}{z_j} p_j^{z_j} (1-p_j)^{n_j - z_j} \tag{5.3}$$

where p_j is the probability that a ground motion with IM = x_j will cause specified response of the structure.

The fragility function that will predict p_j and maximum likelihood identifies the fragility function that gives the highest probability of having observed the specified structural response obtained from structural analysis. When analysis data are obtained at multiple IM levels, we take the product of the binomial probabilities [from Eq. (5.3)] at each IM level to obtain the likelihood for the entire dataset:

$$Likelihood = \prod_{j=1}^{m} \binom{n_j}{z_j} p_j^{z_j} (1-p_j)^{n_j - z_j} \tag{5.4}$$

where m is the number of IM levels and Π is a product over all levels.

We then substitute Eq. (5.4) for p_j, so the fragility parameters are explicit in the likelihood function:

$$Likelihood = \prod_{j=1}^{m} \binom{n_j}{z_j} \emptyset\left(\frac{\ln(x_j/\theta)}{\beta}\right)^{z_j} \left[1 - \emptyset\left(\frac{\ln(x_j/\theta)}{\beta}\right)\right]^{n_j - z_j} \tag{5.5}$$

Estimates of the fragility function parameters are obtained by maximizing this likelihood function. It is equivalent and numerically easier to maximize the logarithm of the likelihood function:

$$\{\hat{\theta}, \hat{\beta}\} = \underset{\theta,\beta}{argmax} \sum_{j=1}^{m} \left\{ \ln\binom{n_j}{z_j} + z_j \ln \emptyset\left(\frac{\ln(x_j/\theta)}{\beta}\right) + (n_j - z_j) \ln\left[1 - \emptyset\left(\frac{\ln(x_j/\theta)}{\beta}\right)\right] \right\} \tag{5.6}$$

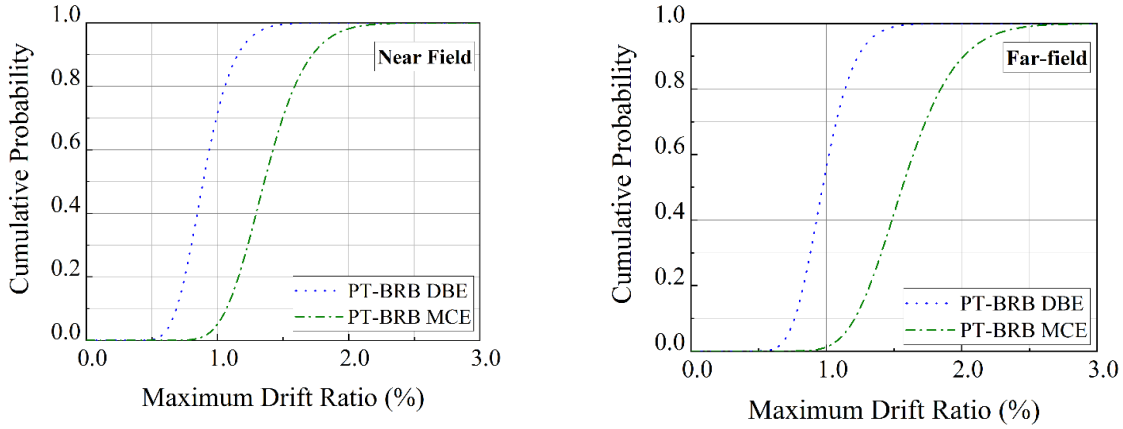

(a)

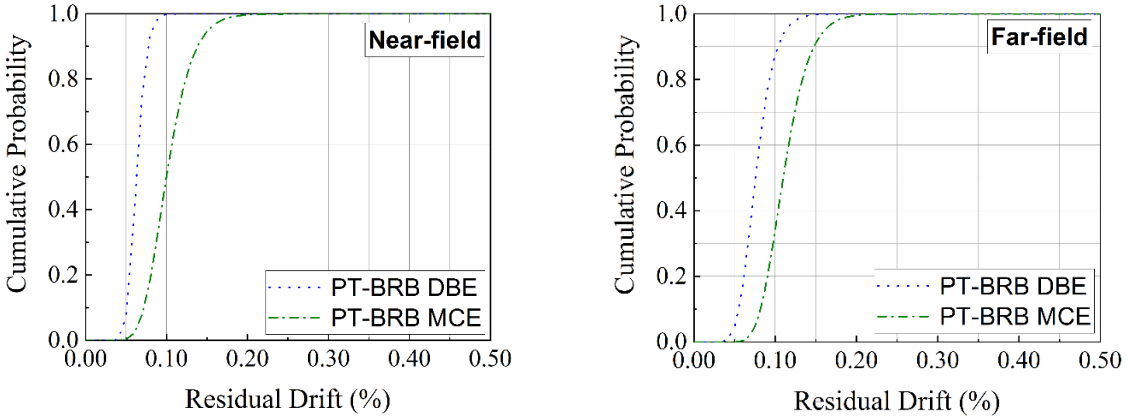

(b)

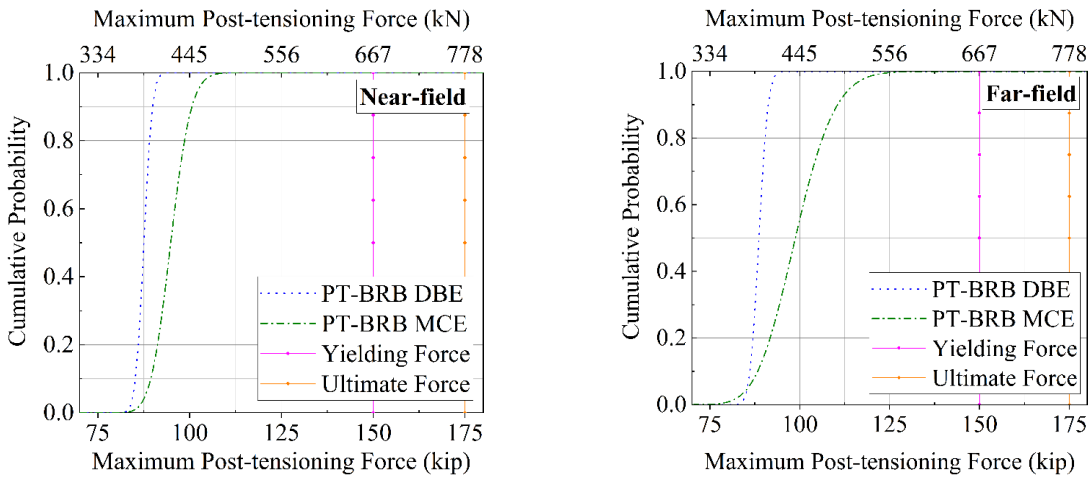

(c)

Figure 5.14 Seismic evaluation of post-tensioned bridge bent and post-tensioned bridge bent with BRB under 14 DBE and MCE level near-field ground motion and 22 DBE and MCE level far-field ground motions: (a) maximum drift ratio; (b) residual drift ratio; (c) maximum post-tensioning force

5.6.6 Seismic Fragility Analysis

In order to perform MSA analysis, the structural response of both bridge bents is obtained for both types of earthquakes up to 6g with an increment of 0.2g. A fragility function is calculated using the MSA approach, with drift ratio being the seismic response parameter and slight, moderate, and extensive damage being the degree of measure. The parameters of fragility curves for the post-tensioned bridge bent with BRBs are shown in Table 5.3.

Table 5.3 Parameters of fragility curves for post-tensioned bridge bent with BRB with respect to spectral acceleration for near-field ground motions

	Bridge bent	Slight		Moderate		Extensive	
		x(g)	β	x(g)	β	x(g)	β
Ground motions	Near-field ground motion	0.66	0.15	1.10	0.16	3.10	0.18
	Far-field ground motion	0.65	0.10	1.04	0.16	2.78	0.13

The fragility function is defined as the probability of failure, which equals the probability of the drift ratio being larger than the drift limit state at the given IM. Fragility curves give an idea about the probability of exceeding the damage state of the structure for a given intensity measure of the ground motion. The evaluation of fragility helps determine the effectiveness of the BRB, as shown in Figure 5.15. Overall, this means that the bridge bent with BRB improves the structural seismic performance of the whole system.

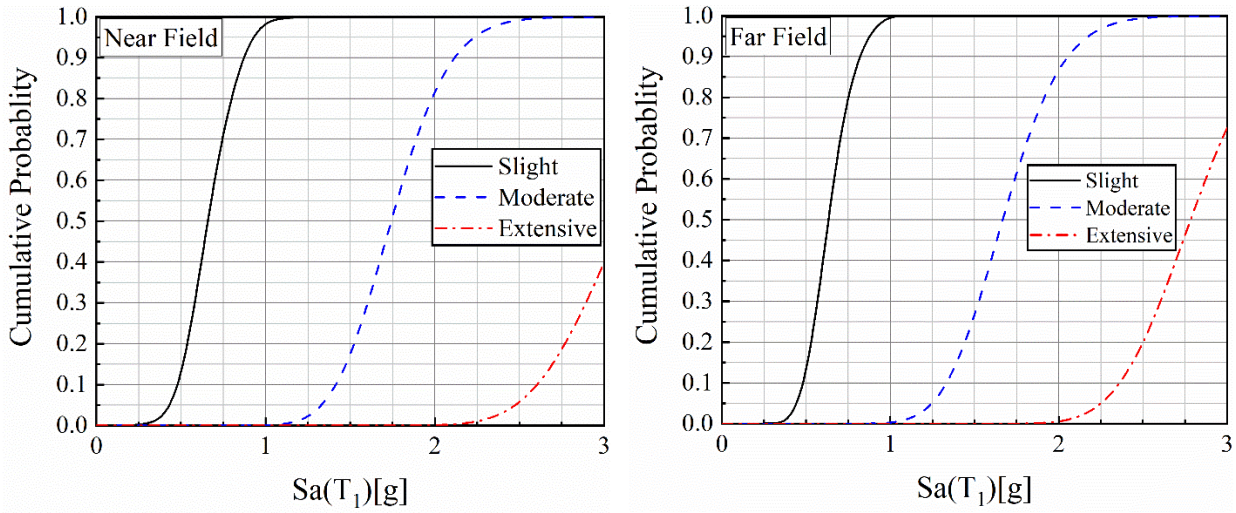

Figure 5.15 Fragility curves for near-field and far-field earthquake of PT-BRB Bent

6. SUMMARY, CONCLUSIONS AND FUTURE RECOMMENDATIONS

6.1 Summary

The value of the initial post-tensioning force in the hybrid bridge bent must satisfy the re-centering condition. The initial post-tensioning stress should not exceed 50% of the yield stress of the PT bars; rigid body analogy of the PT-Bent could be used as a preliminary design method for selecting the value of the initial post-tensioning force, but this should be checked against yielding at the PT bars at the target drift ratio. The yield displacement of the BRB should be smaller than the yield displacement of the PT-Bent. The hybrid system with a BRB should be designed such that the PT-Bent contributes at least 25% of the seismic-induced lateral force; the lateral force at yield displacement of the hybrid PT-BRB Bent should be less than or equal to the lateral force at yield displacement of the post-tensioned-only bent.

The lateral strength of the PT-BRB Bent should be less than 1.5 times the lateral strength of the post-tensioned-only bent. Steel collars must be provided up to a height equal to the column diameter to prevent the formation of concrete cracks or spalling in the columns. Stiffeners should be placed at the gusset assembly to prevent out-of-plane movement of the vertical steel plates and gussets. A clear gap should be designed between the gusset assemblies and rocking columns to prevent damage to columns during rocking based on the gusset plate expected column rotation and geometry. The authors suggest that the clear distance should be 3.0% of the column height.

6.2 Conclusions

A post-tensioned bridge bent, built with a diagonal BRB from the cap beam to one of the footings, was tested under quasi-static cyclic loads; the precast concrete columns of the bridge bent were allowed to rock in a controlled manner. The analytical model was developed for PT-BRB Bent, which showed excellent matching with experimental results. This numerical model was then expanded to represent an actual bridge bent, a post-tensioned three column bridge bent with two BRBs.

Based on the analysis of the numerical model and the experiments, the following conclusions are offered:

- The initial value of post-tensioning force in the PT bars, obtained using rigid body analogy, was conservative for re-centering. The capacity of the BRB, selected using a preliminary analysis, was sufficient to dissipate substantial hysteretic energy with good re-centering.
- The hybrid bridge bent with post-tensioned columns and a BRB had excellent performance and the hysteresis curves were stable and symmetric. The BRB added strength and stiffness to the hybrid bridge bent through yielding of the steel core until fracture. The BRB yielded early at 1.5% drift ratio and fractured after the second cycle of the 5.0% drift ratio.
- The post-tensioned columns rocked to a maximum rotation of 0.15 rad without causing instability; in addition, smooth and gradual degradation of stiffness was observed. The PT bars remained elastic up to 5.0% drift ratio; the two PT bars of the west column yielded at the 6.0% drift ratio after the BRB steel core had fractured.
- The combination of gravity load and post-tensioning was able to re-center the bridge bent to near its original position. The maximum residual drift ratio was 2.3%; this low residual drift ratio as compared to the imposed 6.0% drift ratio suggests that the bridge could re-center after a large earthquake since it is a dynamic phenomenon.
- No cracking was observed in the reinforced concrete cap beam, columns, or footings of the hybrid bridge bent; this is attributed to the large amount of hysteretic energy dissipated by the BRB in both tension and compression, the confinement provided by the steel collars at the top and bottom of the columns, and the re-centering offered by the PT bars and axial forces simulating gravity load. The maximum strain in the steel collars reached 0.4 times the yield

strain, which prevented column cracking and yielding of the steel spiral. The longitudinal mild steel bars yielded during the last cycle of the 6.0% drift ratio.

- The BRB connection details developed for the cap beam and footing using steel gusset assemblies were satisfactory. The maximum strain in the steel plates and stiffeners of the BRB gusset assemblies was less than 0.15 times the yield strain; in addition, no lateral buckling or instability was observed in any of the gusset assemblies.
- The equivalent viscous damping ratio of the hybrid bridge bent increased after yielding of the BRB and reached a maximum value of 15.4% of critical damping. During significant inelastic deformation of the BRB steel core, the damping ratio ranged between 10% to 15% of critical damping; this is a suitable value for design of such hybrid systems.
- The hybrid bridge bent with post-tensioned columns and a BRB is a good candidate for RC bridges constructed using accelerated construction methods in high seismic regions. After removal of the BRB, the gussets could be used to return the bridge to its original position and a new BRB could be installed. The proposed system is resilient, and bridges constructed in this manner could recover and function soon after an earthquake.
- The BRB eliminates or postpones yielding of the PT bars, which was predicted by the numerical model. The model predicted BRB fracture at the same drift ratio as the experiment. Incorporating *fatigue material* in the BRB steel core simulates well the accumulated fatigue behavior and gradual damage of the BRB in the experiment. The BRB model using *steel02* material in conjunction with *pinching material* and *fatigue material* displays good matching with the experimental results. However, the numerical model for the BRB cannot capture buckling of the steel core, which develops a large deflection with concrete crushing in the steel tube.
- The numerical model is within 15% of the experiment regarding peak lateral force capacity, hysteretic energy, and stiffness at each cycle. The numerical model is within 15% of the experiment regarding the post-tensioning forces in the columns. The axial deformation of the steel core of the BRB, when compared to the numerical model, shows a good match as the experimental value is within 10% of the analytical value.
- The *steel4* material used in the models captured the post-tensioning cyclic forces with an excellent match. The values defined for *steel4* can be used as the basis for modeling the PT bars in future experiments or actual bridge bents.
- The post-tensioned bridge bent with two BRBs showed excellent re-centering capabilities in the event of an MCE level earthquake for both near-field and far-field ground motions.
- Fragility analysis shows that the hybrid bridge bent with BRBs suffers minimal damage for both near-field and far-field earthquakes. Specifically, for the extensive damage state, the PT-BRB Bent can tolerate a much higher earthquake demand.

7. REFERENCES

ACI Committee 318. (2014). Building code requirements for structural concrete and commentary (ACI 318-14). American Concrete Institute, Farmington Hills, MI.

AISC (American Institute of Steel Construction). (2016). Seismic provisions for structural steel buildings. AISC 341. Chicago, IL.

Ameli, M.J., Parks, J.E., Brown, D.N., and Pantelides, C.P. (2015). "Seismic evaluation of grouted splice sleeve connections for reinforced precast concrete column–to–cap beam joints in accelerated bridge construction." *PCI J.*, 60(2), 80-103.

Ameli, M.J., Brown, D.N., Parks, J. E., and Pantelides, C. P. (2016). "Seismic column-to-footing connections using grouted splice sleeves." *ACI Struct. J.*, 113(5), 1021–1030.

Ameli, M.J, and Pantelides, C.P. (2017). "Seismic analysis of precast concrete bridge columns connected with grouted splice sleeve connectors." *J. of Struct. Eng.*, 143(2), 1-13.

Ardani, A. A., Lindsey, R., and Mallela, J. (2010). "One-weekend job: Rapid removal and replacement of 4500 South Bridge in Salt Lake City, Utah." *Transportation Research Record*, (2200), 12–16.

ASCE (2005). Minimum design loads for buildings and other structures. ASCE/SEI 7-05. Reston, VA.

Aslam, M., Fodden, W. G., and Scalise, D. T. (1980). "Earthquake rocking response of rigid bodies." *J. Structural Div., ASCE*, 106(ST2, Proc. Paper, 15182), 377–392.

ASTM (2015). "Standard specification for high-strength steel bars for prestressed concrete." A722/A722M-15, ASTM International, West Conshohocken, PA.

Baker, J. (2015). "Efficient analytical fragility function fitting using dynamic structural analysis." *Earthq. Spectra,* 31(1), 579–599.

Baker J. W., and Cornell C. A. (2006). "*Vector-valued ground motion intensity measures or probabilistic seismic demand analysis*." *PEER Research Rep. 2006/08, Pacific Earthquake Engineering Research Center*, Univ. of California, Berkeley, CA.

Bazaez, R., and Dusicka, P. (2016). "Cyclic behavior of reinforced concrete bridge bent retrofitted with buckling restrained braces." *Engineering Struct.*, 119, 34–48.

Bazaez, R., and Dusicka, P. (2018). "Performance assessment of multi-column RC bridge bents seismically retrofitted with buckling-restrained braces." *Bull. Earthq. Eng.*, 16(5), 2135–2160.

Billah, A. M., Alam, M. S., and Bhuiyan, M. R. (2012). "Fragility analysis of retrofitted multicolumn bridge bent subjected to near-fault and farfield ground motion." *J. Bridge Eng.*, 10.1061/(ASCE)BE.1943-5592 .0000452, 992–1004.

Billington, S. L., and Yoon, J. K. (2004). "Cyclic response of unbonded posttensioned precast columns with ductile fiber-reinforced concrete." *J. Bridge Eng.*, 9(4), 353–363.

Brenes, F. J., Wood, S. L., and Kreger, M. E. (2006). "Anchorage requirements for grouted vertical-duct connectors in precast bent cap systems." Report FHWA/TX-06/*4176*, Center for Transportation Research, Austin, TX.

Bu, Z., Guo, J., Zheng, R., Song, J., and Lee, G. C. (2016a). "Cyclic performance and simplified pushover analyses of precast segmental concrete bridge columns with circular section." *Earthq. Eng. Eng. Vibr.*, 15(2), 297–312.

Bu, Z.-Y., Ou, Y.-C., Song, J.-W., and Lee, G. C. (2016b). "Hysteretic modeling of unbonded posttensioned precast segmental bridge columns with circular section based on cyclic loading test." *J. Bridge Eng.*, 21(6), 04016016.

Buckle, I. G., Douglas, B., Mayes, R., Nutt, R., and Thoma, S. (1994). "*The Northridge, California earthquake on January 17, 1994: Performance of highway bridges*. " *Report NCEER-94-0008, National Center for Earthquake Engineering Research*, Univ. at Buffalo, NY.

Caltrans (2019). Caltrans Seismic Design Criteria. Version 2, California Department of Transportation, Sacramento, CA.

Canha, R. M. F., de Borja Jaguaribe, K., de Cresce El Debs, A. L. H., and El Debs, M. K. (2009). "Analysis of the behavior of transverse walls of socket base connections." *Engineering Struc.*, 31(3), 788–798.

Cheng, C. T. (2008). "Shaking table tests of a self-centering designed bridge substructure." *Engineering Struct.*, 30(12), 3426–3433.

Chou, C. C., and Chen, Y. C. (2006). "Cyclic tests of post-tensioned precast CFT segmental bridge columns with unbonded strands." *Earthquake Engineering and Structural Dynamics*, 35(2), 159–175.

Chou, C. C., and Chen, S. Y. (2010). "Subassemblage tests and finite element analyses of sandwiched buckling-restrained braces." *Engineering Struct.*, 32(8), 2108–2121.

Chou, C. C., Chang, H. J., and Hewes, J. T. (2013). "Two-plastic-hinge and two dimensional finite element models for post-tensioned precast concrete segmental bridge columns." *Engineering Struct.,* 46, 205–217.

Clough, R. W., and Huckelbridge, A. A. (1977). "Preliminary experimental study of seismic uplift of a steel frame." Report No. UCB/EERC-77/22, *Earthq. Eng. Res. Center*, Univ. California, Berkeley, CA.

Coleman, J., and Spacone E. (2001). "Localization issues in force-based frame elements." *J. Struct. Eng.*, 127(11), 1257–1265.

Cormack, L. G. (1987). "The design and construction of major bridges on the Mangaweka rail deviation." Tansactions, Inst. of Professional Eng., 1-14, Christchurch, NZ.

Culmo, M. P. (2011). "Accelerated bridge construction - experience in design, fabrication and erection of prefabricated bridge elements and systems." *Federal Highway Administration (FHWA). (2012). ⟨http://www.fhwa.dot .gov/bridge/abc/index.cfm⟩ (Mar. 18, 2014)*, (100), 1–347.

Dahal, P. K., and Tazarv, M. (2020). "Mechanical bar splices for incorporation in plastic hinge regions of RC members." *Constr. and Building Materials*, 258, 120308.

Dangol, I., and Pantelides, C. P. (2022). "Resilient posttensioned bridge bent with buckling restrained brace." *J. Bridge Eng.*, *27*(2), 04021107. https://doi.org/10.1061/(ASCE)BE.1943-5592.0001823.

Dangol, I., Thapa, D., and Pantelides, C.P. (2022). "Experimental evaluation of post-tensioned bridge bent under cyclic loads and comparison to hybrid bridge bents." *Engineering Struct.*, 256, 113962. https://doi.org/10.1016/j.engstruct.2022.113962.

Dhakal, R. P., and Maekawa, K. (2002). "Modeling for postyield buckling of reinforcement." *J. Struct. Eng.*, 128(9), 1139–1147.

Dong, W., Li, M., Lee, C. L., and MacRae, G. (2021). "Numerical modelling of glulam frames with buckling restrained braces." *Engineering Struct.*, 239, 112338.

Dutta, A., and Mander, J. B. (1998). “Seismic fragility analysis of highway bridges." *Proc., Center-to-Center Project Workshop on Earthquake Engineering in Transportation Systems*, Tokyo, 311–325.

Eatherton, M. R., Hajjar, J. F., Deierlein, G. G., Krawinkler, H., Billington, S., and Ma, X. (2008). “Controlled rocking of steel-framed buildings with replaceable energy-dissipating fuses.” *14th World Conf. Earthq. Eng.*, 12–17, Beijing, China.

El-Sheikh, M. T., Pessiki, S., Sause, R., and Lu, L. W. (1999). “Seismic behavior and design of unbonded post-tensioned precast concrete walls.” *PCI J.*, 44(3), 72–89.

El-Bahey, S., and Bruneau, M. (2011). “Buckling restrained braces as structural fuses for the seismic retrofit of reinforced concrete bridge bents.” *Engineering Struct.*, 33(3), 1052–1061.

ElGawady, M., Booker, A. J., and Dawood, H. M. (2010). “Seismic behavior of posttensioned concrete-filled fiber tubes.” *J. Composites for Constr.*, 14(5), 616–628.

ElGawady, M. A., and Sha’lan, A. (2011). “Seismic behavior of self-centering precast segmental bridge bents.” *J. Bridge Eng.*, 16(3), 328–339.

Erkmen, B., and Schultz, A. E. (2009). “Self-centering behavior of unbonded, post-tensioned precast concrete shear walls.” *J. Earthq. Eng.*, 13(7), 1047–1064.

Field, C., and Ko, E. (2004). “Connection performance of buckling restrained braced frames.” In *Proceedings of 13th World Conference on Earthquake Engineering. Vancouver, BC, Canada, Paper* (No. 1321).

Freddi, F., Dimopoulos, C. A., and Karavasilis, T. L. (2017). “Rocking damage-free steel column base with friction devices: design procedure and numerical evaluation.” *Earthq. Eng. Struct. Dyn.*, 46, 2281–2300.

Freddi, F., Dimopoulos, C. A., and Karavasilis, T. L. (2020). “Experimental evaluation of a rocking damage-free steel column base with friction devices.” *J. Struct. Eng.*, 146(10), 04020217.

Freddi, F., Tubaldi, E., Zona, A., and Dall’Asta, A. (2021). “Seismic performance of dual systems coupling moment-resisting and buckling-restrained braced frames.” *Earthq. Eng. Struct. Dyn.*, 50(2), 329–353.

Federal Highway Administration. (2013). Post-tensioning tendon installation and grouting manual. FHWA-NHI-13-026, Version 2, Washington, DC.

Gomes, A., and Appleton, J. (1997). “Nonlinear cyclic stress-strain relationship of reinforcing bars including buckling.” *Engineering Struct.*, 19(10), 822–826.

Guerrini, G., and Restrepo, J. I. (2015). “Self-centering precast concrete dual-shell steel columns.” Proc. 15th World Conf. on Earthquake Engineering, Lisbon, Portugal.

Guerrini, G., Restrepo, J. I., Massari, M., and Vervelidis, A. (2015). “Seismic behavior of posttensioned self-centering precast concrete dual-shell steel columns.” *J. Struct. Eng.*, 141(4), 04014115.

Haber, Z. B., Saiid Saiidi, M., and Sanders, D. H. (2015). “Behavior and simplified modeling of mechanical reinforcing bar splices.” *ACI Structural J.*, 112(2), 179–188.

Han, Q., Jia, Z., Xu, K., Zhou, Y., and Du, X. (2019). “Hysteretic behavior investigation of self-centering double-column rocking piers for seismic resilience.” *Engineering Struct.*, 188, 218–232.

Haraldsson, O. S., Janes, T. M., Eberhard, M. O., and Stanton, J. F. (2013). “Seismic resistance of socket connection between footing and precast column.” *J. Bridge Eng.*, 18(9), 910–919.

HAZUS 4.2 SP3. (2020). Hazus Earthquake Model Technical Manual. Department of Homeland Security: FEMA, Washington DC.

Hewes, J. T., and Priestley, M. J. N. (2002). “Seismic design and performance of precast concrete segmental bridge columns.” *Rep. No. SSRP-2001/25*, Univ. California San Diego, San Diego, CA.

Hofer, L., Zanini, M. A., Faleschini, F., Toska, K., and Pellegrino, C. (2021). “Seismic behavior of precast reinforced concrete column-to-foundation grouted duct connections.” *Bull. Earthq. Eng.*, 19(12), 5191–5218.

Housner, G. W. (1963). “The behavior of inverted pendulum structures during earthquakes.” *Bull. Seismol. Soc. America*, 53(2), 403–417.

Hoveidae, N., and Rafezy, B. (2012). “Overall buckling behavior of all-steel buckling restrained braces.” *J. Constr. Steel Res.*, 79, 151–158.

Jansson, P. O. (2008). “Evaluation of grout-filled mechanical splices for precast concrete construction. ” *Report No. R-1512*, Michgan Dept. Transp., Lansing, MI.

Jones, J., Shoushtari, E., Saiidi, M. “Saiid,” and Itani, A. (2020). “Comparison of seismic performance of socket and pocket connections for reinforced concrete bridge column base hinges.” *Transportation Research Record*, 2674(5), 349–360.

Kersting, R. A., Fahnestock, L. A., and López, W. A. (2015). “Seismic design of steel buckling-restrained braced frames.” *NEHRP Seismic Design Technical Brief*, (11), NIST, Gaithersburg, MD.

Kim, J., and Choi, H. (2004). “Behavior and design of structures with buckling-restrained braces.” *Engineering Struct.*, 26(6), 693–706.

Khan, M. A. (2014). Accelerated bridge construction: Best Practices and Techniques. Elsevier, Amsterdam, Netherlands.

Ko, E., and Field, C. (1988). “The unbonded brace^{TM}: from research to Californian practice.” *Technology*, February.

Kwan, W.-P., and Billington, S. L. (2003a). “Unbonded posttensioned concrete bridge piers. I: Monotonic and cyclic analyses.” *J. Bridge Eng.*, 8(2), 92–101.

Kwan, W. P., and Billington, S. L. (2003b). “Unbonded posttensioned concrete bridge piers. II: Seismic analyses.” *J. Bridge Eng.*, 8(2), 102–111

Mander, J. B., and Cheng, C.-T. (1997). “Seismic resistance of bridge piers based on damage avoidance design.” *Technical Report MCEER-97-0014*, 1–148, Multidisciplinary Center for Earthquake Engineering Research, Univ. at Buffalo, NY.

Mander, J. B., Priestley, M. J. N., and Park, R. (1988). “Theoretical stress-strain model for confined concrete.” *J. Struct. Eng.*, 114(8), 1804–1826.

Mander, J. B., Dhakal, R. P., Mashiko, N., and Solberg, K. (2007). “Incremental dynamic analysis applied to seismic risk assessment of bridges.” *Engineering Struct.,* 29(10), 2662–2672.

Marriott, D., Pampanin, S., Bull, D., and Palermo, A. (2008). “Dynamic testing of precast, post-tensioned rocking wall systems with alternative dissipating solutions.” *Bull. New Zealand Soc. Earthq. Eng.*, 41(2), 90–103.

Marriott, D., Pampanin, S., and Palermo, A. (2009). “Quasi-static and pseudo-dynamic testing of unbonded post-tensioned rocking bridge piers with external replaceable dissipaters.” *Earthq. Eng. Struct. Dyn.*, 38(3), 331–354.

Marsh, M. L., Stanton, J. F., Wernli, M., Eberhard, M. O., Garrett, B. E., and Weinert, M. D. (2011). “Application of accelerated bridge construction connections in moderate-to-high seismic regions. ” *NCHRP Report 698*, Washington, DC.

Mashal, M., and Palermo, A. (2019). “Low-damage seismic design for accelerated bridge construction.” *J. Bridge Eng.*, 24(7), 04019066. https://doi.org/10.1061/(ASCE)BE.1943-5592.0001406.

Mashal, M., White, S., and Palermo, A. (2012). “Concepts and developments for accelerated bridge construction and dissipative controlled rocking.” *15th World Conf. Earthq. Eng.*, Lisbon, Portugal.

Matsumoto, E., Waggoner, M., Kreger, M., Vogel, J., and Wolf, L. (2008). “Development of a precast concrete bent-cap system." *PCI J.*, 53(3), 74–99.

Matsumoto, E. (2009a). “Emulative precast bent cap connections for seismic regions: Grouted duct and cap pocket test results, design and construction specifications, design examples, and connection details.” *ECS Rep. No. ECS-CSUS-2009-05*, California State Univ., Sacramento, CA.

Matsumoto, E. E. (2009b). “Emulative precast bent cap connections for seismic regions: Component tests—Cap pocket full ductility specimen (unit 3).” *ECS Rep. No. ECS-CSUS-2009-03*, California State Univ., Sacramento, CA.

Mazzoni, S., Mckenna, F., and Fenves, G. (2005). OpenSees command language manual. Pacific Earthquake Engineering Research Center, Berkeley, CA.

McKenna F. (2014). Open system for earthquake engineering simulation (OpenSees). Pacific Earthquake Engineering Research Center, Berkeley, CA.

Mehrsoroush, A., and Saiidi, M. S. (2016). “Cyclic response of precast bridge piers with novel column-base pipe pins and pocket cap beam connections.” *Journal of Bridge Engineering*, *21*(4), 04015080.

Midorikawa, M., Ishihara, T., Azuhata, T., Hori, H., Kusakari, T., and Asari, T. (2009). “Three-dimensional shaking table tests on seismic response of reduced-scale steel rocking frame.” *Proc. 3rd Intern. Conf. Advances in Exper. Struct. Eng.,* Earthquake Engineering Research Center, San Francisco, California.

Mohebbi, A., Saiidi, M. S., and Itani, A. M. (2018). “Shake table studies and analysis of a PT-UHPC bridge column with pocket connection.” *J. Struct. Eng.*, 144(4), 04018021.

Motaref, S.; Saiidi, M.; and Sanders, D. H. (2011), “Seismic response of precast bridge columns with energy dissipating joints,” *Report No. CCEER-11-01,* Center for Civil Engineering Earthquake Research.

Motaref, S., Saiidi, M. S., and Sanders, D. (2014). “Shake table studies of energy-dissipating segmental bridge columns.” *J. Bridge Eng.*, 19(2), 186–199.

Ou, Y.-C., Chiewanichakorn, M., Aref, A. J., and Lee, G. C. (2007). “Seismic performance of segmental precast unbonded posttensioned concrete bridge columns.” *J. Struct. Eng.*, 133(11), 1636–1647.

Ou, Y.-C., Tsai, M.-S., Chang, K.-C., and Lee, G. C. (2010a). “Cyclic behavior of precast segmental concrete bridge columns with high performance or conventional steel reinforcing bars as energy dissipation bars.” *Earthq. Eng. Struct. Dyn.*, 39, 1181–1198.

Ou, Y.-C., Wang, P.-H., Tsai, M.-S., Chang, K.-C., and Lee, G. C. (2010b). “Large-scale experimental study of precast segmental unbonded posttensioned concrete bridge columns for seismic regions.” *J. Struct. Eng.*, 136(3), 255–264.

Pampanin, S., Marriott, D., and Palermo, A. (2010). "PRESSS design handbook." New Zealand Concrete Society, Auckland, New Zealand.

Palermo, A., and Mashal, M. (2012). “Accelerated bridge construction (ABC) and seismic damage resistant technology: A New Zealand challenge.” *Bull. New Zealand Soc. Earthq. Eng.*, 45(3), 123–134.

Palermo, A., Pampanin, S., and Carr, A. (2005). “Efficiency of simplified alternative modelling approaches to predict the seismic response of precast concrete hybrid systems.” *Proceedings of fib Symposium* 2, 1083–1088, Int. Federation for Struct. Concr., Lausanne, Switzerland.

Palermo, A., Pampanin, S., and Marriott, D. (2007). “Design, modeling, and experimental response of seismic resistant bridge piers with posttensioned dissipating connections.” *J. Structural Eng.*, 133(11), 1648–1661.

Pang, J. B. K., Eberhard, M. O., and Stanton, J. F. (2010). “Large-bar connection for precast bridge bents in seismic regions.” *J. Bridge Eng.*, 15(3), 231–239.

Pantelides, C. P., Gergely, I., Reaveley, L., and Volnyy, V. A. (1999). “Retrofit of R/C bridge pier with CFRP advanced composites.” *J. Struct. Eng*. 125 (10): 1094–9.

Pantelides, C. P., Reaveley, L., Duffin, J., Ward J., and Delahunty, C. (2003). “In-situ tests of three bents at South Temple Bridge on Interstate 15–Final report.” *Rep No. UT-03.32*. Utah: Utah Department of Transportation, Salt Lake City, UT.

Pantelides, C. P., Ward, J. P., and Reaveley, L. D. (2004). “Behavior of R/C bridge bent with grade beam retrofit under simulated earthquake loads.” *Earthq. Spectra*; 20(1): 91–118.

Pantelides, C.P., Duffin, J.B., and Reaveley, L.D. (2007). “Seismic strengthening of reinforced-concrete multicolumn bridge piers.” *Earthq. Spectra*; 23(3): 635–64.

Pantelides, C.P., and Fitzsimmons, G. (2012). “Case study of strategies for seismic rehabilitation of reinforced concrete multicolumn bridge bents.” *J. Bridge Eng.,* 17(1): 139–50. https://doi.org/10.1061/(ASCE)BE.1943-5592.0000203.

PEER (2021). NGA-West2 database flat-file, Pacific Earthquake Engineering Research Center. Available: http://peer.berkeley.edu/ngawest2/databases/ [last accessed November 2021].

Priestley, M. J. N., Evison, R. J., and Carr, A. J. (1978). “Seismic response of structures free to rock on their foundations.” *Bull. New Zealand Soc. Earthq. Eng.*, 11(3), 141–150.

Priestley, M. J. N., and Tao, J. R. (1993). “Seismic response of precast prestressed concrete frames with partially debonded tendons.” *PCI J.*, 38(1), 58–69.

Priestley, M. J. N., and MacRae, G. A. (1996). “Seismic tests of precast beam-to-column joint subassemblages with unbonded tendons.” *PCI J.*, 41(1), 64–80.

Priestley, M. J. N., Sritharan, S. S., Conley, J. R., and Pampanin, S. (1999). “Preliminary results and conclusions from the PRESSS five-story precast concrete test building.” *PCI J.*, 44(6), 42–67.

Rahmzadeh, A., Alam, M. S., and Tremblay, R. (2018). “Analytical prediction and finite-element simulation of the lateral response of rocking steel bridge piers with energy-dissipating steel bars.” *J. Struct. Eng.*, 144(11), 04018210.

Raynor, D. J., Lehman, D. E., and Stanton, J. F. (2002). “Bond-slip response of reinforcing bars grouted in ducts.” *ACI Structural J.*, 99(5), 568–576.

Restrepo, J. I., Matsumoto, E. E., and Tobolski, M. J. (2011). “Development of a precast bent cap system for seismic regions.” *National Cooperative Highway Research Program (NCHRP) Report 681,* Washington DC.

Robinson, B.K.S., Kersting, R. A., and Saxey, B. (2012). “No buckling under pressure.” *Modern Steel Construction*, AISC, Chicago, IL.

Roh, H.-S. (2007). “Seismic behavior of structures using rocking columns and viscous dampers.” PhD Dissertation, Dept. Civil, Struct. and Env. Eng., SUNY, Buffalo, NY.

Roh, H.-S., and Reinhorn, A. M. (2010). “Nonlinear static analysis of structures with rocking columns.” *J. Struct. Eng.*, 136(5), 532–542.

Routledge, P. J., Cowan, M. J., and Palermo, A. (2016). “Low-damage detailing for bridges – A case study of Wigram-Magdala Bridge.” *2016 NZSEE Conference*, 1–8.

Sahoo, D. R., and Chao, S.-H. (2015). “Stiffness-based design for mitigation of residual displacements of buckling-restrained braced frames.” *J. Struct. Eng.*, 141(9), 04014229.

Scott, M. H., and Fenves, G. L. (2006). “Plastic hinge integration methods for force-based beam–column elements.” *J. Struct. Eng.*, 132(2), 244–252.

Seismosoft. (2022). Seismomatch—A computer program for spectrum matching of earthquake records. Available at: https://www.seismosoft.com/seismomatch

Sideris, P., Aref, A. J., and Filiatrault, A. (2014). “Quasi-static cyclic testing of a large-scale hybrid sliding-rocking segmental column with slip-dominant joints.” *J. Bridge Eng.*, 19(10), 04014036.

Sideris, P., Aref, A. J., and Filiatrault, A. (2015). “Experimental seismic performance of a hybrid sliding–rocking bridge for various specimen configurations and seismic loading conditions.” *J. of Bridge Eng.*, 20(11), 04015009.

Spieth, H. A., Carr, A. J., Murahidy, A. G., Arnolds, D., Davies, M., and Mander, J. B. (2004). “Modelling of post-tensioned precast reinforced concrete frame structures with rocking beam-column connections.” *Research Report No. 2004-X*, New Zealand: Dept. of Civil Engineering, Univ. of Canterbury, Christchurch.

Sritharan, S., Priestley, M. J. N., and Seible, F. (1999). “Enhancing seismic performance of bridge cap beam-to-column joints using prestressing.” *PCI J.*, 44(4), 74–91.

Stanton, J., Stone, W. C., and Cheok, G. S. (1997). “A hybrid reinforced precast frame for seismic regions.” *PCI J.*, 42(2), 20–32.

Steuck, K. P., Eberhard, M. O., and Stanton, J. F. (2009). “Anchorage of large-diameter reinforcing bars in ducts.” *ACI Structural Journal*, *106*(4), 506.

Tang, B. M. (2014). “Accelerated bridge construction.” *Bridge Engineering Handbook, Second Edition: Construction and Maintenance*, CRC Press, 175–206.

Tazarv, M., and Saiidi, M. S. (2015). “UHPC-filled duct connections for accelerated bridge construction of RC columns in high seismic zones.” *Engineering Struct.*, 99, 413–422.

Thapa, D., and Pantelides, C. P. (2021). “Self-centering bridge bent with stretch length anchors as a tension-only hysteretic hybrid system.” *J. Struct. Eng.*, 147(10), 04021163.

Thiers-Moggia, R., and Málaga-Chuquitaype, C. (2019). “Seismic protection of rocking structures with inerters.” *Earthq. Eng. Struct. Dyn.*, 48(5), 528–547.

Thonstad, T., Mantawy, I. M., Stanton, J. F., Eberhard, M. O., and Sanders, D. H. (2016). “Shaking table performance of a new bridge system with pretensioned rocking columns.” *J. Bridge Eng.*, 21(4), 04015079.

Upadhyay, A., and Pantelides, C.P. (2019). “Experimental Program on Corebrace BRB.” *Technical Report*, University of Utah, Salt Lake City, Utah.

Upadhyay, A., and Pantelides, C. P. (2018). “Hybrid bridge bent for accelerated bridge construction using post-tensioned columns and BRBs.” *Sixteenth European Conference on Earthquake Engineering*, Thessaloniki, Greece.

Upadhyay, A., Pantelides, C. P., and Ibarra, L. (2019). “Residual drift mitigation for bridges retrofitted with buckling restrained braces or selfcentering energy dissipation devices.” *Eng. Struct*. 199 (2): 109663. https://doi.org/10.1016/j.engstruct.2019.109663.

U.S. Geological Survey (USGS). (2020). Earthquake Lists, Maps, and Statistics, accessed November 10, 2020, at URL. https://www.usgs.gov/natural-hazards/earthquake-hazards/lists-maps-and-statistics.

Wang, J., Wang, Z., Tang, Y., Liu, T., and Zhang, J. (2018). “Cyclic loading test of self-centering precast segmental unbonded posttensioned UHPFRC bridge columns.” *Bull. Earthq. Eng.*, 16(11), 5227–5255.

Wang, Y., Ibarra, L., and Pantelides, C. (2016). “Seismic retrofit of a three-span RC bridge with buckling-restrained braces.” *J. Bridge Eng.*, 21(11), 04016073.

Wang, Z., Li, T., Qu, H., Wei, H., and Li, Y. (2019). “Seismic performance of precast bridge columns with socket and pocket connections based on quasi-static cyclic tests: experimental and numerical study.” *J. Bridge Eng.*, 24(11), 04019105.

Watanabe, A., Hitomi, Y., Saeki, E., Wada, A., and Fujimoto, M. (1988). “Properties of brace encased in buckling-restraining concrete and steel tube.” *9th World Conf. on Eatthq. Eng*., Tokyo-Kyoto, Japan.

White, S., and Palermo, A. (2016). “Quasi-static testing of posttensioned nonemulative column-footing connections for bridge piers.” *J. Bridge Eng.*, 21(6), 04016025.

Wiebe, L., and Christopoulos, C. (2009). “Mitigation of higher mode effects in base-rocking systems by using multiple rocking sections.” *J. Earthq. Eng.*, 13, 83–108.

Wu, R. Y., and Pantelides, C. P. (2019). “Seismic evaluation of repaired multi-column bridge bent using static and dynamic analysis.” *Constr. Build. Mater.*, 208, 792–807.

Xie, Q. (2005). “State of the art of buckling-restrained braces in Asia.” *J. Constr. Steel Res.*, 61(6), 727–748.

Xu, W., and Pantelides, C. P. (2017). “Strong-axis and weak-axis buckling and local bulging of buckling-restrained braces with prismatic core plates.” *Engineering Struct.*, 153, 279–289.

Yamashita, R., and Sanders, D. H. (2009). “Seismic Performance of Precast Unbonded Prestressed Concrete Columns.” *ACI structural journal*, *106*(6).

Zareian, F., Krawinkler, H., and Ibarra, L. (2006). “Why and how to predict the probability of collapse of buildings.” *8th U.S National Conf. Earthq. Eng.*, San Francisco, CA.

APPENDIX

Table A1 *Steel02* material properties used for BRB modeling

***UniaxialMaterial steel02* Parameter**				
Specimen	**1**	**2**	**3**	**4**
E	29000 ksi	29000 ksi	29000 ksi	29000 ksi
R_0	20	21	24	23
E_{sh}	0.0001	0.0001	0.0001	0.0001
C_{r1}	0.92	0.93	0.94	0.93
C_{r2}	0.09	0.1	0.3	0.1
a_1	0.035	0.045	0.020	0.021
a_2	1	1	1	1
a_3	0.1	0.12	0.061	0.056
a_4	1	1	1	1
si	0.1	0.1	0.1	0.1

Note: 1 ksi = 6.895 MPa

Table A2 *Pinching4* material properties used for BRB modeling

***UniaxialMaterial pinching4* Parameter**				
Specimen	**1**	**2**	**3**	**4**
pEnvelopeStrain	[0.005, 0.01286, 0.00809, 0.000213]	[0.005, 0.01286, 0.00809, 0.000213]	[0.0000001, 0.000086, 0.00097, 0.000213]	[0.0065, 0.086, 0.00097, 0.000213]
pEnvelopeStress	[13.0, 2.0000001, 2.00001, 0.000001]	[13.0, 2.0000001, 2.00001, 0.000001]	[0.0000001, 0.0000001, 0.000001, 0.000001]	[14.0, 0.0000001, 0.000001, 0.000001]
nEnvelopeStrain	[-0.0022, -0.01388, -0.01588, -0.0220923]	[-0.0022, -0.01488, -0.019900923, -0.1220923]	[-0.0022, -0.015488, -0.021900923, -0.0001220923]	[-0.0022, -0.015488, -0.021900923, -0.0001220923]
nEnvelopeStress	[2.272, -30.00038, -45.0936, -0.000001]	[0.272, -33.00038, -20.0936, -0.000001]	[0.272, -38.00038, -60.0936, -0.0001]	[6.272, -36.00038, -60.0936, -0.0001]
rDisp	[-0.99, 1]	[-0.99, 1]	[-0.99, 1]	[-0.99, 1]
rForce	[-1, 1]	[-1, 1]	[-1, 1]	[-1, 1]
uForce	[0.9, -0.9]	[0.9, -0.9]	[0.9, -0.9]	[0.9, -0.9]

Table A3 *Fatigue* material properties used for BRB modeling

***UniaxialMaterial fatigue* Parameter**				
Specimen	**1**	**2**	**3**	**4**
E0	0.163 *LR_BRB	0.163 *LR_BRB	0.287*LR_BRB	0.156 *LR_BRB
m	-0.701	-0.701	-0.701	-0.701
min	-0.035	-0.035	-0.035	-0.035
max	0.035	0.035	0.035	0.035

Note: LR BRB = yield length ratio.

Table A4 Near-field ground motions

GM S.N	**Earthquake**			**Recording Station**	**Epicentral distance (km)**	**PGA (g)**
	M	**Name**	**Year**			
N1	6.5	Imperial Valley-06	1979	El Centro Array #6	27.47	0.44
N2	6.5	Imperial Valley-06	1979	El Centro Array #7	27.64	0.46
N3	6.9	Irpinia, Italy-01	1980	Sturno	30.35	0.31
N4	6.5	Superstition Hills-02	1987	Parachute Test Site	15.99	0.42
N5	6.9	Loma Prieta	1989	Saratoga - Aloha Ave	27.23	0.38
N6	6.7	Erzican, Turkey	1992	Erzincan	8.97	0.49
N7	7	Cape Mendocino	1992	Petrolia	4.51	0.63
N8	7.3	Landers	1992	Lucerne	44.02	0.79
N9	6.7	Northridge-01	1994	Rinaldi Receiving Sta	10.91	0.87
N10	6.7	Northridge-01	1994	Sylmar - Olive View Med FF	16.77	0.73
N11	7.5	Kocaeli, Turkey	1999	Izmit	5.31	0.22
N12	7.6	Chi-Chi, Taiwan	1999	TCU065	26.67	0.82
N13	7.6	Chi-Chi, Taiwan	1999	TCU102	45.56	0.29
N14	7.1	Duzce, Turkey	1999	Duzce	1.61	0.52

Table A5 Far-field ground motions

GM S.N	Earthquake			Recording Station	Epicentral distance (km)	PGA (g)
	M	Name	Year			
F1	6.7	Northridge	1994	Beverly Hills - Mulhol	13.3	0.52
F2	6.7	Northridge	1994	Canyon Country-WLC	26.5	0.48
F3	7.1	Duzce, Turkey	1999	Bolu	41.3	0.82
F4	7.1	Hector Mine	1999	Hector	26.5	0.34
F5	6.5	Imperial Valley	1979	Delta	33.7	0.35
F6	6.5	Imperial Valley	1979	El Centro Array #11	29.4	0.38
F7	6.9	Kobe, Japan	1995	Nishi-Akashi	8.7	0.51
F8	6.9	Kobe, Japan	1995	Shin-Osaka	46	0.24
F9	7.5	Kocaeli, Turkey	1999	Duzce	98.2	0.36
F10	7.5	Kocaeli, Turkey	1999	Arcelik	53.7	0.22
F11	7.3	Landers	1992	Yermo Fire Station	86	0.24
F12	7.3	Landers	1992	Coolwater	82.1	0.42
F13	6.9	Loma Prieta	1989	Capitola	9.8	0.53
F14	6.9	Loma Prieta	1989	Gilroy Array #3	31.4	0.56
F15	7.4	Manjil, Iran	1990	Abbar	40.4	0.51
F16	6.5	Superstition Hills	1987	El Centro Imp. Co.	35.8	0.36
F17	6.5	Superstition Hills	1987	Poe Road (temp)	11.2	0.45
F18	7	Cape Mendocino	1992	Rio Dell Overpass	22.7	0.55
F19	7.6	Chi-Chi, Taiwan	1999	CHY101	32	0.44
F20	7.6	Chi-Chi, Taiwan	1999	TCU045	77.5	0.51
F21	6.6	San Fernando	1971	LA - Hollywood Stor	39.5	0.21
F22	6.5	Friuli, Italy	1976	Tolmezzo	20.2	0.35